

Optimisation methodology of large-scale 3D printing using recycled plastics

Jiayi Wang

Civil Engineering and Geosciences



Optimisation methodology of large-scale 3D printing using recycled plastics

by

Jiayi Wang

in partial fulfillment of the requirements for the degree of

Master of Science
in Civil Engineering

at the Delft University of Technology,
to be defended publicly on Tuesday March 27, 2018 at 10:30 AM.

Chairman:	Prof. ir. R. Nijse ,	TU Delft
Thesis committee:	Dr. ir. F. A. Veer,	TU Delft
	Dr. ir. H. R. Schipper,	TU Delft
	Dr. ir. J. L. Coenders,	White Lioness technologies
	Ir. R. Houtman,	Tentech BV

This thesis is confidential and cannot be made public until March 28, 2020.

An electronic version of this thesis is available at <http://repository.tudelft.nl/>.

Acknowledgements

This graduation project was carried out between March 2017 and March 2018 in cooperation with Delft University of Technology, Tentech B.V., Aectual and White Lioness technologies.

At the beginning of this report, I would like to thank all the people and parties involved in the process of this project. First of all, I want to thank the owners of Tentech B.V., Rogier Houtman and Harmen Werkman, they offered me the opportunity to get involved in this exciting project and provided me generous help and encouragement during it. I am deeply grateful to Jeroen Coenders, Founder and CEO of White Lioness technologies, who introduced me to Tentech B.V. and inspired me with his advanced thoughts. My deepest gratitude to my graduation committee members: Chairman Professor Rob Nijse, Daily-supervisor Roel Schipper, Test-supervisor Fred Veer and mentioned Rogier Houtman and Jeroen Coenders, this project would not be accomplished without their full support and guidance.

I express my deep sense of gratitude to Ina Cheibas, Head of Production and Material Development of Aectual, for her support in arranging the printing and dealing with the tough process of recycling plastics. I am grateful to Paweł Baran, who generously shared his knowledge, experience and give me great help. I would like to show my gratitude to Maiko van Leeuwen for making room in his tight schedule to help me, it was really fun to cast concrete with him, and I have learnt a lot during the process. I also would like to thank all the colleagues at Tentech B.V., they let me experienced the 'nederlandse cultuur' and I really enjoy the time with them.

Last but not least, I would like to thank my friends and family, especially my parent, they have given me their great trust and support during my study in the Netherlands and understandings when I had obstacles, I am really grateful for their endless love.

Jiayi Wang
Utrecht, March 2018

谨以此文献给我的父母。

This thesis is dedicated to my parents.

Abstract

Large-scale 3D printing technology provides numerous of possibilities for the construction industry thanks to its flexibility and labour saving. *Aectual*, a subsidiary of *DUS Architects*, Amsterdam, dedicates to explore the possibilities of using polymers as material for large-scale 3D printing in construction activities. Together with *Tentech*, a Utrecht based engineering firm, they have investigated the structural feasibility of this technology in recent years and obtained fruitful achievements, especially in its application as moulds. However, the relatively high price of the material, *Technomelt 3D 6910*, triggers them to seek for the potential alternatives, and recycled plastics stands out as a promising solution. The content of this report is to explore the feasibility of combining large-scale 3D printing technology and recycled plastic and use it for designing moulds of relatively large scale concrete products. The exploration started with the investigation of the material properties of recycled material compositions based on three candidate materials: *Scofelin 53-G-10 natural*, *Technomelt 3D 6910* and *60%LDPE+40%PPgf recycled*. After the evaluation with preliminary test, one most promising composition was selected for the further investigation with respect to its mechanical properties. In the meantime, a conceptual methodology, which aims to take advantage of the 3D printing technology to improve the structural efficiency of 3D printed mould was proposed based on the numerical analysis results of the selected material. Then, results together with phenomenon and issues found during the research were discussed and corresponding conclusions were drawn. It is possible to use the recycled plastics for the structural purpose and take advantage of the flexibility of 3D printing technology to improve the structural efficiency, especially for designing moulds for irregular concrete products. However, its benefit is significantly influenced by the multilayer printing and shrinkage issue accompanying by the utilization of plastic. At the end of this report, possible improvements, including the laboratory experiments, numerical analysis and practical implementation, are recommended for the further research.

Key words: 3D printing, recycled plastics, moulds, Finite Element Analysis, optimisation.

Intelligence is the ability to adapt to change.

— *Stephen Hawking*

Contents

1	Backgrounds	1
1.1	3D printing technology	2
1.2	Recycling of plastics	3
1.3	Structural optimisation	6
1.4	Previous work	8
2	Introduction	9
2.1	Research questions	9
2.2	Scope of the research	9
2.3	Material description	10
2.4	Research method	11
2.4.1	Material test	11
2.4.2	Numerical modelling	13
2.5	Outline of the contents	14
3	Preliminary test	15
3.1	Test description	15
3.2	Test results	15
3.2.1	Composition test of Scolefin 53-G-10 natural	16
3.2.2	Composition test of Technomelt 3D 6910	18
3.2.3	Composition test of 60%LDPE 3+40%PPgf recycled	20
3.2.4	Recycling round test of Technomelt 3D 6910	21
3.2.5	Creep test	22
3.3	Evaluation and selection	23
4	Other property tests	25
4.1	Test description	25
4.1.1	Tensile test	27
4.1.2	Flexural test	27
4.1.3	Shear test	28
4.2	Test results	28
4.2.1	Tensile test	29
4.2.2	Bending test	30
4.2.3	Shear test	31
4.3	Summary and issues	32
5	Numerical modelling	37
5.1	Objectives	37
5.2	Approaches	38
5.2.1	Modelling with shell elements	38
5.2.2	Modelling with volumetric elements	39
5.2.3	Modelling with sandwich element	40
5.3	Element type	41
5.3.1	Inner and outer layers	41
5.3.2	Rib layer	43
5.4	Analysis mode	43
5.5	Material Inputs	43
5.5.1	Inputs for the shell element	44
5.5.2	Inputs for the volumetric element	47

5.6	Numerical validation	50
5.6.1	Material tests validation	50
5.6.2	Single-layer mould	52
5.6.3	Multilayer hexagon	53
5.6.4	Hexagonal mould	54
5.7	Summary	54
6	Design methodology	57
6.1	Variables and inputs	57
6.2	Implementation	58
6.2.1	Sensitivity analysis	58
6.2.2	Iteration algorithm	59
6.3	Example	60
6.4	Summary	63
7	Case study	65
7.1	General information	65
7.2	Mould design	66
7.3	Post-processing	68
7.4	Practical implementation	70
7.4.1	Preparation	70
7.4.2	Concrete casting	71
7.5	Summary and issues	72
8	Discussion	75
8.1	Laboratory experiments and material properties	75
8.1.1	Overview	75
8.1.2	Recycling	75
8.1.3	Material properties	76
8.2	Numerical analysis	76
8.3	Practical implementation	77
9	Conclusions	79
9.1	Laboratory experiments and material properties	79
9.2	Numerical analysis	79
9.3	Practical implementation	80
10	Recommendations	81
10.1	Laboratory experiments and material properties	81
10.2	Numerical analysis	82
10.3	Practical implementation	82
A	Material Information of <i>Scolefin 53-G-10 natural</i>	83
B	Calculation of the characteristic value for material properties	85
C	Raw data of preliminary tensile test	87
C.1	Composition test results: <i>Scolefin 53-G-10 natural</i>	88
C.2	Composition test results: <i>Technomelt 3D 6910</i>	92
C.3	Composition test results: <i>60%LDPE 3+40%PPgf recycled</i>	96
C.4	Recycling round test results: <i>Technomelt 3D 6910</i>	100
D	Raw data of other property test for the selected material	103
D.1	Tensile test results	104
D.2	Bending test results	106
D.3	Shear test results	109

E	Effective length for tensile test	113
F	Hydrostatic pressure during concrete casting	115
G	Mathematical limitation of using triple-layer shell element	117
H	Derivation of the material inputs for the shell element	119
I	Definition of the maximum side length of hexagon	121
J	Conversion from the homogenized properties to the element properties	125
K	Custom defined interpretation of the strain results	129
L	Details of the parametric bench for the case study	131
M	Details of the self-compact concrete C65	133
	List of Figures	135
	List of Tables	139
	Bibliography	141

1

Backgrounds

Industry 4.0, is a new term which originally appeared at the Hannover Fair in 2011. Later on in 2016, it was written in *High-tech Strategy 2020* [1]. In the meantime, Chinese government published *Made in China 2025*, which aims to transform China into a world manufacturing power [2]. Both of them have the same goal: the digital revolution of manufacturing. As a newly developed technology, 3D printing is one of the representative approaches to achieve the digitization and automation, and large-scale 3D printing brings multiple opportunities for structural design, including the structure itself and construction process. From 2014, DUS architects started to investigate possibilities of utilizing the 3D printing technology in construction activities by equipping large-scale 3D printer, *Kamermaker*, which uses plastic as material to print structures. This creates a potential possibility of combining large-scale 3D printing and plastics recycling to improve flexibility, sustainability, economic and environmentally friendly in the construction industry.



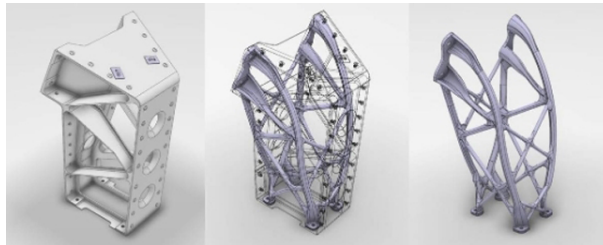
Figure 1.1: 3D printed Urban Cabin by DUS architects [3] (photo by Ossip van Duivenbode).

1.1. 3D printing technology

3D printing refers to additive manufacturing which constructs three-dimensional object with automating layer-by-layer production process [4]. Its early development can trace back to 1980s [5], and in recent years it becomes more and more popular and practical in multiple sectors such as medical industry and aerospace.



(a) 3D printed liver by Mako Sugimoto at Kobe University [6].



(b) 3D printed bracket by Airbus [7].

Figure 1.2: Application of 3D printing.

As for the application 3D printing technology in construction activities, many attempts have been made to improve and develop this traditional industry. Different approaches, such as inkjet powder printing, laser sintering and contour crafting, can be applied in order to take benefit from 3D printing like waste reduction, flexibility and manpower reduction [8]. For example, Arup, an international engineering firm, has carried out an exploration on Direct Metal Laser Sintering (DMLS) with topology optimisation to improve the design of a steel node for a tensegrity structure in The Hague [9]. By taking advantage of the flexibility of the 3D printing technology, the weight of the node is reduced significantly (Fig. 1.3).



Figure 1.3: Stainless steel node made by additive manufacturing [9].

Using concrete as material for 3D printing, which usually uses contour crafting as printing method, is also developing rapidly. Winsun, a Shanghai-based 3D printing company, has constructed multiple projects with concrete 3D printing, e.g. Phoenix International Media (Fig. 1.4), which shows the advantage of the customization of this technology.



Figure 1.4: Application of concrete 3D printing in Phoenix International Media project [10].

Besides steel and concrete, technologies which could use local materials such as mud, dirt and sand are also inventing by some companies [11]. While plastics, which is utilized by 3D printing technology since the very beginning of its development for small-scale products [12], is also a promising material for large-scale printing in the construction industry. Amsterdam-based company Aectual, which is a subsidiary of DUS architects, is developing large-scale 3D printing technology using plastics in many aspects, such as façade, floor and moulds for concrete (Fig. 1.5).



Figure 1.5: Large-scale 3D printed products by Aectual [13]. Left: facade. Middle: floor. Right: mould for casting concrete staircase.

Overall, the application of the 3D printing technology has a wide coverage in modern industries. Its advantages in flexibility, customizability, reduction of the material consumption and many other aspects make it promising and attractive. As for its prospect in construction activities, it brings innovation and more possibilities to improve the construction methods and concepts.

1.2. Recycling of plastics

Plastics are common material in terms of civil and industrial use. Its utilization has a wide coverage because of many advantages such as low-price, high strength and chemical resistance [14]. However, it causes considerable pollution after its end-of-life. In 2010, 4.8 to 12.7 million metric tons plastic waste from 192 coastal countries enters the ocean and this number is still increasing [15]. Therefore, measures need to be taken to prevent endless pollution, while recycling is a possible strategy. Because

of the increasing sense of economic and environment, the rate of recycling plastic has a substantial increase [16].



Figure 1.6: Beach cleanup activity conducted by Greenpeace on Freedom Island, Philippines [17].

As shown in Fig. 1.7, plastics can be distinguished as thermoplastics and thermosets. The former can be moulded again after reheating, while the latter cannot due to the irreversible chemical changes during the heating process. The main focus of this thesis is on the thermoplastics since its remouldability makes it easier to be recycled. However, it does not mean thermosets cannot be recycled, methods such as chemical recovery are developing with respect to recycling thermosets [18, 19].

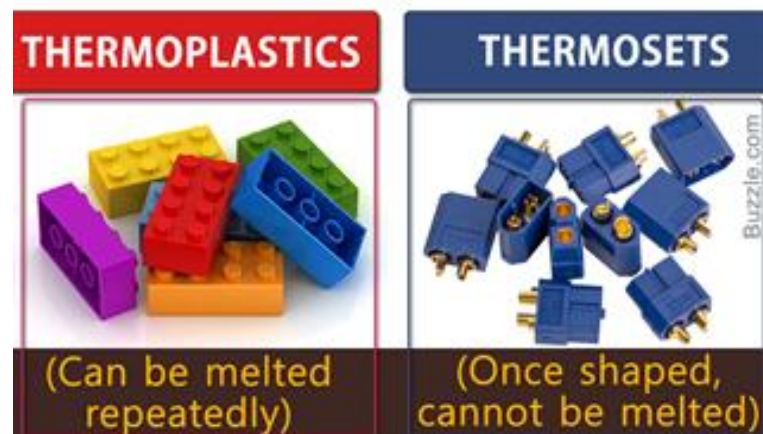


Figure 1.7: Thermoplastics and thermosets [20].

The thermoplastics, including polyolefins such as polyethylene(PE) and polypropylene(PP), can be recycled by mechanical treatment. This process mainly contains two stages (Fig. 1.8): the first stage includes operations for the preparation of the materials such as material collection and washing, and the second stage is about the remoulding the plastic product [21].

However, the recycling of the plastics is not as simple as melt and extrude, it is usually accompanied by property degradation. This is because physical treatment would damage the molecular linear chain and cut them into segments and results in a property reduction after the recycling (Fig. 1.9). This impact is severer on PP than PE with the increase operation round of recycling, because the former

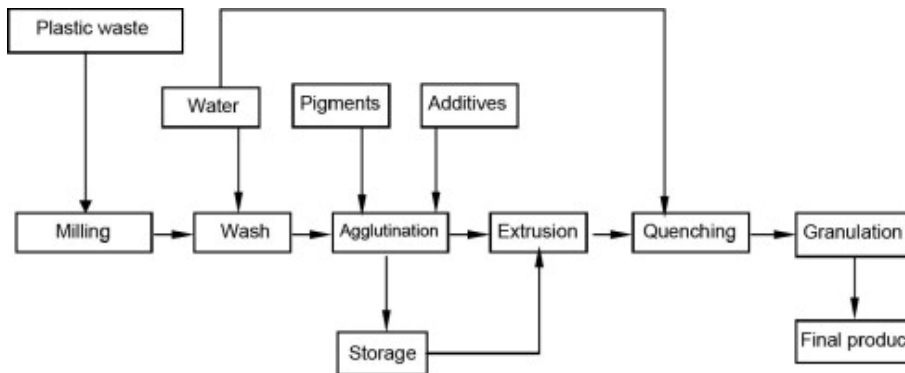


Figure 1.8: Mechanical recycling steps of plastics [21, 22].

has chain-scission and the latter has cross-linking during the recycling [23]. The investigation of the degradation of the properties becomes one of the main topics with respect to plastic recycling. Mechanical performance of recycled PP and carbon fibres composite was investigated by Giannadakis et al [24]. Strapasson et al have done researches on PP and Low Density Polyethylene(LDPE) to get a view of tensile and impact behaviour [25]. There are also researches which relates 3D printing technology and recycling plastic, such as the work of Anderson on the investigation of the mechanical properties of virgin/recycled Polylactic Acid (PA) compositions after 3D printed [26], and the work of Veer et al on the strength and ductility of 3D printed PP with glass fibre reinforcement after recycling [27].

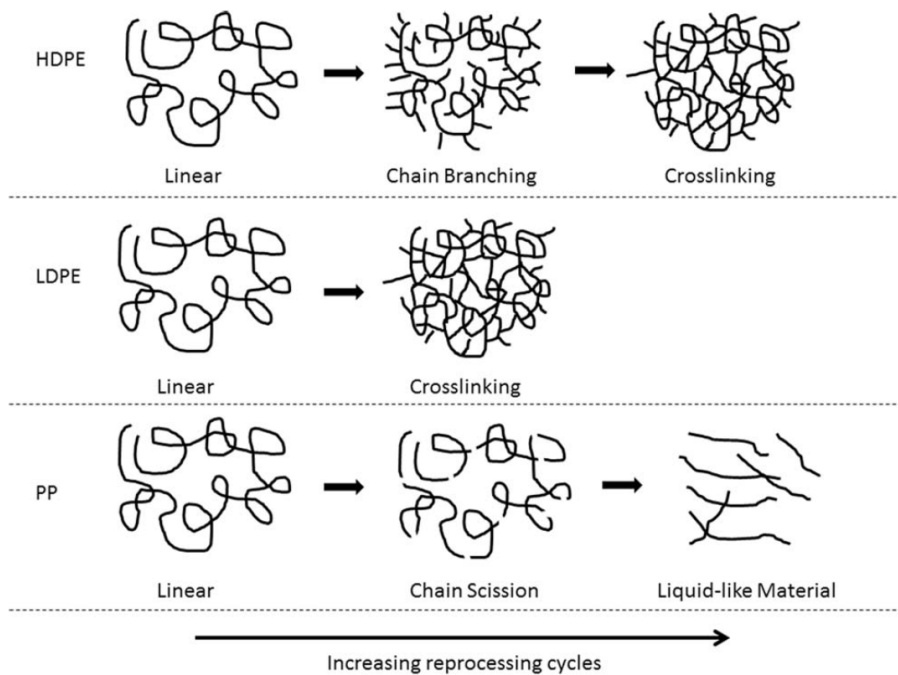


Figure 1.9: Several physical phenomena occur with the increase of the recycling cycle [23].

In terms of the investigation of recycling plastics at Aectual, its potential benefit of combining large-scale 3D printing technology and recycled plastics is very attractive. The process of utilization of the recycled plastics is rather simple now, printed products are demolished into small segments, and shredded further with special machine. The small pellets are mixed with virgin materials and being ready for the new printing (Fig. 1.10). This process is not perfect, but it is a good start of the implementation of this combination.

Overall, plastic recycling is a promising solution for solving the problem caused by the waste plastics.



Figure 1.10: Preparation of the material for recycling at Aectual. Left: small segments. Middle: shredded pellets for printing. Right: printing process(example) [28].

However, it has benefit and challenge at the same time in terms of the recycling technology and social aspect. Moreover, the degradation of the properties is a crucial topic in order to increase the applicability of the recycled plastics, and it is also one of the focal points of this research.

1.3. Structural optimisation

How to improve the structural efficiency is a topic that worth exploring. Antoni Gaudí, a famous Spanish architect in the late 19th and early 20th centuries, uses form finding techniques to increase the structural efficiency in his works during his professional life. For instance, during the designing of Sagrada Família, he used a scaled reversed force model to prototype the structure and find the optimal solution of its the shape(Fig. 1.11).



Figure 1.11: Form finding used by Antoni Gaudí during the design of Sagrada Família [29].

Moreover, German architect and structural engineer Frei Otto is also one of the representatives. He has great contributions to tensile and membrane structures, and he is keen to use structural knowledge and experimental models to improve the lightweight structures, e.g. tree structure in Fig. 1.12.

In the recent years, with the development of the computer, the applicability of the structural op-

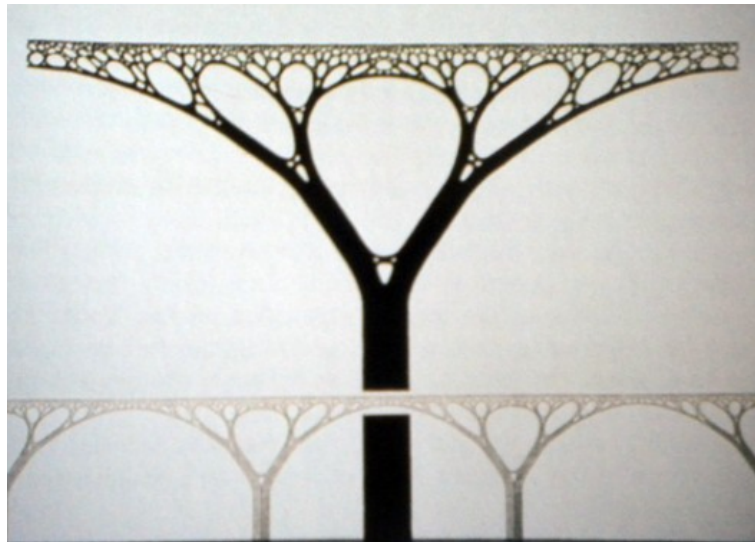


Figure 1.12: Tree structures [30].

timisation becomes more and more feasible. Generally, structural optimisation can be simplified to a minimize(or maximize) problem, which can be written in formula [31] as:

$$\text{Find } x \text{ to minimize } f(x) \text{ subject to } g(x) \leq 0 \tag{1.1}$$

where:

- f is the objective function.
- x is an n-vector which has n components.
- g is the constrains.

Moreover, structural optimisation is usually divided into three three categories: Sizing optimisation, shape optimisation and topology optimisation [32]. Its application can be found in many sectors, such as automotive manufacturing and design. What is more, with the development of 3D printing technology, the possibility and applicability of the structural optimisation, especially topology optimisation, has increased significantly thanks to the flexibility of the 3D printing.

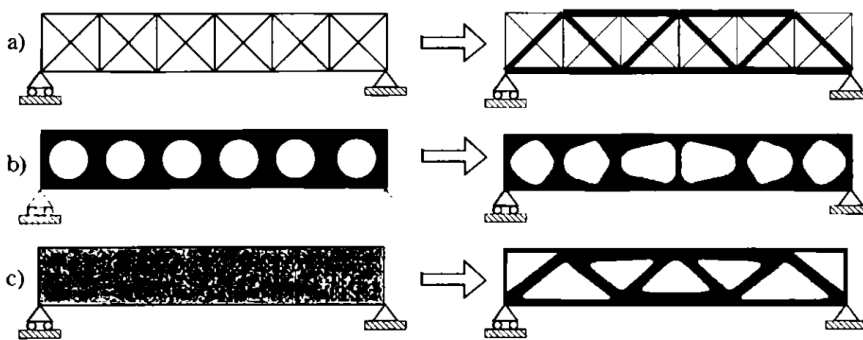


Figure 1.13: Three categories of structural optimisation.(a)sizing optimisation (b)shape optimisation (c)topology optimisation [32].

However, the application of the structural optimisation should be based on the specific case. Within the scope of this research, the investigated structure type is 3D printed mould. It has features like: it is subject to hydrostatic pressure caused by the concrete, and its planar shape is similar to the truss. These features determine that not all the optimization approaches are suitable for it. Finally, if treat the mould as one whole structure, the shape optimisation might be a feasible solution.

1.4. Previous work

As a continuous research on exploring the feasibility of large-scale 3D printing technology in construction activities, architects from DUS, Amsterdam, together with engineers from Tentech, Utrecht, have cooperation in many projects. The printer, called *KamerMaker*, uses polymers as materials to construct structures with layer-by-layer extrusion. The application of this technology can be generally distinguished as three topics: full-print, moulds and hybrid (Fig. 1.14).

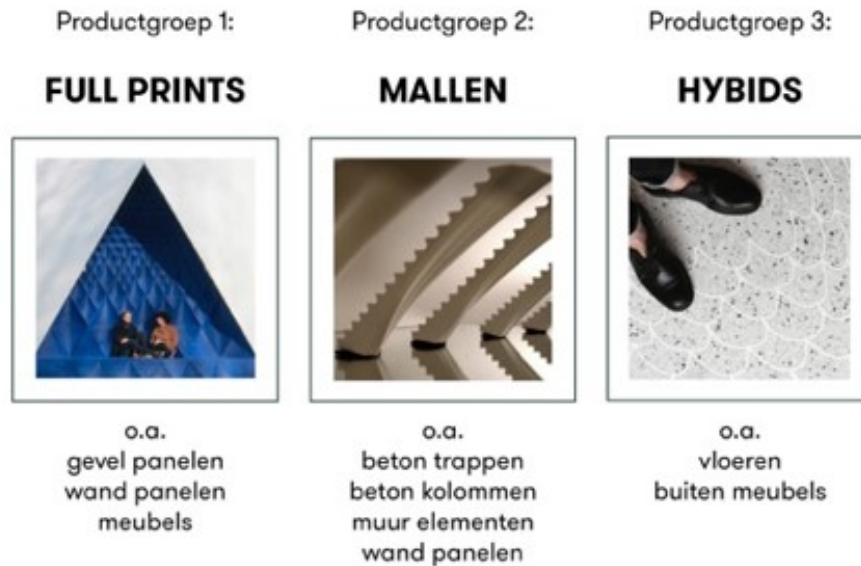


Figure 1.14: Three types of application with the large scale 3D printing [13].

In 2014, the structural feasibility of the technology is investigated by Veen [33], and he established material test foundation and pointed out the possible improvement could be made for further development. Puelen explored the buckling issue in terms of combining the 3D printed columns with a steel core [34]. In 2016, Baran has improved the material test frame and developed a pre-deformation methodology for designing the 3D printed moulds [35]. All these projects made contributions to the development of this technology and made it become much possible to be applied in the real life. In 2017, a subsidiary, Aectual, is established by DUS architects to focus on the application and investigation of the large-scale 3D printing technology and the corresponding development of the material.

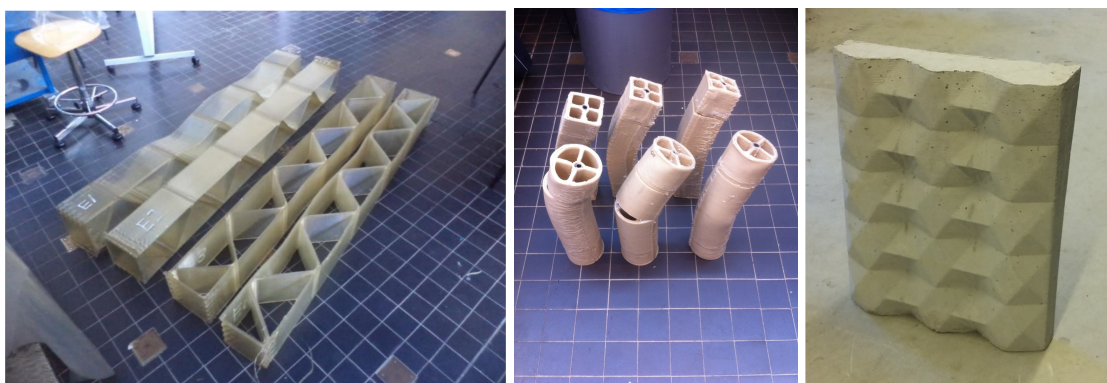


Figure 1.15: Previous projects. Left: printed beam for testing [33]. Middle: printed columns with steel core after test [34]. Right: parametric wall designed with utilization of pre-deformation method [35].

2

Introduction

In this chapter, an introduction of the research is presented. It includes the following: The questions definition and scope of the research, an introduction of the investigated materials, research methods for laboratory activities and numerical modelling, and an outline which gives an overview of the main points in the research.

2.1. Research questions

As mentioned in Chapter 1, several works have been performed on the feasibility of large-scale 3D printing technology with plastics. The general properties and characteristics of *Technomelt 3D 6910* have been investigated, and a clear scheme for testing the basic properties for structural use was established [35, 36]. However, the price of *Technomelt 3D 6910* is rather high compared with common plastics since it is bio-based and specially designed for 3D printing. Using recycled plastics could help to reduce the cost and make the process more sustainable at the same time. Besides, the structural feasibility was investigated mainly for single-layer printing, and only few tests and conclusions are made regarding the structured geometry and multi-layer printing. It is certain that with the scale of the structure getting larger, the complexity of the geometry will increase, and more factors, such as printing path, need to be taken into account due to their impact on the structural behaviour. Moreover, thanks to the features of 3D printing technology, it is possible to improve the products¹ with respect to economic, customisation and structural purpose. Based on these aspects, three core questions are raised:

1. How to utilize recycled plastics as material for 3D print moulds?
2. What is the influence of the geometry on the structural behaviour of printed products?
3. How to take advantage of the features of 3D printing technology to improve the printed products?

These questions were investigated and answered in the research based on laboratory experiments, numerical modelling and analysis.

2.2. Scope of the research

Both plastics and 3D printing technology have numerous parameters, thus the scope of the research needed to be limited with logical constraints. The range of the questions declared in Section 2.1 is therefore adjusted with a framework including specific objectives and conditions. The framework applied in the research has contents as below:

1. Material tests were carried out on limited number of recycled materials. There are various kinds of recycled plastics with respect to polymer type, recycling method and reinforcement method. During the research, 3 basic plastics with 15 different compositions were investigated. See Section 2.3.

¹Full print, Moulds and Hybrid. See Chapter 1.

2. Only basic mechanical properties are chosen as inputs for modelling stage. See Chapter 4.
3. All the experiments were conducted under controlled environmental conditions. The testing condition is limited to indoor environment with a room temperature and moisture content to reduce the external variables. See Fig. 2.1.
4. The purpose of numerical modelling is to utilize the results derived from materials test for designing the mould. However, due to the time-scale relationship limitation and large-scale 3D printing, it is difficult to validate the structured printed moulds with experiments. Therefore, only a concept is proposed along with numerical implementation and validation.
5. The geometry of the mould has a pre-defined planar pattern in order to constrain the printing path. Most of the work regarding numerical modelling will be based on this pattern. See Chapter 6.

Although the scope of the research is based on several pre-set conditions, the final outcome and conclusion of the research should be sufficient for answering proposed questions and to provide a general overview for the further research. Further validation and testing are expected to extend the applicability.

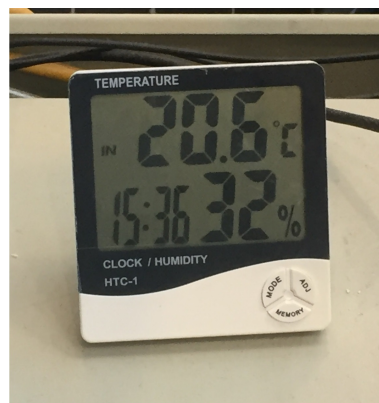


Figure 2.1: Environmental conditions for tests

2.3. Material description

During the recycling process of plastics, there is a foreseen reduction of properties [37]. Therefore, measures need to be taken in order to prevent this degradation, such as adding glass fibre and adding virgin material. Glass fibre can significantly increase the property of recycled polymers, especially along the printing direction, but it is difficult for implementation as it could cause toxicity [38]. Unlike adding glass fibre, mixing virgin and recycled material cannot provide the composition with equal property as virgin material, the degradation can only be reduced but not completely compensated [27]. However, it requires only the same material as virgin and recycled, and it is easier to implement, thus this approach was chosen for investigation. There are three basic materials for testing:

1. Scolefin 53-G-10 natural: Common plastic based on PP² with 30% glass fibre as reinforcement.
2. Technomelt 3D 6910: A bio-based material with 12% glass fibre as reinforcement.
3. 60%LDPE³ + 40%PPgf: Post-consumer recycled common plastic composition, in which recycled PP is reinforced with 30% glass fibre.

These three plastics were mixed with their recycled materials in 4 different ratios. Besides, an additional test was carried out with *Technomelt 3D 6910* regrading recycling rounds⁴, in order to provide an insight of property degradation. In total, there are 15 blends, and detailed settings are presented in Table 2.1.

²Abbreviation of Polypropylene

³Abbreviation of Low-density Polyethylene.

⁴The printing with virgin material is 0 round, then the product is shredded as a material for reprinting, the re-printed outcome is 1st round, this process can be repeated several times, 2nd, 3rd, etc.

Composition test with mix-ratio (virgin/recycled)				
<i>Scolefim 53-G-10 natural</i>	100% 0%	75% 25%	50% 50%	25% 75%
<i>Technomelt3D 6910</i>				
60%LDPE+40%PPgf				
Recycling round test				
<i>Technomelt3D 6910</i>	1 st round	2 nd round	3 rd round	

Table 2.1: Materials for testing with different compositions and recycling rounds

2.4. Research method

The research can be divided into two stages: Material test and numerical modelling. To start with the first stage, experiments were carried out to evaluate the candidate materials and derive engineering properties of the selected material. Afterwards, these properties were utilized for derivation of inputs for the second stage. However, because of the time limitation and the schedule of the printer, these two stages were carried out in parallel. The numerical modelling at the beginning of the research was based on the properties used in previous projects [35].

Additionally, a global and a local coordinate system is defined for the interpretation of the results from material tests, and for the numerical analysis. The xy plane in the global coordinate system is defined as the plane to which the nozzle of the printer is perpendicular, and the z axis is the extrusion direction of the printed product. The local coordinate system is defined as x axis coincides with printing direction, z axis coincides the normal to the printed wall (Fig. 2.2).

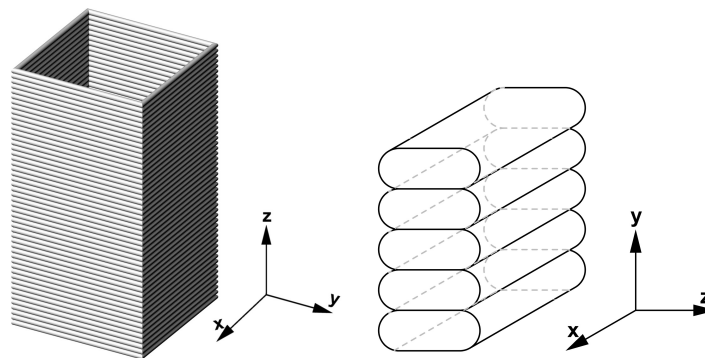


Figure 2.2: Coordinate system utilized in the research. Left: global coordinate system. Right: local coordinate system

2.4.1. Material test

The variety of mixtures for testing is relatively large, especially taken into account the orthotropic behaviour of 3D printed product. Therefore, it is more efficient to choose one property as indicator to give a general view of the material. Tensile property along the printing direction is selected as the indicator since it can represent the general mechanical behaviour of a material. Consequently, the material test contains two parts:

1. *Preliminary tests*: For each blend in Table 2.1, the tensile properties along the printing direction were tested. Based on the results, an evaluation was presented with respect to stiffness, strength, deformation and creep. Then the most promising candidate was selected for the next part.
2. *Basic property tests*: The selected material was tested to derive several other properties for structural design purpose. In addition, double-layer printing products with this material were also tested in order to provide an overview of multi-layer printing.

The geometries for producing the samples were printed with large scale 3D printer *Kamer Maker 2* at *Aectual*, Amsterdam. Then they were cut into planar sheets with oscillating tool and delivered to *Schrijver B.V.*, Almerer. The final samples were produced by cutting the sheets with waterjet. Unlike previous researches, laser cut was not used, because both *Scolefin 53-G-10 natural* and *60%LDPE 3+40%PPgf recycled* were not possible to be cut with laser. This might be related to the glass-fibre content of the material. Besides, the heat generated by the laser during the cutting could affect the results since plastics are quite sensitive to temperature.



Figure 2.3: Preparation for the samples. Left: Printed geometry for preliminary test. Right: Water cutting machine at Schrijver B.V.

The material tests were carried out at the *Materials Science and Engineering laboratory at the Faculty of Mechanical, Maritime and Materials Engineering (3mE)*, TU Delft. There was at least 14 days gap between printing and testing in order to let the material cure sufficiently [35]. The results were processed in accordance with basis of structural design [39]. The statistical foundation used in the processing is presented in Appendix B. Moreover, in many cases the test result is affected by the machinery imperfection, such as toe effect. It need to be modified by extrapolating the first linear part of the output curve to get correct results [40]

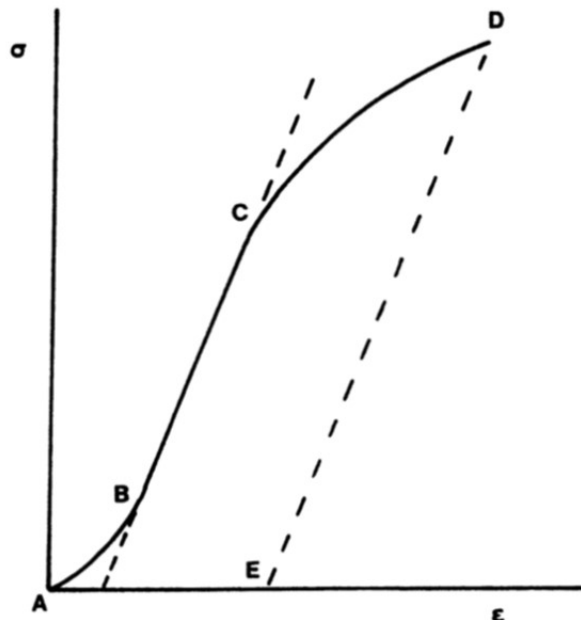


Figure 2.4: Toe effect in stress-strain curve. [40]

2.4.2. Numerical modelling

In the numerical modelling stage, FEM⁵ software is used for analysis and development of optimisation methodology. Test results of a selected material need to be sorted out and transformed into engineering inputs for elements. Two FEM software products are utilized within the research: CalculiX is an light weight open sources software [41]. 2.12, the latest version, was used at the beginning of this project. However it has a bug when calculating the norm of shell elements, thus version 2.08 was used at the late stage. It has already been proved as a good tool for FEM analysis in the previous research [35], but it still has drawbacks, such as no graphic user interface, since it is not developed for commercial purpose. Therefore, ANSYS 17.1 was also used for a quick check of the results derived from CalculiX. Despite these being two products with different calculation algorithm, the inputs for calculation are exactly the same and result difference is within the acceptable range.

Rhinoceros with Grasshopper plug-in has been also used during the research for multiple purposes. It is convenient to make parametric models which saves plenty of time during the attempts at the start of the research. Together with Guanaco package developed by Baran, Tentech, it is easier to generate 2D and 3D meshes by calling Gmsh. Moreover, it is also suitable for visualisation of the outcome generated by FEM software, and as a connection between CalculiX and ANSYS.

The cooperation and utilization among several tools is accomplished by scripting with Python, which is one of the most popular programming languages since 2003 [42]. In Grasshopper on Rhino 5, the Python package has a memory leakage problem, which makes the memory usage continues to increase and slow down the operation speed while calling a Python script, which contains the usage of Grasshopper Python library, multiple times. This is a widely known issue and was mentioned in previous work [35]. This problem is fixed in Rhino 6 WIP with a new Python syntax library, however, most of the scripts are written externally and separately as individual file to make it easier for check and debug.

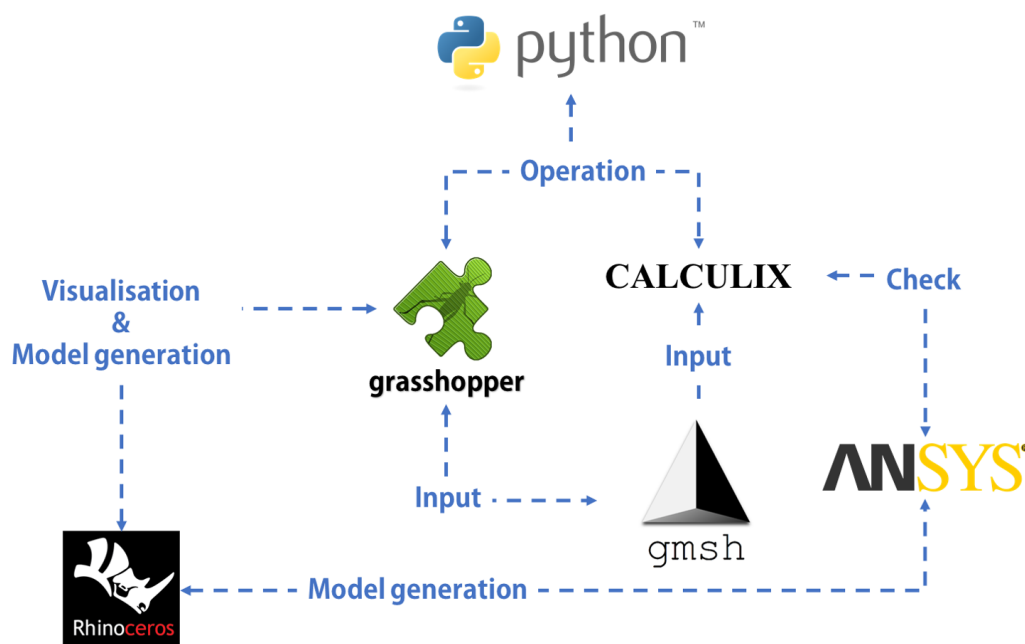


Figure 2.5: Integration of software products utilized in the research

⁵Abbreviation of Finite Element Modelling

2.5. Outline of the contents

In this section, an outline of the structure and main points of this report is presented:

- **Chapter 3 and 4** present material tests, including evaluation, results and issues. The preliminary test is presented individually, because it is the start point of the whole project and provides basic information for the later research.
- **Chapter 5** contains the derivation of engineering inputs for numerical modelling and validation based on the material tests.
- **Chapter 6** talks about the design methodology regarding a conceptual optimisation approach for the 3D print moulds. A numerical example is included for illustration.
- **Chapter 7** includes a case study validating the implementation of the methodology.
- **Chapter 8, 9 and 10** are discussion, conclusions and recommendations respectively.

3

Preliminary test

3.1. Test description

The preliminary test contains three parts regarding the tensile properties along the printing direction: The first one is a standard axial tensile test with respect to different composition ratio between virgin and recycled material. The resultant force-displacement curve is used for deduction of indicated properties for comparison and evaluation. Two testing speed were utilized, 0.5 mm/min and 10 mm/min. The second test scheme uses the same setting as the first one, but is related to different recycling rounds and only applied to *Technomelt 3D 6910*. The final one is creep test, during which a predefined load close to the maximum load derived from the previous test is applied on the sample in axial direction for 15 minutes, and the elongation of the sample is monitored to determine the creep sensitivity of the test material. To carry out the test, the sample is designed in accordance with ISO 527-4 standard [43] with adjusted dimensions. 25 samples are needed for testing, including 10 samples for each speed of the standard axial tensile test and 5 samples for the creep test. More details are in the Table 3.1 and the application of the test is shown in Figure 3.1.

Preliminary test settings			
Sub-test name	Test speed or duration	Sample number	Test equipment
Standard tensile test	0.5mm/min	10	Zwick Z100
	10mm/min	10	
Creep test	15 min	5	Zwick Z010

Test direction
Along the printing direction (Longitudinal direction), x direction in local coordinate system

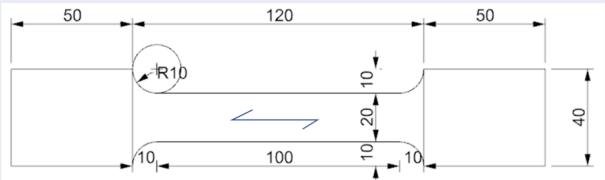
Sample shape and dimensions


Table 3.1: Settings for preliminary tensile test

Not all of the samples were tested due to the time limitation, printing quality and cut quality, but the results are sufficient to get trend of the property change and make a selection.

3.2. Test results

The results are interpreted with composition tests regarding three different basic materials, recycling round test and creep test. Each basic material is compared with respect to several indicator properties: the maximum standard force applied on the sample and the corresponding displacement,



Figure 3.1: Application of the preliminary test

stiffness, and the elongation¹ during the creep test. The units for these properties are listed in Table 3.2.

Property name	Unit
Maximum strength	N
Displacement	mm
Stiffness	N/mm
Creep behaviour	mm

Table 3.2: Unit of properties for comparison

3.2.1. Composition test of Scolefin 53-G-10 natural

The force-displacement curve of *Scolefin* has a general pattern as piecewise curve. It consists of two linear part and a non-linear part as transition (See Figure 3.2). The specimens failed brittlely and most of them break at the location where the cross-sectional area changes.

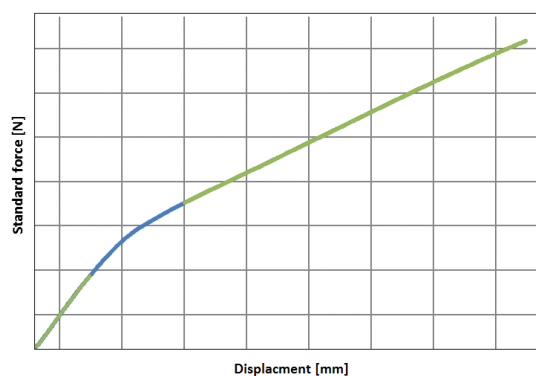


Figure 3.2: Force-displacement curve of Scolefin 53-G-10 natural. Green: linear parts. Blue: non-linear transition.

Under testing speed of 10 mm/min (Figure 3.3, Right), all tested compositions have a relatively large deviation among samples with respect to the maximum force: the difference is around 1000N.

¹The load applied to the sample varies with different compositions regarding the maximum load it can bear, thus the results are compared by interpolating the corresponding elongation to the minimum load applied to each basic material.

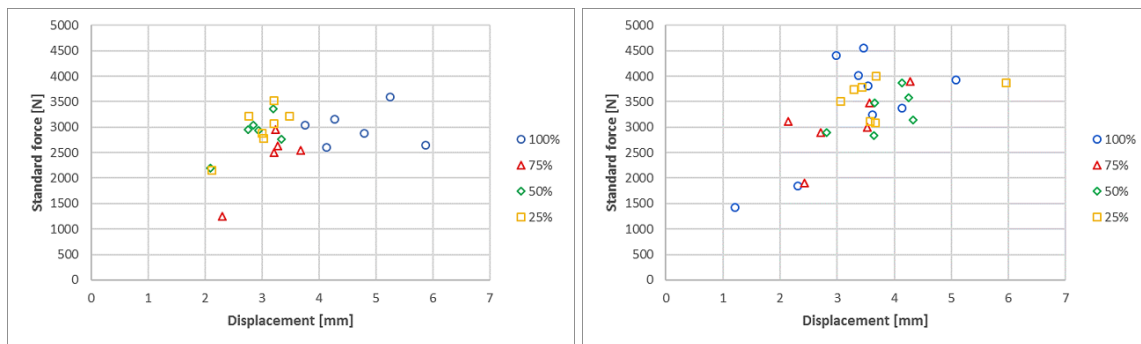


Figure 3.3: Maximum force and corresponding displacement regarding different composition of Scolefin 53-G-10 natural. Left: speed 0.5 mm/min. Right: speed 10 mm/min (Percentage is the content of virgin material)

This is caused by the inhomogeneity of the material. The blend with 100% virgin material has a more obvious non-uniform distribution due to its poor cutting quality. The scatter of the blend with 75% virgin material is also not distributed evenly because some samples delaminated during the test (Figure 3.4, Left). The delamination is also observed during the printing process (Figure 3.4, Right), which means the shrinkage of printed product is more severe with this ratio. The other two blends have relatively less deviated results with respect to the corresponding displacement at maximum force, in spite of the difference of maximum force is still relatively large. Despite the influence of quality of the samples, the strength of the material is still related to the content of recycled material, i.e. the more recycled material in the composition, the lower maximum strength it has. However, when the blend consists of 25% virgin material and 75% recycled material, its strength rises again and is nearly equal to that of blend contains 50% recycled material. The ratio between virgin and recycled plastics used by recycling industry for recycling polypropylene is also around 1:3 [44].

As for the test with testing speed of 0.5 mm/min (Figure 3.3, Left), the deviation of maximum strength still exists, but less than that of the test with speed of 10 mm/min. Besides, because low speed test gives more time for defects in the samples to expose, the influence of the shrinkage and corresponding delamination is bigger. Consequently, the results of the blend with 75% virgin material has an even lower value than that of the blend with 50% virgin material.

As mentioned before, the force-displacement curve of *Scolefin 53-G-10 natural* has two linear sections. The first linear part ends at location with a standard force around 1000N, which is a higher value than the maximum strength of all the compositions of *Technomelt 3D 6910* and *60%LDPE 3+40%PPgf recycled*. Therefore, this part is more suitable for structural design, and the stiffness is investigated only for this part. From the results in Table 3.3, it is clear to see the stiffness are almost equal except for the blend with 100% virgin material, which is caused by the poor cutting quality. This indicates that the ratio between virgin and recycled material has a relatively small effect on the stiffness of the first linear part. It should be noted that the stiffness is derived from the approximate curve function and is limited by the decimal places. It is sufficient for evaluation in preliminary test, and a more accurate value is used for deriving engineering properties in Chapter 5. Moreover, the value of standard deviation equals to zero depends on decimal places and should be only regarded as an indication of very small deviation among samples.

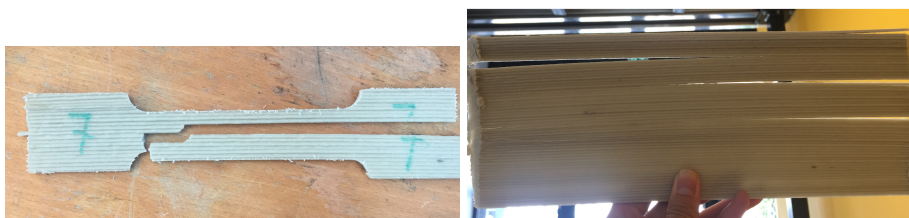


Figure 3.4: Delamination with virgin/recycled ratio of 75%/25%. Left: delamination of the sample. Right: delamination of the printed sheet

Stiffness comparison of Scolefin 53-G-10 natural								
Composition (Virgin/Recycled)	100/0		75/25		50/50		25/75	
Testing speed [mm/min]	0.5	10	0.5	10	0.5	10	0.5	10
Maximum value [N/mm]	2000.00	2500.00	2000.00	2500.00	2000.00	2000.00	2500.00	2500.00
Minimum value [N/mm]	1428.57	1666.67	2000.00	2000.00	2000.00	2000.00	1666.67	1428.57
Average value [N/mm]	1690.48	1972.22	2000.00	2200.00	2000.00	2000.00	2027.78	1932.54
Standard deviation [N/mm]	234.90	305.81	0.00	273.86	0.00	0.00	243.98	363.41

Table 3.3: Stiffness comparison with respect to different composition of Scolefin 53-G-10 natural.

3.2.2. Composition test of Technomelt 3D 6910

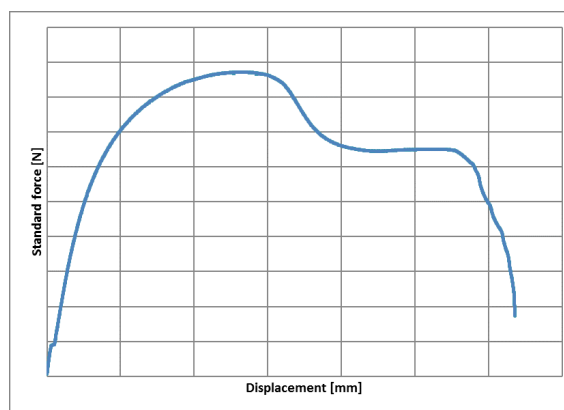


Figure 3.5: Force-displacement curve of Technomelt 3D 6910.

Stiffness comparison of Technomelt 3D 6910								
Composition (Virgin/Recycled)	100/0		75/25		50/50		25/75	
Testing speed [mm/min]	0.5	10	0.5	10	0.5	10	0.5	10
Maximum value [N/mm]	243.90	294.12	227.27	270.27	200.00	232.56	208.33	243.90
Minimum value [N/mm]	243.90	243.90	188.68	192.31	196.08	185.19	172.41	166.67
Average value [N/mm]	243.90	277.54	207.98	248.74	198.04	219.16	190.37	212.18
Standard deviation [N/mm]	0.00	16.02	27.29	27.96	2.77	15.74	25.40	24.11

Table 3.4: Stiffness comparison with respect to different composition of Technomelt 3D 6910.

Technomelt 3D 6910 has a non-linear force-displacement curve (Figure 3.5), and all the samples break in ductile failure with a relatively large displacement² and a very obvious plastic deformation appears during the testing (Figure 3.6). In the test with a speed of 10 mm/min (Figure 3.7, Right), a decrease of the maximum strength can be observed with the increase of the content of recycled material in the first three blends. Blend with 25% virgin material also has a raised value in maximum strength, and it is almost equals to that of blend with 75% virgin material. However, its corresponding displacement at maximum force is also larger than that of the other blends, and the values are more

²For the sake of saving time, only two samples were tested in the speed of 0.5mm/min with a predefined threshold. This threshold should make the force-displacement curve passes the the point with maximum strength.

varied among samples. Moreover, compared to the results in the previous research [35, 36], the deviation of the results is smaller thanks to the improvement of the printing quality. But this is at expense of a decrease of maximum strength. The 100% virgin material with 28 days old had a strength over 1200N [35], but the same property got in this research is less than 1000N.



Figure 3.6: Plastic deformation with narrowing while testing Technomelt 3D 6910.

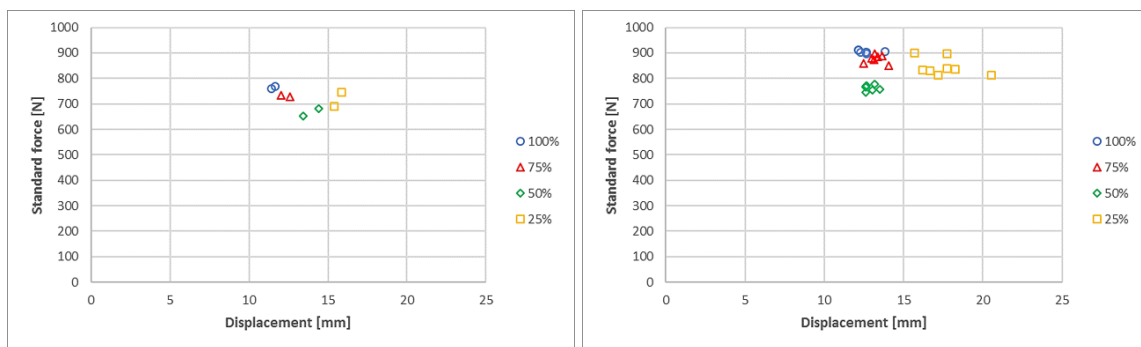


Figure 3.7: Maximum force and corresponding displacement for different compositions of Technomelt 3D 6910. Left: speed 0.5 mm/min. Right: speed 10 mm/min (Percentage is the content of virgin material)

As for the results with a testing speed of 0.5 mm/min (Figure 3.7, Left), the trend of the property changes along the change in the recycle material content is clearer. The maximum strength decreases with the increase in the content of recycled material until the ratio of virgin/recycled reaches 25%/75%. Besides, the displacement at maximum force continually increases with increase of the recycled material content. Moreover, the stiffness³ shown in Table 3.4 with both testing speed has very small value in spite of a small deviation among samples.

³The stiffness of *Technomelt 3D 6910* is calculated according to ISO 527-1 [45] . $k = \frac{N_{0.25\%} - N_{0.05\%}}{d_{0.25\%} - d_{0.05\%}}$

3.2.3. Composition test of 60%LDPE 3+40%PPgf recycled

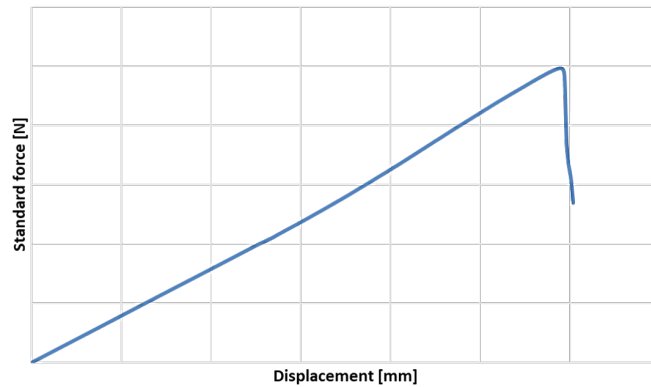


Figure 3.8: Force-displacement curve of 60%LDPE+40%PPgf recycled.

The force-displacement curve of 60%LDPE+40%PPgf is linear like, and all the tested samples fails brittlely. It can be clearly observed in Figure 3.9, the material has very deviated results among the samples. Although its difference regarding the maximum strength among the samples is less than that of *Scolefina*, its highest strength is also much less. In the scatter with testing speed of 10 mm/min (Figure 3.9, Right), a large difference of displacement is observed. Moreover, the decreases in maximum strength is dramatic once the recycled material is added, but the maximum strength of the blends containing recycled material in each ratio is more or less the same.

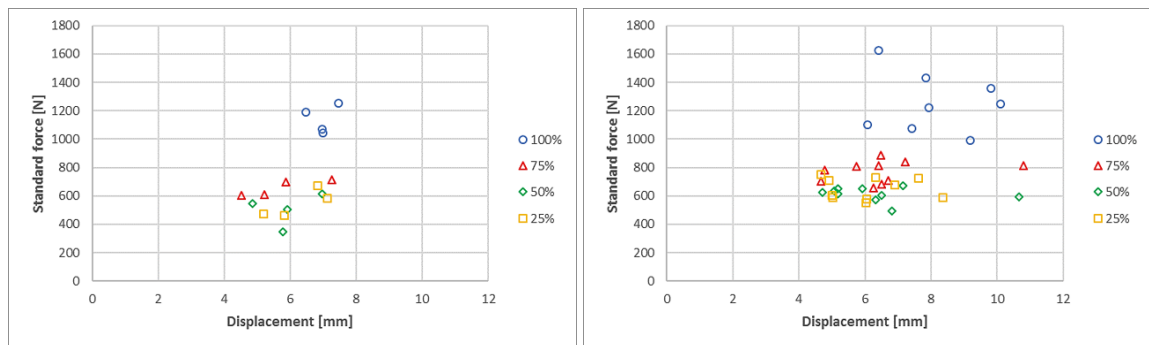


Figure 3.9: Maximum force and corresponding displacement regarding different composition of 60%LDPE 3+40%PPgf recycled. Left: speed 0.5 mm/min. Right: speed 10 mm/min (Percentage is the content of virgin material)

The stiffness of each composition of 60%LDPE+40%PPgf recycled has a small deviation among samples, but this because its strength is already relatively low. Difference between highest and lowest value shows this material is less homogeneous. Some of the value in strength scatter are even less than that of *Technomelt 3D 6910*.

Stiffness comparison of 60%LDPE+40%PPgf recycled								
Composition (Virgin/Recycled)	100/0		75/25		50/50		25/75	
Testing speed [mm/min]	0.5	10	0.5	10	0.5	10	0.5	10
Maximum value [N/mm]	196.08	322.58	163.93	185.19	131.58	147.06	138.89	188.68
Minimum value [N/mm]	156.25	151.52	117.65	84.03	58.82	50.00	99.01	111.11
Average value [N/mm]	177.37	204.95	145.02	146.19	90.05	102.79	111.65	137.40
Standard deviation [N/mm]	16.32	56.83	19.52	31.39	30.43	30.86	18.67	26.99

Table 3.5: Stiffness comparison with respect to different composition of 60%LDPE+40%PPgf.

3.2.4. Recycling round test of Technomelt 3D 6910

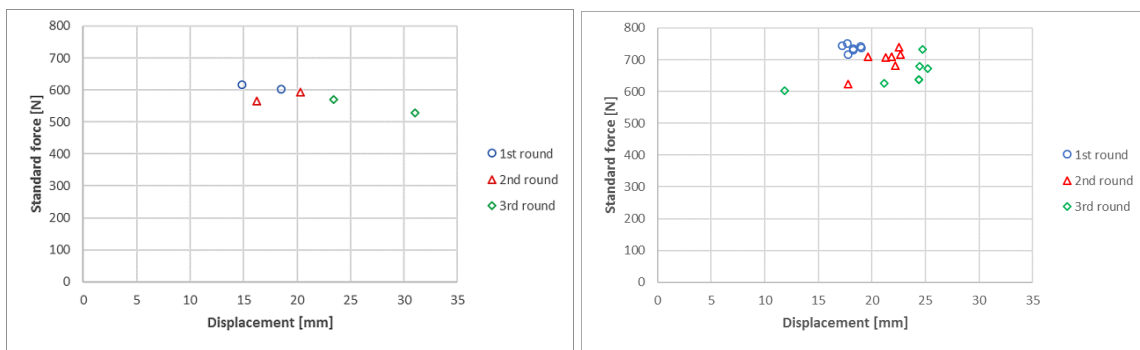


Figure 3.10: Maximum force and corresponding displacement with respect to recycling rounds of Technomelt 3D 6910. Left: speed 0.5 mm/min. Right: speed 10 mm/min

It can be observed in Figure 3.10, with the increase of the recycling rounds, the maximum force is reduced around 50N per round, and the corresponding displacement increases in the meantime. The maximum strength does not decrease much, however, the quality of the samples also decreases. Visible voids and uneven surface which reduces the homogeneity can be observed on the sample, and it is clearer to see them on the printed sheet before cutting the samples out (Figure 3.11). In the tests with both testing speeds, the deviation among the samples increases as the number of recycling rounds increases. Especially, two points in the test with testing speed of 0.5 mm/min of 3rd round blend deviates a lot regarding the displacement. Except for the influence of recycling round, the other cause is that they were tested with different machines with different clamping method.



Figure 3.11: Bad quality of sheet of Technomelt 3D 6910 with multi-round printing

With the increase of recycling rounds, the stiffness is reduced slightly, and deviation of the results

Stiffness comparison of Technomelt 3D 6910						
Recycling round	1 st round		2 nd round		3 rd round	
Testing speed [mm/min]	0.5	10	0.5	10	0.5	10
Maximum value [N/mm]	172.41	208.33	138.89	175.44	109.89	161.29
Minimum value [N/mm]	151.52	181.82	135.14	144.93	58.82	142.86
Average value [N/mm]	161.96	193.87	137.01	160.77	84.36	150.25
Standard deviation [N/mm]	14.78	10.78	2.65	13.22	36.11	6.78

Table 3.6: Stiffness comparison with respect to recycling round of Technomelt 3D 6910.

also increases, especially in the test with speed of 0.5 mm/min (Table 3.6). With this speed, the average stiffness is already below 100N/mm.

3.2.5. Creep test

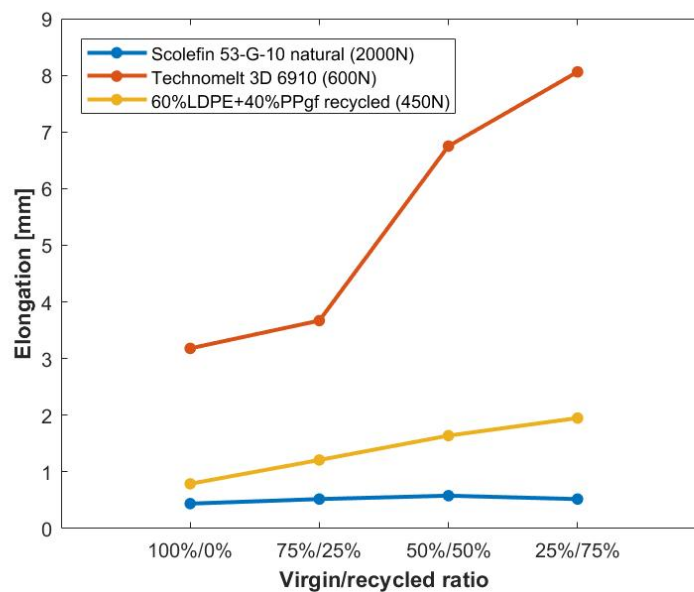


Figure 3.12: Elongation of different basic material with respect to recycled material content.

The results of creep tests are compared in Figure 3.12. *Scolefin 53-G-10 natural* has less creep with all the compositions compared to the other two basic materials, and the elongation is less than 1 mm. In general, the creep increases with the increase of recycled material, however, it has a decrease with the blend containing 75% recycled material.

The creep of *Technomelt 3D 6910* is more significant, and the samples can only bear 600N. The more recycled material contained in the blend, the more obvious creep can be observed. It can be seen there is a dramatic increases of elongation from the blend with 25% recycled material to the blend with 50% recycled material. The elongation with of blend contains 75% recycled material is 8.06 mm, which is almost 7% of the effective length⁴.

⁴See Appendix E for the definition of effective length.

As for *60%LDPE 3+40%PPgf recycled*, it has much less creep than *Technomelt 3D 6910* but more than *Scolefin 53-G-10 natural*. However, the load it can bear is 450N, which is also relatively small. There is a constant increase of the creep with respect to the increase of recycled material content.

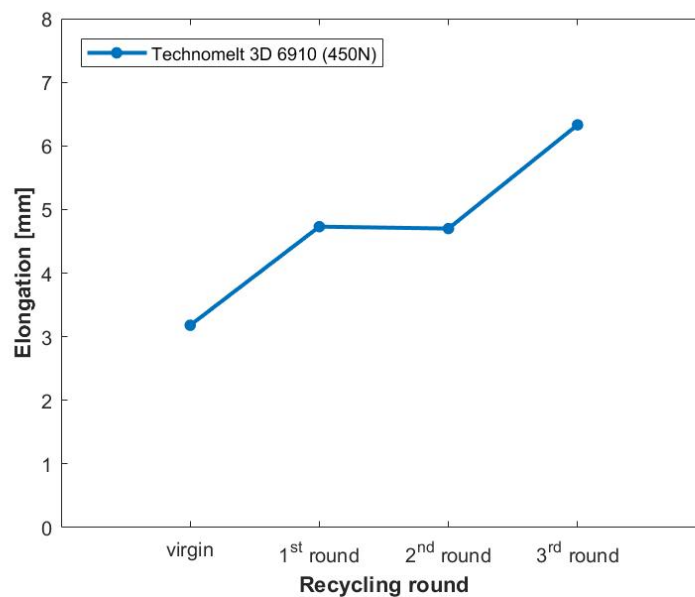


Figure 3.13: Elongation of Technomelt 3D 6910 with respect to recycling rounds.

In Figure 3.13, the creep behaviour of the virgin material is added for comparison. A dramatic increase of creep is observed between the virgin material and 1st round recycled material. The similar increase can be also observed between 2nd round recycled material and 3rd round recycled material. This means the material is hardly to be used as structural material for long time purpose. Moreover, due to the limitation of the sample size, only 2 of each blend, it is suggested to carry out more tests in order to get a better understanding of the creep behaviour.

3.3. Evaluation and selection

Basic material *Scolefin 53-G-10 natural* is the stiffest, and strongest candidate among three basic materials. It can bear relatively high load, and the effect of long term loading is small. Besides, the load applied on the sample during creep test is 2000N and the value used for designing, which is below 1000N, is the first linear part as mentioned in previous section. Therefore, the effect of creep can be neglected.

Both *Technomelt 3D 6910* and *60%LDPE 3+40%PPgf recycled* can bear a smaller load compared with *Scolefin 53-G-10 natural*. Despite the printing quality with *Technomelt 3D 6910* is relatively good (Figure 3.15.) and the results indicates a good homogeneity, it has a large deformation when loaded, and it is very sensitive to creep. *60%LDPE 3+40%PPgf recycled* is not suitable for structural use, because both the load it can bear and the stiffness are very low. Besides, during the test with this material, 45 degree shear failure appears in some samples (Figure 3.14), which means the property of the sample along the printing direction is as low as that across the printing direction.

As for the recycling rounds tests of *Technomelt 3D 6910*, the properties have an expected decrease. After first round recycling with around 25% strength decrease compared to virgin material, there is 50N strength decrease each round which is not very large. However, the homogeneity and printing quality are reduced considerably in 2nd and 3rd round. Therefore it is better to use it only with 1st recycling round.

A trend can be clearly seen in the property results of three basic materials, which is a raise of properties with virgin/recycled ratio equal to 25%/75%. This phenomenon can be very promising for

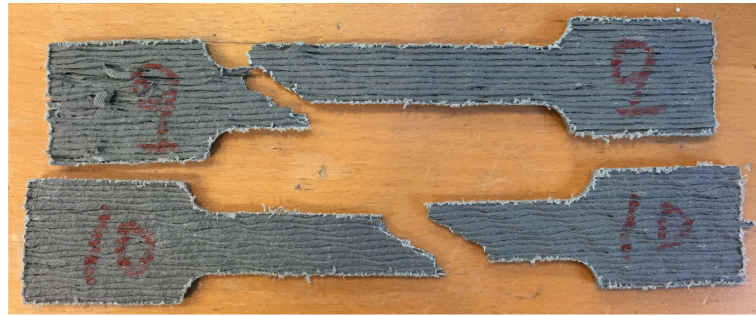


Figure 3.14: Failure in 45 degree during the tensile test of 60%LDPE 3+40%PPgf recycled.



Figure 3.15: Decent printing quality with Technomelt 3D 6910.

using recycled material if the homogeneity with this composite ratio is improved.

Among all the materials and compositions, blend of *Scolefim 53-G-10 natural* with a virgin/recycled ratio of 50%/50% is the most promising candidate for the following design. Its property is less deviated among samples than the other compositions based on the same basic material. It has high strength and stiffness, and its sensitivity with respect to creep behaviour is also very small. Therefore it is selected as the material composition for the further property tests and structural design.

4

Other property tests

4.1. Test description

Based on the results and evaluation of the preliminary test, mixture *Scofelin 53-G-10 natural* with a virgin/recycled composite ratio of 50%/50% was chosen to be tested for other properties. Because of the time and resource limitations, it is not possible to test all the mechanical properties of this material. Therefore, the test scale is limited to investigation of basic properties which can be used for deriving engineering inputs in the modelling phase. Because the printed product exhibits highly orthotropic behaviour, the tests are carried out in two directions: along the printing direction and across the printing direction. For the sake of simplicity, these directions will be represented by longitudinal direction and transverse direction respectively in the rest of the thesis. The selected basic properties are:

- Tensile strength and stiffness
- Flexural strength and stiffness
- Shear strength

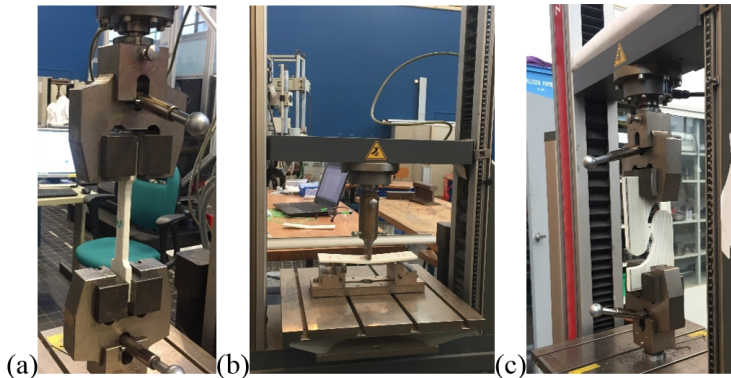


Figure 4.1: Application of the property tests. (a)Standard tensile test. (b)Three points bending test. (c)Modified shear test.

For each test type regarding different directions, 20 samples were required, including 10 samples for testing speed of 0.5 mm/min and testing speed of 10 mm/min each. In addition, double-layer samples were also printed and tested with the same test settings in order to investigate the properties with multi-layer printed product (Fig. 4.2). However, only the properties in the longitudinal direction with a few samples were tested due to a malfunction of the printer during the production of the double-layer geometry.

It needs to be noted that during the testing of transverse property of single-layer samples, especially transverse tensile test, some of them failed at clamps. The reason for that is the production process,



Figure 4.2: Geometry for producing double-layer samples.

during which the part at clamps contains the layers that are being printed first. These layers are brighter compared with the other layers and have lower strength (Fig. 4.3). These parts have a relatively big influence on the results, therefore, they were removed with hammer before testing. The rest part should still have enough area for clamping.



Figure 4.3: The influence of first printed layers. Up: the first printed layers in the printed product. Down: the failure at clamps.

4.1.1. Tensile test

The samples designed for testing the tensile property have same dimensions as used in preliminary test in accordance to ISO 527-4 standard [43]. The test of single-layer samples was performed in transverse direction, and the test of double-layer samples, including 2 samples for each testing speed, was performed in longitudinal direction. The output is a force-displacement curve, and not all the samples with single-layer were tested due to the time limitations and printing quality. More details of the tensile test setting are in Table 4.1.

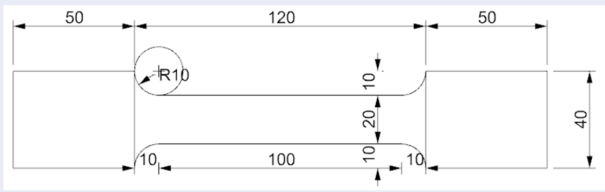
Tensile property test			
Sub-test name	Test speed or duration	Sample number	Test equipment
Standard tensile test	0.5mm/min	10	Zwick Z100
	10mm/min	10	
Test direction			
Transverse direction			
Test method			
Standard tensile test			
Sample shape and dimensions [mm]			
			

Table 4.1: Settings for tensile test.

4.1.2. Flexural test

The samples for three point bending test was designed according to ISO 178 standard [46]. The span between supports is 115 mm, which is same as that in the previous research [35]. For single-layer samples, the test was performed in both longitudinal and transverse directions. As for the double-layer samples, including 2 samples for each testing speed, the test was performed in longitudinal direction. The output is a force-displacement curve, and not all the samples with single-layer were tested due to the limitation of time and printing quality. More details of the flexural test setting are in Table 4.2.

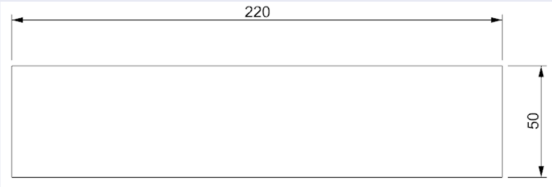
Flexural property test			
Sub-test name	Test speed or duration	Sample number	Test equipment
Standard tensile test	0.5mm/min	10	Zwick Z100
	10mm/min	10	
Test direction			
Longitudinal and transverse direction			
Test method			
Three points bending test			
Sample shape and dimensions [mm]			
			

Table 4.2: Settings for bending test.

4.1.3. Shear test

The method for testing the shear properties is based on the work of Bao and Wierzbicki [47]. It is easier to implement thanks to applying axial load instead of direct shear on the sample, and it was proven to be applicable in the previous researches [35, 36]. The dimensions of the sample have been adjusted to suit the size of printed product. Similarly, properties regarding both directions were tested for single-layer samples and property in longitudinal direction was tested with double-layer samples. More details of the shear test setting are in Table 4.3.

Shear property test			
Sub-test name	Test speed or duration	Sample number	Test equipment
Standard tensile test	0.5mm/min	10	Zwick Z100
	10mm/min	10	
Test direction			
Longitudinal and transverse direction			
Test method			
Bao and Wierzbicki method (2004).			
Sample shape and dimensions [mm]			

Table 4.3: Settings for shear test.

4.2. Test results

Because of the special cross-sectional geometry of the printed samples and complex orthotropic behaviour, the results are presented in the form of cross-sectional force-displacement properties per running millimetre (Table 4.4), which is in the same manner as in the previous research [35].

In-plane strength	$\frac{F}{b} \left[\frac{N}{mm} \right]$
Out-of-plane strength	$\frac{M}{b} \left[\frac{Nmm}{mm} \right]$

Table 4.4: Cross-sectional properties per running millimetre

Except for the results of the shear test, each property is presented separately with a plot in the following subsections. The y axis is the relevant cross-sectional property, and the x axis is the relative displacement between clamps in tensile test or the movement of the head in bending test. Besides, the gradient of the curve can represent the stiffness of the relevant property, the steeper it is the higher the stiffness. Additionally, the results of a preliminary tensile test of the chosen material are shown as a reference. As mentioned before, only the first linear part is used and compared since it covers the range relevant for practical design. The endpoint of the curve regarding the displacement is in accordance with different definitions of yielding point for different properties [40, 46, 48].

4.2.1. Tensile test

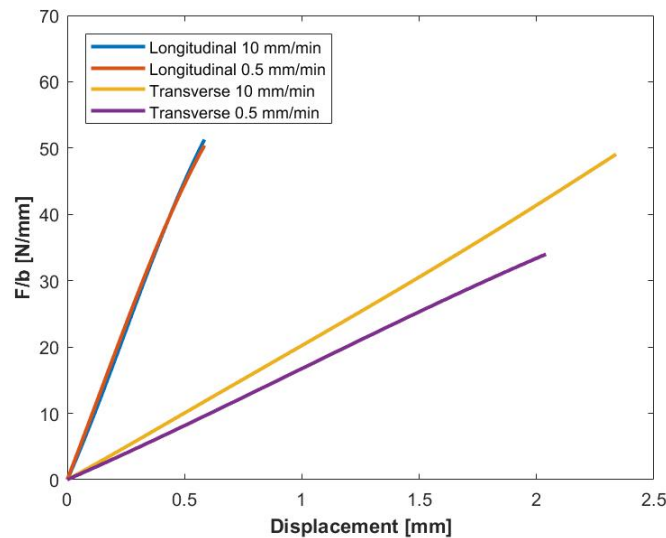


Figure 4.4: Tensile test results of single-layer samples

Significant orthotropic behaviour in tensile property can be observed in Fig. 4.4. The stiffness in longitudinal direction is much higher than that in transverse direction. The results with respect to different testing speed are much deviated in transverse direction. Both strength and stiffness is much lower with a lower testing speed. Besides, the samples even breaks with a smaller displacement. This means there are more defects in the transverse direction, and loading with a low speed will make these defects exposed.

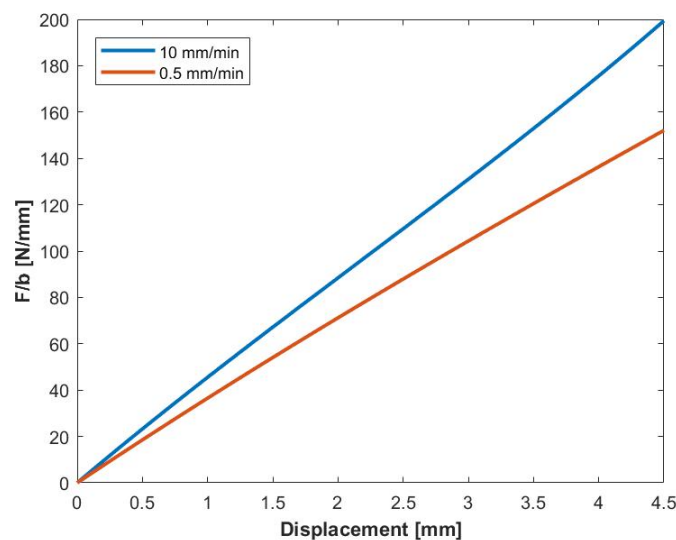


Figure 4.5: Tensile test results of double-layer samples

As for the tensile test of double-layer samples, the property difference regarding the testing speed is more obvious in longitudinal direction. Moreover, unlike the piecewise force-displacement curve of tensile property in the longitudinal direction of single-layer samples, the curve is linear like with double-layer samples in the same testing direction.

4.2.2. Bending test

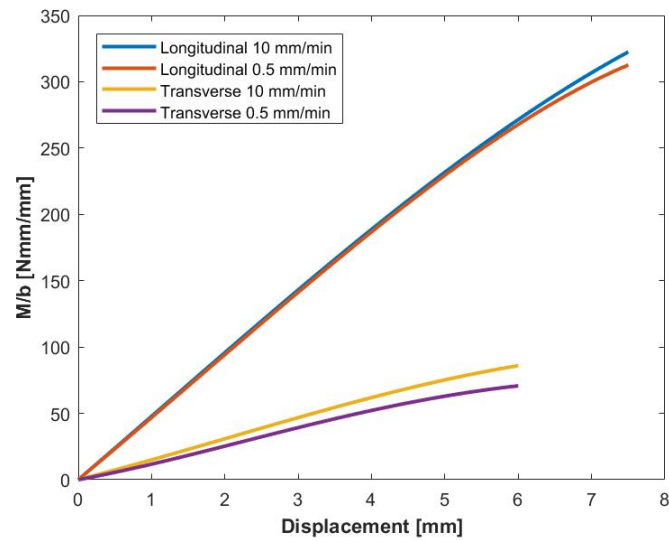


Figure 4.6: Bending test results of single-layer samples

Likewise, the results of bending test with single-layer samples show an orthotropic behaviour similar to the tensile test. However, the deviation related to the testing speed is smaller. In general, the results of low speed test have a smaller value that of high speed test.

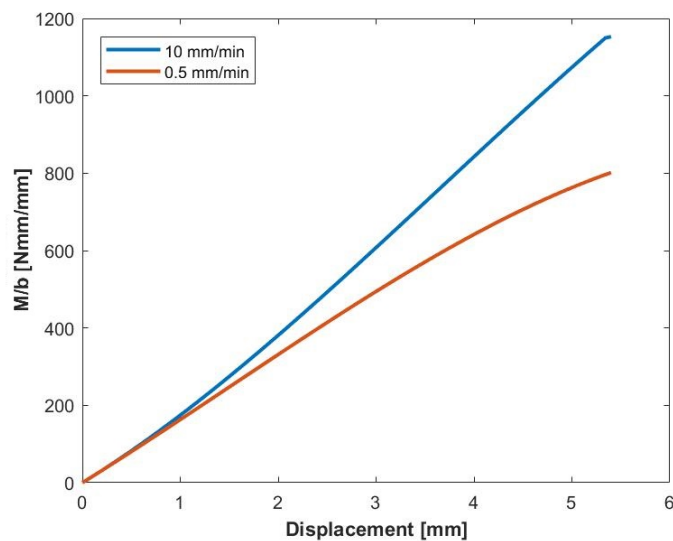


Figure 4.7: Bending test results of double-layer samples

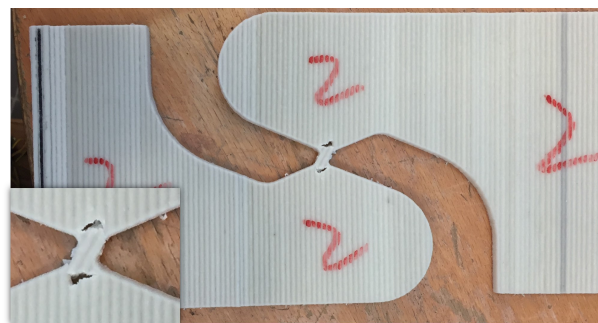
The result deviation caused by the testing speed is much higher in case of double-layer samples. With the increase of the displacement, the deviation also increases.

4.2.3. Shear test

Based on the result of shear test, it is hard to conclude the stiffness against the shear deformation because of the selection of the testing method. Besides, during the shear test in transverse direction, most of the samples failed with delamination or at the other location instead of the test point (Fig. 4.8, Down). Therefore, only the maximum shear strength reached by the samples can be derived (Table 4.5). However, the scope of the structure for designing in this research is moulds, and the shear failure is not dominant in case of this type of structures. Besides, the values of shear stress obtained from FEM on the design stage are usually much lower than the values listed in the table. Therefore, the shear behaviour is neglected in this project. It is suggested to explore the shear property with the other approaches in the further work. Moreover, rotation at the shear test point is observed during the test (Fig. 4.8, (a)), this phenomenon indicates a general relation among the properties: Transverse shear strength > Longitudinal tensile strength > Longitudinal shear strength > Transverse tensile strength.

Layer number and direction	Shear strength [MPa]
Single-layer longitudinal direction	30
Single-layer transverse direction	116
Double-layer longitudinal direction	45

Table 4.5: Shear strength.



(a) Rotation of the testing point.



(b) Tensile failure at other location.

Figure 4.8: Failure in shear tests.

4.3. Summary and issues

According to the results presented in the previous section, it is clear that almost all properties are linear like, with plastic deformation occurring only at late stage before fracture. Therefore, these properties can be approximated with a line, which leaves the corresponding Young's modulus constant. In order to embrace potential defects as much as possible, the results with testing speed of 0.5 mm/min are used for numerical modelling and structural design. Besides, the type of structures to be investigated and designed within this research is limited to moulds, thus the safety factor applied for the design is set to 20% of the characteristic yield strength as criteria:

$$X_d = 20\% \times X_k \quad (4.1)$$

Particularly, for the tensile property in the longitudinal direction with single-layer printing, the design value of the yield point is related to the maximum strength instead at the endpoint of the first linear part to prevent a too small value for practical design. The derived design value lies within the design range (Fig. 4.9). In case of designing of other structures with the same material, more safety factors need to be defined [49].

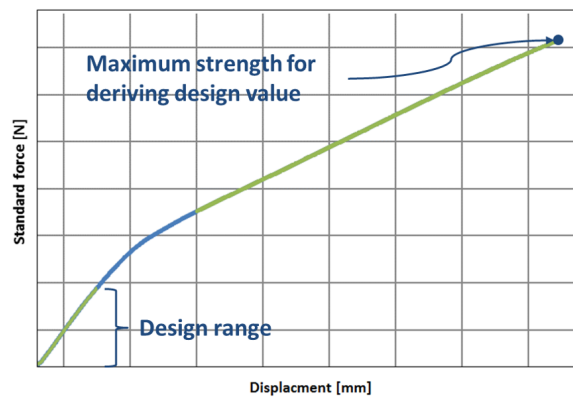


Figure 4.9: Determination of the design value for the tensile property in the longitudinal direction of a single-layer wall.

Layer number	Nominal thickness [mm]	Direction	Property name	Nominal Young's moduli [MPa]	Yield strain $\epsilon_{y,d}$ [mm/mm]	$\frac{E_f}{E_n}$
Single	5	Longitudinal	Tensile	2109.40	0.25%	2.2
			Bending	4723.44	0.32%	
		Transverse	Tensile	392.44	0.35%	3.4
			Bending	1332.34	0.25%	
Double	10	Longitudinal	Tensile	404.11	0.38%	5.2
			Bending	2091.53	0.46%	
		Transverse	Tensile	222.21	0.53%	2.7
			Bending	590.02	0.37%	

Table 4.6: Summary of the design values.

To sum it up, the design values can be defined with nominal thickness (Table 4.6). Because of the constancy Young's modulus, the design value of the strength can be represented by yielding strain, which is more suitable for the modelling with multi-layer shell element in the later numerical design phase (Chapter 5). The missing property of double-layer in transverse direction is derived by interpolation from the other results. The calculation of Young's modulus and corresponding strain¹ is according to the following equations:

¹It is not necessary to calculate the true strain for the tensile property because of the magnitude of the yielding strain is quite small.

Calculation of modulus and strain for tension:

$$E_{normal} = \frac{F}{b} \times \frac{L_{eff}}{td} \quad (4.2a)$$

$$\varepsilon_{tensile} = \frac{d}{L_{eff}} \quad (4.2b)$$

Calculation of modulus and strain for bending:

$$E_{flexural} = \frac{M}{b} \times \frac{L_{bend}^2}{t^3 d} \quad (4.3a)$$

$$\varepsilon_{flexural} = \frac{6dt}{L_{bend}^2} \quad (4.3b)$$

where:

$\frac{F}{b}$ is in-plane strength.

$\frac{M}{b}$ is out-of-plane strength.

t is nominal thickness. 5 mm and 10 mm for single-layer and double-layer respectively.

d is displacement.

L_{eff} is effective length which equals to 116.95 mm².

L_{bend} is distance between supports in bending test, it equals to 115 mm.

According to the results shown in Table 4.6, two issues can be discovered. The first one is in both directions, the Young's modulus calculated from bending test results is higher than that from tensile test:

$$\frac{E_{flexural}}{E_{normal}} > 1 \quad (4.4)$$

This is caused by the anisotropy of the material after extruding from the nozzle of the 3D printer. Three possible reasons are explained below with local coordinate system³:

1. **Nonuniform curing** [35]: This is a view proposed in previous research by Baran, 2016, on a bio-based 3D printing material: *Technomelt 3D 6910*. During the curing process, the outer surface would have a quicker curing speed compared to the central part, and consequently a difference between normal stiffness and flexural stiffness. This phenomenon is time-dependent (Fig. 4.10).

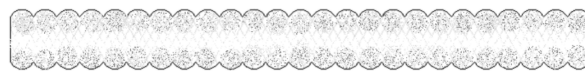


Figure 4.10: Nonuniform curing throughout the cross section [35].

2. **Voids caused by shrinkage**: The *Scofieldin 53-G-10 natural* used for this research has a very significant shrinkage problem during the printing process, which could cause micro-voids in the printed lines. These voids would not be noticeable during the tensile test but would have an influence on bending test. Taken a part of the 3D printed wall in the undeformed state, the neutral plane would be at the centre of the cross-section, but once it is bent, the voids at the upper half of the wall would close under compression and cause larger tensile area due to the force equilibrium. Consequently, the neutral plane would shift upward, and the wall would have a larger flexural stiffness. (Fig. 4.11)

²See Appendix E for the definition of effective length.

³See Section 2.4 for the definition of local coordinate system.

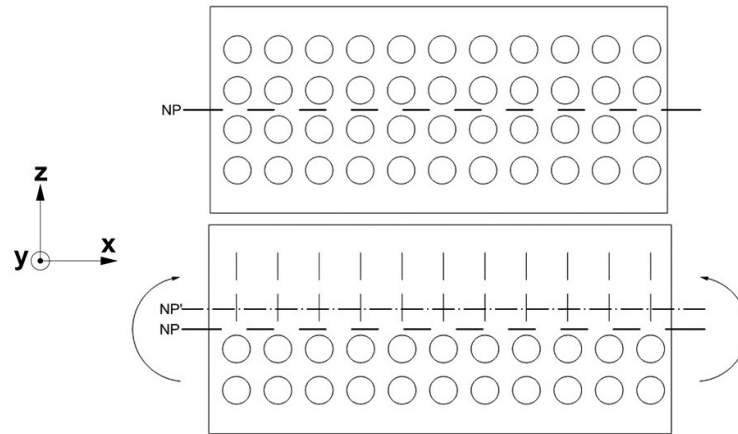


Figure 4.11: Voids caused by shrinkage in a segment of printed line, with local coordinate system. Up: Undeformed state. Down: After bent.

3. **Nonuniform density caused by shrinkage:** The third potential reason is also caused by shrinkage. During the printing process, the glass fibre would flow along the printing direction, which means the reinforcement is much less effective at transverse direction. This causes severer shrinkage at sides, and because the volume of glass fibre doesn't change, the relative glass fibre content ratio is increased and consequently the stiffness at the side parts is increased.

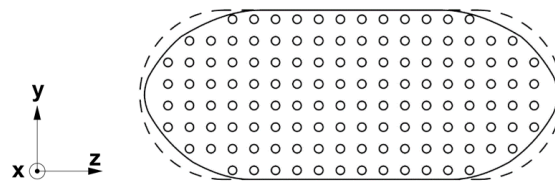


Figure 4.12: Nonuniform density caused by shrinkage, with local coordinate system. Solid line: profile after shrinkage. Dash line: profile before shrinkage. Circle: glass-fibre.

The second issue is related to multilayer printing. The Young's modulus derived from single-layer samples and that from double-layer samples are not identical. It is higher in case of single-layer samples with respect to both tension and bending. The reason behind this phenomenon could be the influence from heating. Plastic is a thermosensitive material, and while printing the second layer, there needs to be at least 1 mm overlap of two layers to ensure sufficient bonding. The part of the existing layer adjacent to the overlap would be reheated, and consequently cause a reduction of the stiffness (Fig. 4.13, Left). Moreover, this feature could also be affected by parity of the layer number. In case of odd layer number, the distribution of the Young's modulus across the section could be asymmetric, and it would affect the test result with placing different side upward on the support (Fig. 4.13, Right).

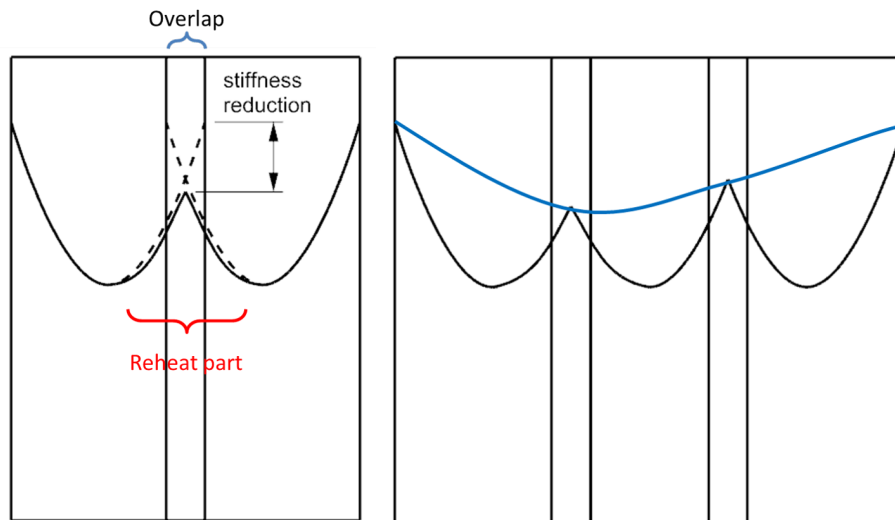


Figure 4.13: Stiffness reduction with multi-layer printing. Left: two adjacent layers with overlap (dash line: E distribution of single layer. solid line: E distribution after second layer printed). Right: three adjacent layers with overlap (blue line: asymmetric E distribution along the cross-section).

5

Numerical modelling

As mentioned in Section 2.4, two FEM software products, CalculiX and ANSYS, were utilized for the numerical modelling. Since CalculiX is the main software and ANSYS was used for validation, only the inputs and settings for CalculiX are described in this chapter. Even though, the material inputs for both software products are identical, and the relative settings, such as element type, can be found in ANSYS documentations [50]. Moreover, since FEM software products are based on same theory in spite of the calculation algorithm might be different, the results generated from both software products should not deviate significantly.

5.1. Objectives

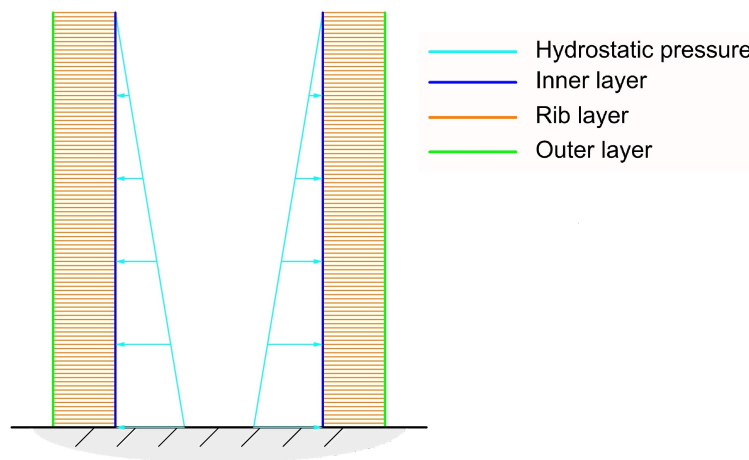


Figure 5.1: Side view of structured mould.

The objective of numerical modelling within this research is to establish a numerical model to simulate complex structured geometry with the selected material. This structured geometry type is limited to moulds for casting relatively large concrete products as mentioned in Chapter 2, and it can be considered as consisting of three parts:

- **Inner layer:** It directly contacts to the concrete, and is subject to the hydrostatic pressure¹ from the concrete. It is in the shape of the outer surface of the concrete product.
- **Rib layer:** Connection between the inner layer and outer layer. It transfers and distributes the load that comes from the inner layer to the outer layer.

¹See Appendix F for the hydrostatic pressure of concrete

- **Outer layer:** The outermost layer which ensures the integrity of the whole structure.

In order to take as much advantage as possible of the flexibility of 3D printing technology, a concept based on shape optimisation² is proposed to optimise the mould: Generate an envelope of the outer layer according to the demand (maximum stress, strain, deformation requirements, etc.). In another word, the material (or equivalent thickness) distribution over the structured mould is following the need instead of uniform distribution (Fig. 5.2). This process would be helpful for saving material usage while retaining the strength and stiffness.

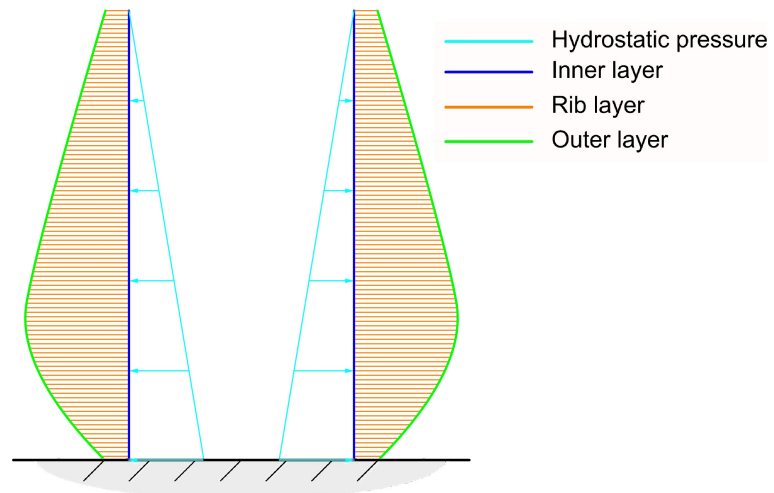


Figure 5.2: Side view of optimised mould.

5.2. Approaches

In order to accomplish the objective of thickness distribution defined in the previous section, three attempts have been made. The optimised thickness distribution is achieved by iterative addition or reduction of the material across the envelope of the mould.

Moreover, as mentioned in Section 2.4, the material tests and numerical modelling were carried out parallel, which resulted in two attempts having been made prior to the material tests. Therefore, they are based on the isotropic material properties. However, it did not influence the decision and selection of the final approach because if it does not work well with the isotropic material, it could not be applied with orthotropic material either.

5.2.1. Modelling with shell elements

The first attempt utilizes shell element. The inner layer discrete into shell elements, and by iteratively increase the thickness of each shell element according to stress or strain information, the optimised envelope can be found.

This approach has very attractive advantages such as fast computational speed and ease of meshing thanks to the utilization of 2D element. However, it also has very obvious drawbacks. First, the thickness of a shell element is achieved by expanding the 2D element in the direction normal to the shell plane as shown in Fig. 5.3. If there is an angle between two adjacent elements, a rigid knot would be generated to transfer the bending moment, which results in lack of information at the knot (Fig. 5.4). This issue can be neglected while using thin shell, but it could cause inaccuracy in case of a thick element. Second, shell element with large thickness itself is also inaccurate with respect to the theory of FEM³ method. Long distance from integration point to node would increase the error during the

²See Chapter 1 for the information of optimisation.

³Abbreviation of Finite Element Modelling.

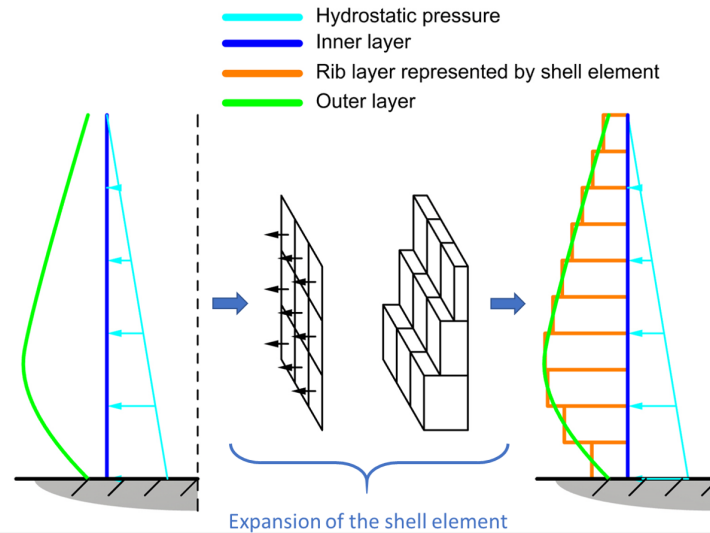


Figure 5.3: Process of envelope generation with shell element (presented with symmetry).

extrapolation. More information on this issue can be found in literature, e.g. [51]. Finally, with the generation of a solid between the inner layer and the outer layer to get the envelope, it is not possible to take the orthotropic behaviour into account, which is essential regarding the material used in this project.

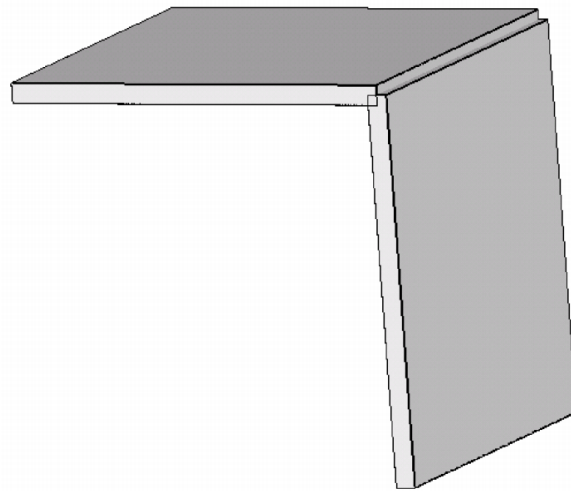


Figure 5.4: Overlapping shell elements at a knot [41].

5.2.2. Modelling with volumetric elements

The second attempt utilizes volumetric element. Different from the first approach, the optimisation direction is reversed. First of all, design domain needs to be defined (e.g. in Fig. 5.5, the design domain is three layer of elements), then the elements which are less important will be removed iteratively according to their stress or strain information and finally yields the desired envelope. This approach was inspired by a well known method for topology optimisation: Bidirectional Evolutionary Structural Optimization. Its introduction and application to additive manufacturing can be found in relevant literature [52].

This approach has better accuracy because it limits the size of volumetric element and consequently

reduces the error during the extrapolation from integration point to node. Moreover, by placing elements at corner, the information (strain, stress, etc.) can be acquired (Fig. 5.6). Although this approach covers almost all the disadvantages of previous method, it is at expense of relatively high computational cost. Volumetric element is naturally more computationally expensive than shell due to the dramatic increase in number of equations to be solved⁴. In addition, it requires even finer mesh to model the envelope precisely, this can be observed in Fig. 5.3 and Fig. 5.5, the model quality with shell is much better than that with volumetric elements. Moreover, orthotropy could not be taken into account either due to the same reason as shell element.

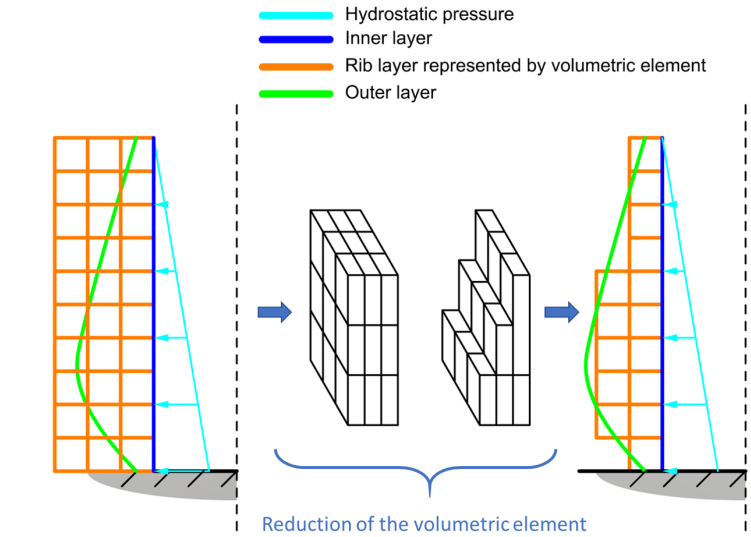


Figure 5.5: Process of envelope generation with volumetric element (presented with symmetry).

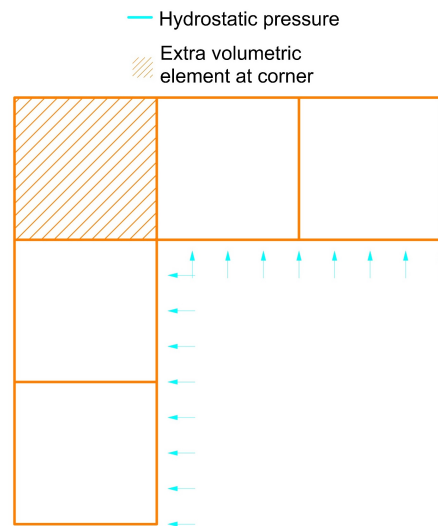


Figure 5.6: Element at corner (Planar view).

5.2.3. Modelling with sandwich element

As mentioned at the beginning of this chapter, the structured geometry of mould can be divided into three parts. A custom composite element is proposed to respectively model these three parts, which

⁴With direct equation solver and first order elements, the computational cost are proportional to d^4 and d^7 for 2D elements and 3D elements respectively, where d is the number of nodes. This problem can be found in literature of FEM, e.g. [51]

consists of two shell elements as the inner and outer layer and a volumetric element as the rib layer (Fig. 5.7). The thickness distribution is transformed into the property distribution of the volumetric elements as a consequence.

This composite element can realistically represent the whole structure with a similar degree of freedom, therefore, more accurate. It also limits the computational cost by controlling the number of volumetric elements. Moreover, thanks to the separation of inner layer, outer layer and ribs, the orthotropic behaviour of each part can be considered. However, it also has a very significant disadvantage: it is difficult to generate the mesh due to the relatively complex element composition. This issue can be reduced with a custom Grasshopper package Guanaco developed by Baran, but not fully solved.

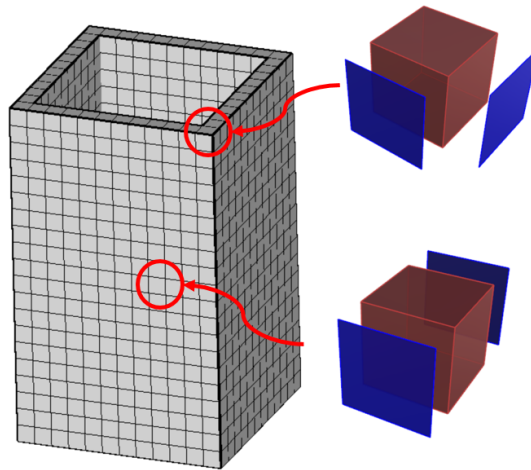


Figure 5.7: Sandwich elements represent a section of formwork for a rectangular column. Blue: shell elements for the inner and outer layer. Red: volumetric element for rib layer.

5.3. Element type

5.3.1. Inner and outer layers

In the previous chapter, a feature of unequal Young's modulus with respect to tensile and bending is described. It causes a nonuniform distribution of Young's modulus across the cross-section as shown in Fig. 5.8, which is high at sides and low in the middle. In order to cover this anisotropy, multilayer shell element was proposed for the modelling [35].

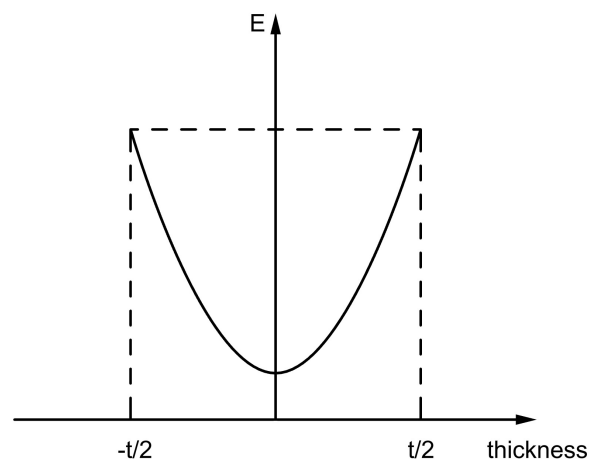


Figure 5.8: Distribution of the Young's modulus across the cross-section of printed wall. Solid: Young's modulus distribution. Dash: profile of cross-section.

Second order quadratic shell element (Fig. 5.9) with reduced integration points is selected for implementation of multilayer shell. This is a commonly used element type for modelling with decent precision, efficiency and robustness, and it prevents issues such as shear locking, over stiff and hour-glass effect with first order 2D elements [41, 53, 54].

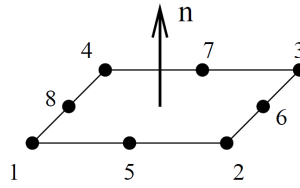


Figure 5.9: Second order quadratic shell element(S8R) utilized in CalculiX [41].

Especially, quadratic shell element is expanded into brick element C3D20R in CalculiX (Fig. 5.10), which has 20 nodes and 8 integration points (Fig. 5.11). The main purpose of this process could be regarded as embracing the effect of shear deformation and normal strain perpendicular to shell element, which are neglected in the definition of thin shell [55]. In case of composite shell element with multiple layers, the element will have $n \times 8$ integration points, where n is the number of layers, and the number of the nodes stays the same as 20. More information can be found in CalculiX manual [41].

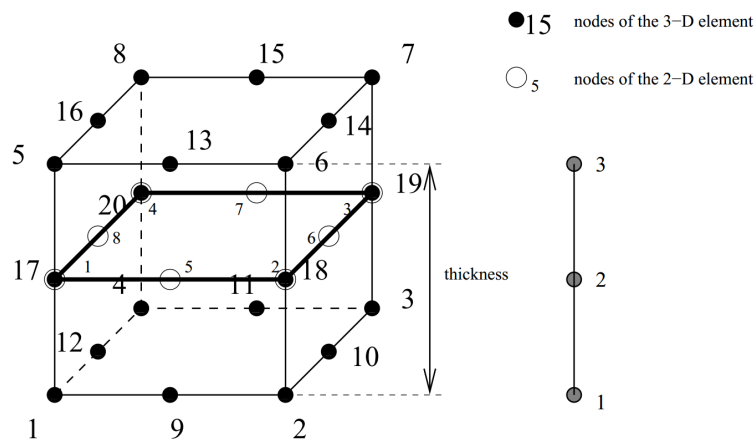


Figure 5.10: Expansion of the S8R shell element. [41]

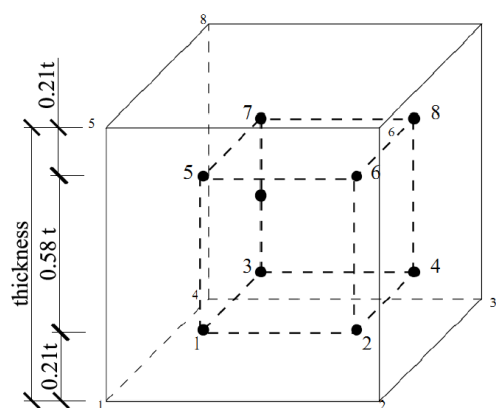


Figure 5.11: Integration points distribution of C3D20R brick element [35].

5.3.2. Rib layer

The volumetric element selected for modelling rib layer is C3D20R brick element, which is same as the element type after expansion from S8R shell element used for modelling inner and outer layer. This simplifies the output from CalculiX thanks to the same element type.

5.4. Analysis mode

Static analysis with geometrical non-linearity option is chosen due to the relatively large deformation accompanied by the structural design with plastic as material. The increment of displacement of each step and the maximum iteration number are set with default values. More information can be found in literature on geometrical non-linearity and documentation of FEM software [41, 50, 54].

5.5. Material Inputs

In this section, the engineering inputs based on the test results for both shell element (inner and outer layer) and volumetric element (rib layer) are presented, including their derivation process and final values. Prior to these, some information needs to be given.

In order to model solid polymers, several material models have been developed [56]. The most popular five types (linear elastic, hyperelastic, linear viscoelastic, plastic, viscoplastic) were compared and discussed by Baran for the applicability in specific case of 3D print moulds [35]. The elastic material model was chosen due to its simplicity, robustness and universality. Despite this model has a potential drawback, which is physical sensibility loss under large strain caused by its linear Hooke's law foundation. This, however, could be treated as not relevant for modelling with shells since the distortions only affects stress values under high compression [35, 41].

Moreover, the problem of lacking the properties normal to the printed wall can be solved by considering the extruded wall as made of unidirectional fibre-reinforced compound, and treating it as transverse isotropic, i.e. in a local coordinate system⁵ its properties in z direction and y direction are identical. Consequently, the stiffness matrix for the determination of orthotropic material will only contain 5 independent elastic constants instead of 9 (Fig. 5.12). These constants defined with local coordinate system are Young's modulus: E_x, E_y . Poisson ratios: ν_{xy}, ν_{yz} and shear modulus: G_{xy} . This approach has been proved to be applicable and reliable by the work of Baran [35], and theoretical derivation can be found in available literature [57].

$$\underline{\underline{C}}^{-1} = \begin{bmatrix} \frac{1}{E_x} & -\frac{\nu_{yx}}{E_y} & -\frac{\nu_{yx}}{E_y} & 0 & 0 & 0 \\ -\frac{\nu_{xy}}{E_x} & \frac{1}{E_y} & -\frac{\nu_{yz}}{E_y} & 0 & 0 & 0 \\ -\frac{\nu_{xy}}{E_x} & -\frac{\nu_{yz}}{E_y} & \frac{1}{E_y} & 0 & 0 & 0 \\ 0 & 0 & 0 & \frac{2(1+\nu_{yz})}{E_y} & 0 & 0 \\ 0 & 0 & 0 & 0 & \frac{1}{G_{xy}} & 0 \\ 0 & 0 & 0 & 0 & 0 & \frac{1}{G_{xy}} \end{bmatrix}$$

Figure 5.12: Inverse stiffness matrix of transverse isotropic material

⁵See Section 2.4 for the definition of the local coordinate system.

5.5.1. Inputs for the shell element

The cross-sectional properties derived from the tests need to be translated to numerical inputs for numerical analysis. First of all, the Young's modulus distribution across the cross-section needs to be investigated. In Fig. 5.8, assuming the function of the Young's modulus distribution curve is:

$$E(x), -\frac{t}{2} \leq x \leq \frac{t}{2} \quad (5.1)$$

Two equations can be established referring to the normal Young's modulus E_{normal} and flexural Young's modulus $E_{flexural}$ derived from the test with nominal thickness t :

$$E_{normal}t = \int_{-\frac{t}{2}}^{\frac{t}{2}} E(x)dx \quad (5.2a)$$

$$\frac{1}{6}E_{flexural}t^3 = \int_{-\frac{t}{2}}^{\frac{t}{2}} E(x)x^2dx \quad (5.2b)$$

With these two equations, $E(x)$ with two unknowns can be solved, and one of them needs to be a constant term. An attempt has been made to apply a simple parabola function and the other high order polynomials:

$$E(x) = Ax^2 + B \quad (5.3a)$$

$$E(x) = Ax^n + B, n \in +\mathbb{Z} \quad (5.3b)$$

where:

A, B are unknowns to be derived.

However, these functions can only be applied to approximate the distribution of Young's moduli if :

$$\frac{E_{flexural}}{E_{normal}} \leq 3 \quad (5.4)$$

In case of the investigated material, $\frac{E_{flexural}}{E_{normal}}$ is larger than three for both single and double layer wall in at least one direction, therefore further research is recommended to have a deeper insight into unequal $E_{flexural}$ and E_{normal} issue and the function to approximate the Young's moduli distribution.

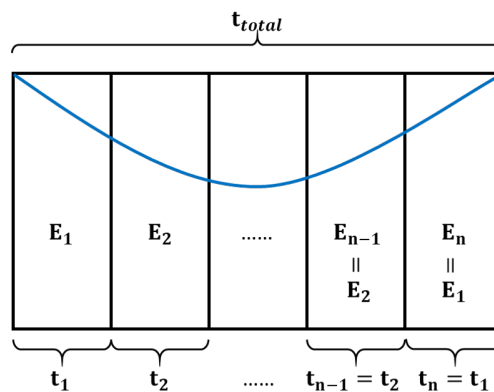


Figure 5.13: Multilayer shell for modelling Young's modulus distribution across the cross-section. Blue: distribution curve of Young's modulus.

Because the function of Young's modulus distribution cannot be determined, it is not possible to use multilayer shell element with more than three layers. For n layer shell (n should be an odd number due

to the symmetry), the number of unknowns need to be solved is $n - 1$, including unknown thickness of each layer and corresponding Young's modulus (Fig. 5.13). However, there are only two equations for solving two unknowns as shown in Eq. (5.2), therefore only three layers shell element is applicable.

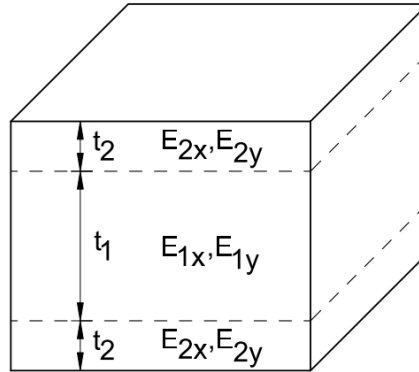


Figure 5.14: Triple-layer shell element[35].

Triple-layer shell element has been used by Baran to model the 3D printed wall made of *Technomelt 3D 6910* (Fig. 5.14). However, this method has the same limitation as in Eq. (5.4) with mathematical proof⁶. Therefore, a modification needs to be carried on in order to reduce the difference between Young's modulus at the side of the printed wall and that at centre. Based on test results shown in Chapter 4, there is a linear relation between load and the response from the structure, i.e. displacement, which means the gradient of the curve (Section 4.2) is a constant and it yields:

Tensile:

$$\frac{E_{normal}A}{L_{eff}b} = \frac{E_{normal}t}{L_{eff}} = C_1 \quad (5.5)$$

Bending:

$$\frac{12E_{flexural}I}{L_{bend}^2b} = \frac{E_{flexural}t^3}{L_{bend}^2} = C_2 \quad (5.6)$$

where:

I is moment of inertia.

C_1, C_2 are constants.

t is nominal thickness.

In which L_{eff} and L_{bend} are constants defined based on test setting, and the remaining terms in the formula, $E_{normal}t$ and $E_{flexural}t^3$, need to be constant as well. This can be presented as:

$$\frac{E_{flexural}}{E_{normal}} \propto \frac{C}{t^2} \quad (5.7)$$

where:

C is constant.

Consequently, by increasing the nominal thickness, the ratio between flexural stiffness and normal stiffness can be reduced and triple-layer shell element can be applied (Fig. 5.15).

⁶See Appendix G for Mathematical limitation of $\frac{E_f}{E_n}$ ratio.

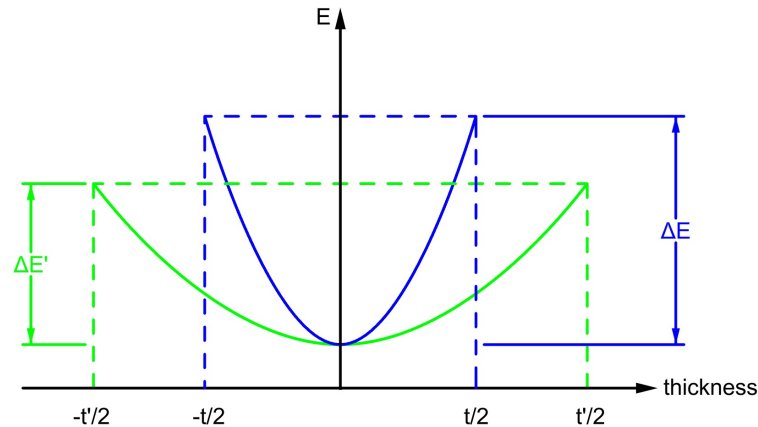


Figure 5.15: Adjustment of Young's modulus distribution by modification of the thickness. Blue: original Young's modulus distribution along the thickness. Green: modified Young's modulus distribution along the thickness.

Additionally, in case of a triple layer element, there are two different layers with different properties, and for each layer the determinant of the compliance matrix must be positive [58]. This means:

$$1 - \nu_{xy}^2 \frac{E_y}{E_x} - \nu_{yz}^2 \frac{E_z}{E_y} - \nu_{xz}^2 \frac{E_x}{E_z} - 2\nu_{xy}\nu_{yz}\nu_{xz} \frac{E_z}{E_x} > 0 \quad (5.8)$$

Combining the requirements defined in equations Eq. (5.4) ad Eq. (5.8), the proposed dimensions and properties of triple layer element are defined as follows⁷:

Single	t [mm]	Total t [mm]	Ex [MPa]	Ey [MPa]	Ez [MPa]	ν _{xy}	ν _{xz}	ν _{yz}	G _{xy} [MPa]	G _{xz} [MPa]	G _{yz} [MPa]
Mid layer	4	8	1538.64	138.60	138.60	0.39	0.39	0.42	67.46	67.46	48.80
Side layer	2		1098.12	351.95	351.95	0.39	0.39	0.42	171.02	171.02	123.92
Double	t [mm]	Total t [mm]	Ex [MPa]	Ey [MPa]	Ez [MPa]	ν _{xy}	ν _{xz}	ν _{yz}	G _{xy} [MPa]	G _{xz} [MPa]	G _{yz} [MPa]
Mid layer	14	16	95.27	135.73	135.73	0.39	0.39	0.42	66.06	66.06	47.79
Side layer	1		1353.63	160.94	160.94	0.39	0.39	0.42	78.32	78.32	56.67

Table 5.1: Numerical inputs for shell element.

⁷See Appendix H for details of calculation of the properties and thickness.

5.5.2. Inputs for the volumetric element

The numerical inputs of the volumetric element, which represents rib layer, depend on its planar pattern (Fig. 5.16). Because of the interaction between mechanical behaviour of the structure and printing path, it is more reasonable to apply pattern with predictable properties instead of random pattern with uncertain printing path.

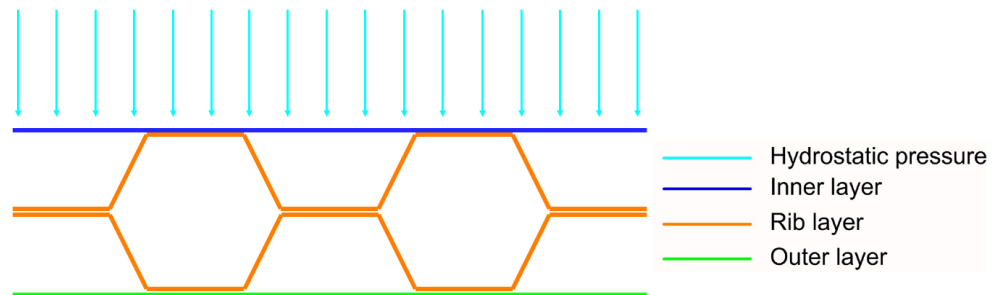


Figure 5.16: Planar geometry of rib layer with regular hexagon .

Two geometries, the regular triangle and the regular hexagon have been considered because of their structural stability. The regular hexagon, so-called honeycomb shape, is a well known in nature for structural efficiency. With the same perimeter (or material usage), it covers 52% more area than regular triangle while retaining the same stiffness (Fig. 5.17).



Figure 5.17: Area coverage of regular triangle and regular hexagon with the same perimeter. If the regular triangle covers an area of A , then the regular hexagon can cover $1.52A$

Moreover, the hexagonal shape provides better printing quality and bonding condition. Similar to the overlap requirement as mentioned in Section 4.3, the print quality of the part with two adjacent members depends on the angle of the printing line, i.e. the smaller the angle the worse the quality. Besides, the bonding length of triangle is also much smaller than that of hexagon.



Figure 5.18: Printing angle and bonding length of triangle and hexagon.

Based on the comparison above, the regular hexagon is selected as the planar pattern for determination of volumetric element properties. There are several pieces of literature for deriving the homogenized in-plane and out-of-plane properties based on honeycomb pattern since it is commonly used in the sandwich slab [59]. The method developed by Shi and Tong [60] is selected due to its simplicity of implementation.

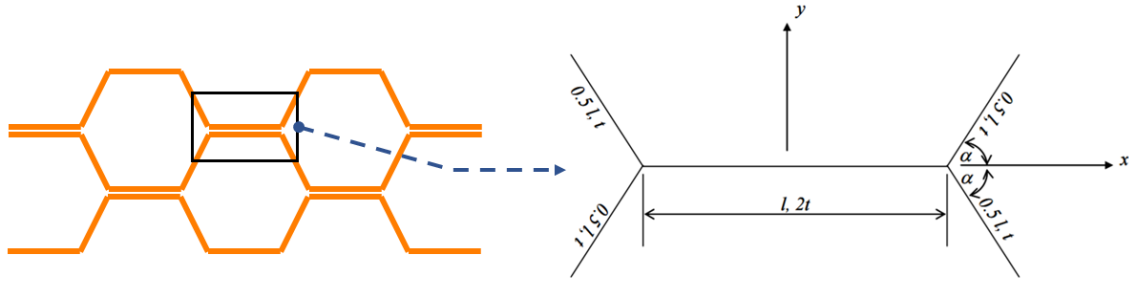


Figure 5.19: Unit cell used for homogenization of honeycomb [59, 60].

According to the method, a unit cell (Fig. 5.19) is selected to represent the hexagon, with which the whole hexagonal honeycomb structure can be constructed by repetitive addition. All the properties used in homogenization are normal properties because the theory assumes no bending at joints. In addition, because of the orthotropic properties of the walls of the unit cell, some terms need to be modified based the formulas by Soliman [59].

$$\begin{aligned}
 E_x = E_y &= \frac{\sqrt{3} t}{5 l} E_{x',normal} \\
 E_z &= V_f E_{y',normal} \\
 G_{xy} &= \sqrt{3} \left(\frac{t}{l}\right)^3 E_{x',normal} \\
 \nu_{xy} = \nu_{yx} &= 1 \\
 \nu_{zy} = \nu_{zx} &= 0 \\
 G_{zx} &= \frac{\sqrt{3} t}{2 l} G_{x'} \\
 G_{zy} &= \frac{t}{\sqrt{3} l} G_{x'}
 \end{aligned} \tag{5.9}$$

where:

x, y, z are x, y and z axis defined for unit cell in Fig. 5.19.

x', y' are x, y axis defined in local coordinate system⁸.

E, G, ν are Young's modulus, shear modulus and Poisson's ratio⁹.

V_f is the volume fraction of homogenized element and hexagonal pattern.

In addition, due to the fact that strength and stiffness properties of a double-layer wall are smaller than single layer wall as mentioned in Section 4.3, a reduction need to be applied based on the area of single layer part and double layer part respectively¹⁰. The final properties will be:

$$P_{final} = \frac{1}{3} P_{single} + \frac{2}{3} P_{double} \tag{5.10}$$

where:

P_{single} is corresponding properties of single-layer printing, e.g. longitudinal Young's modulus.

P_{double} is corresponding properties of double-layer printing.

⁸See Section 2.4 for the definition of local coordinate system.

⁹It should be noted, numerical input of Poisson's ratio should not be 1 or 0, otherwise it will cause error of FEM. Therefore, 0.99 and 0.01 are used to represent them respectively.

¹⁰This is a logical assumption, but it needs to be validated further.

Finally, the homogenization of hexagon pattern with side length¹¹ equal to 100 mm yields properties as shown in Table 5.2:

$E_{x, \text{hex}}$ [MPa]	$E_{y, \text{hex}}$ [MPa]	$E_{z, \text{hex}}$ [MPa]	$\nu_{xy, \text{hex}}$	$\nu_{xz, \text{hex}}$	$\nu_{yz, \text{hex}}$	$G_{xy, \text{hex}}$ [MPa]	$G_{xz, \text{hex}}$ [MPa]	$G_{yz, \text{hex}}$ [MPa]
16.84	16.84	149.73	0.99	0.01	0.01	0.21	29.38	19.59

Table 5.2: Homogenized properties for regular hexagonal shape with side length of 100 mm.

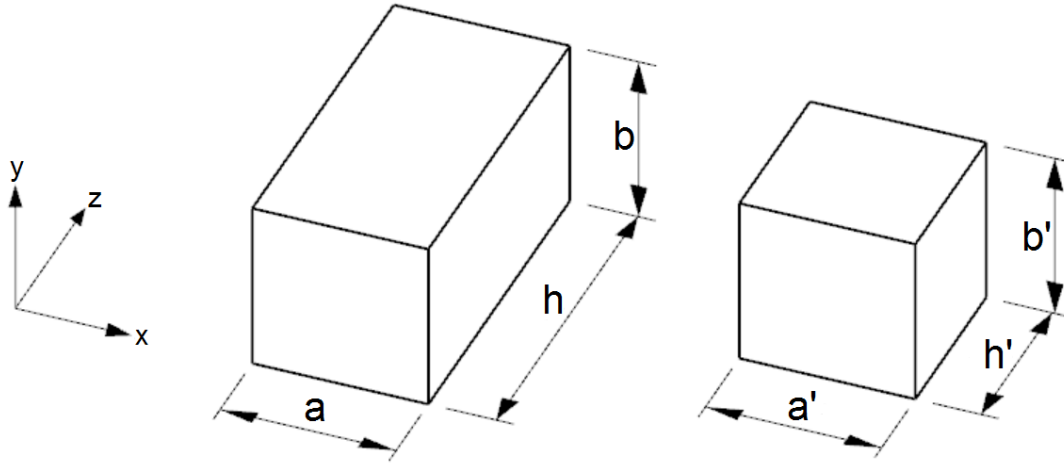


Figure 5.20: Conversion from homogenized properties to the element properties in local coordinate system. Left: real size homogenized element. Right: mesh-size volumetric element.

Once the homogenization is done, it needs to be converted into the properties of the volumetric element¹², i.e. a real-size element with homogenized properties need to be compressed into the element with mesh size, and the properties of the mesh-size element will change accordingly if the dimensions of the real-size element changed. However, because only the distance between the inner and outer layer will change, i.e. $a = a'$, $b = b'$, thus only one dimension h is variable (Fig. 5.20). And the properties of mesh-size element become the values as shown in Table 5.3. In order to simplify the orientation definition, these values have been transformed to local coordinate system defined for shell element instead of the coordinate system used in Fig. 5.19.

$E_{x, \text{mesh}}$ [MPa]	$E_{y, \text{mesh}}$ [MPa]	$E_{z, \text{mesh}}$ [MPa]	$\nu_{xy, \text{mesh}}$	$\nu_{xz, \text{mesh}}$	$\nu_{yz, \text{mesh}}$	$G_{xy, \text{mesh}}$ [MPa]	$G_{xz, \text{mesh}}$ [MPa]	$G_{yz, \text{mesh}}$ [MPa]
16.845η	149.73η	16.845	0.01	0.99	0.01	29.38η	$\frac{0.21(\eta + 1)}{2}$	$\frac{19.59(\eta + 1)}{2}$

Table 5.3: Converted element properties for regular hexagonal shape with side length of 100 mm.

where:

η is equal to $\frac{h}{h'}$ as shown in Fig. 5.20.

¹¹See Appendix I for the definition of the maximum side length of hexagon.

¹²See Appendix J for the conversion from homogenized properties to element properties.

5.6. Numerical validation

In this section, several models are built and presented to validate the proposed method of numerical inputs. The validation was only carried out with numerical modelling because of the relatively large time interval between tests and difficulty with arranging the printer. It is recommended to conduct more experiments with printed structures for the validation.

5.6.1. Material tests validation

The validation of results from material tests was carried out with ANSYS since it is easier to implement with a graphic user interface. The content of validation includes the results of tensile and bending test. The method for validation is applying a displacement according to the data of yield point, and check the corresponding reaction force and the strain in x direction for comparison. The results of shear test were not considered due to the same reason as explained in Section 4.2. Material inputs in Table 5.1 are used for validation. The settings of the model, including dimensions and boundary conditions, are same as that used in the laboratory experiment. Especially for the model for tensile test, the length of testing area is set with the effective length¹³. The coefficient of friction between steel and tested material in bending test is set as 0.3 [61]. See Figs. 5.21 and 5.22 for the details.



Figure 5.21: Numerical model for tensile test [mm]. Blue: clamped. Red: displacement in positive x direction.

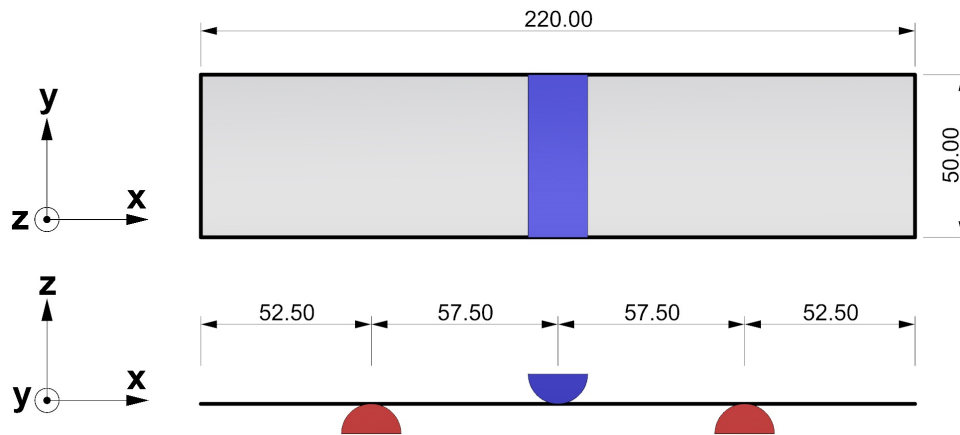


Figure 5.22: Numerical model for tensile test [mm]. Blue: steel head, displacement in negative z direction. Red: steel support, fixed.

The reaction force and strain are calculated according to Eqs. (5.11) and (5.12), and the comparison result are list in Tables 5.4 and 5.5.

For tensile:

$$\varepsilon_{x,normal} = \frac{d}{L_{eff}} \quad (5.11a)$$

$$F_{normal} = \frac{E_{normal} b t d}{L_{eff}} \quad (5.11b)$$

¹³See Appendix E for the definition of effective length.

For bending:

$$\varepsilon_{x,flexural} = \frac{6dt}{L_{bend}} \quad (5.12a)$$

$$F_{flexural} = \frac{4E_{flexural}bt^3d}{L_{bend}^3} \quad (5.12b)$$

where:

d is displacement in tensile and bending respectively. (Figs. 5.21 and 5.22)

L_{eff} is effective length for tensile test which equals to 116.95 mm. (Appendix E).

L_{bend} is support span for bending test which equals to 115 mm.

b is width of specimen. 20 mm for tensile and 50 mm for bending. (Figs. 5.21 and 5.22)

t is modified nominal thickness for single-layer(8 mm) or for double-layer(16 mm). (Table 5.1)

E_{normal} is total normal Young's modulus in two directions. (Table 5.1)

$E_{flexural}$ is total flexural Young's modulus in two directions. (Table 5.1)

Layer	Direction	Displacement [mm]	Indicator name	Experiment result	Model result	Difference[%]
Single	Longitudinal	0.29	Force [N]	522.78	523.65	-0.17
			Strain[%]	0.25	0.27	-8.00
	Transverse	0.41	Force [N]	135.99	137.33	-0.99
			Strain[%]	0.35	0.36	-2.86
Double	Longitudinal	0.44	Force [N]	304.20	305.78	-0.52
			Strain[%]	0.38	0.40	-5.26
	Transverse	0.62	Force [N]	233.98	242.85	-3.79
			Strain[%]	0.53	0.55	-3.77

Table 5.4: Comparison between experimental and model results with respect to tensile property.

Layer	Direction	Displacement [mm]	Indicator name	Experiment result	Model result	Difference[%]
Single	Longitudinal	1.40	Force [N]	108.74	92.09	15.31
			Strain[%]	0.51	0.50	1.96
	Transverse	1.12	Force [N]	24.61	21.35	0.13
			Strain[%]	0.41	0.41	0.00
Double	Longitudinal	1.01	Force [N]	278.78	155.26	44.31
			Strain[%]	0.74	0.56	24.32
	Transverse	0.81	Force [N]	63.09	34.13	45.90
			Strain[%]	0.89	0.42	52.8

Table 5.5: Comparison between experimental and model results with respect to flexural property.

From the comparison results above, it can be seen the results of tensile comparison correlate well, but the results of bending comparison validation deviate significantly especially with double-layer

results. This is caused by the usage of the modified nominal thickness (Table 5.1), which makes the span/thickness ratio less than 20. Consequently, the element becomes thick shell and the influence of shear deformation becomes larger. This is taken into account by applying Mindlin-Reissner shell theory [62] in ANSYS with element type SHELL181 [50]. In CalculiX, as mentioned in the previous section, the calculation of shell element is based on the expanded 3D element (Fig. 5.10), therefore the shear deformation is also taken into account. However, the impact of this deviation is relatively small because the custom defined interpretation of the strain result¹⁴ is based on the thin shell theory.

5.6.2. Single-layer mould

A comparison between ANSYS and CalculiX with respect to a single layer mould is shown in this subsection. By building a mould for rectangular column with dimension of $500\text{mm} \times 500\text{mm} \times 1000\text{mm}$, the maximum total displacement and normal strain (local coordinate system¹⁵) are compared. The boundary conditions are: simply supported at bottom edge and hydrostatic pressure¹⁶ with concrete density of 2400kg/m^3 . The side view of the mould is shown in Fig. 5.23.

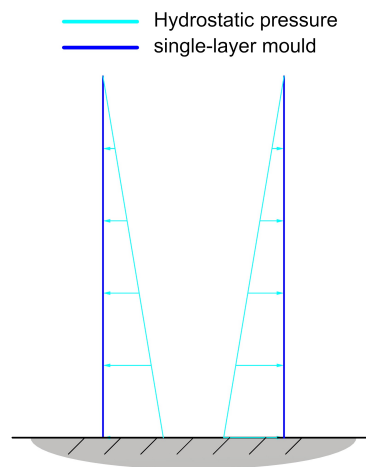


Figure 5.23: Side view of the single-layer mould for casting rectangular column.

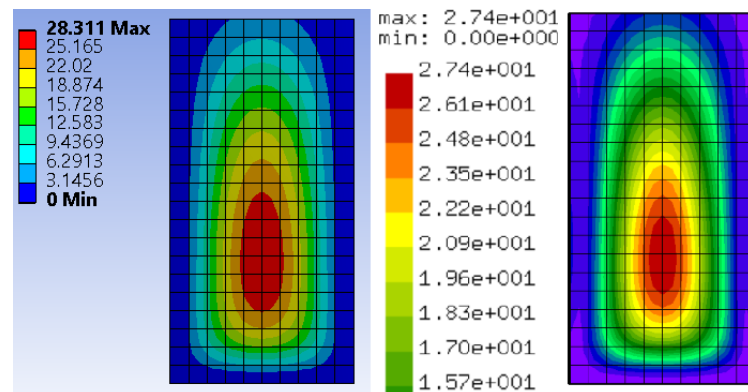


Figure 5.24: Displacement pattern. Left: ANSYS. Right: CalculiX.

The displacement distribution pattern is shown in Fig. 5.24, and the results are listed in Table 5.6. From the results, it can be seen that with different software the results are not completely identical. The maximum total displacement generated by both software products are similar, but the strain results are relatively deviated. This is caused by the different theory behind the calculation as mentioned in the last subsection and can be regarded as not having a large impact due to the same reason of custom

¹⁴See Appendix K for the custom defined interpretation of the strain result.

¹⁵See Section 2.4 for the definition of local coordinate system

¹⁶See Appendix F for the hydrostatic pressure of concrete.

defined strain interpretation. Moreover, in the definition of a shell, strain in the direction normal to the shell element should zero, but both software products generate values as shown in the table because of the their calculation theory.

Software	Maximum total displacement [mm]	ε_x [%]	ε_y [%]	ε_z [%]
ANSYS	28.31	1.80	3.12	1.4
CalculiX	27.40	1.70	2.59	1.7
Difference[%]	3.21	5.56	16.99	-21.43

Table 5.6: Result comparison between ANSYS and CalculiX.

5.6.3. Multilayer hexagon

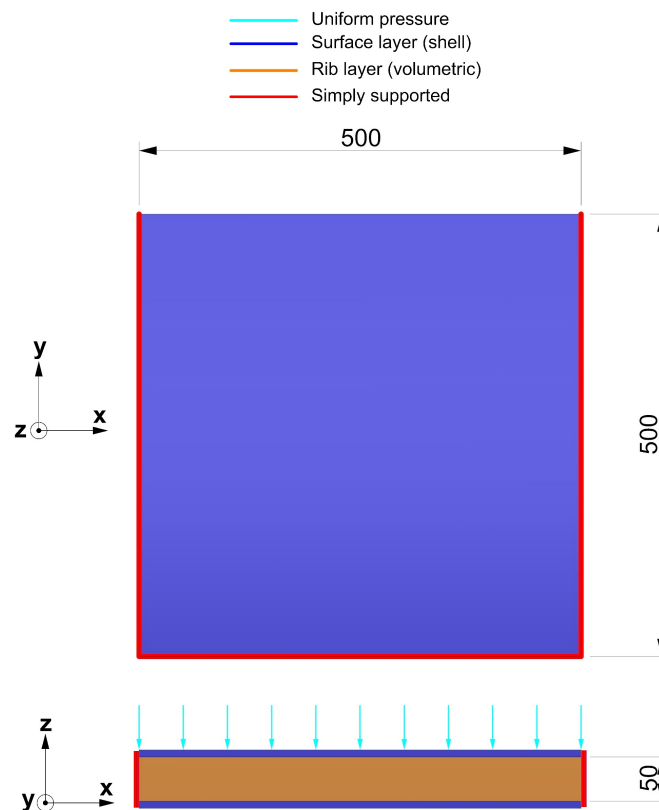


Figure 5.25: Dimensions [mm] and boundary conditions for composite element represented model.

A comparison between rib layer with real structured hexagonal pattern (side length 100 mm) and with the volumetric element was carried out in ANSYS. A section of composite wall including two shell element surface and a volumetric element solid is shown in Fig. 5.25. The uniformly distributed pressure with a value of 0.024MPa is applied on one side of the wall, and three sides are simply supported. The same boundary condition is also applied to real structured wall. Only the maximum total displacement is compared since the strain value generated by the software is less relevant, and the results are shown in Table 5.7.



Layer of hexagon	Real geometry [mm]	Volumetric element [mm]	Difference [%]
0.5 	13.64	13.09	4.00
1 	10.39	11.82	-13.76

Table 5.7: Comparison between real structured model and composite element represented model.

5.6.4. Hexagonal mould

In this section, the structured mould (hexagon side length 100 mm) is designed for casting the concrete column with same dimensions as in Section 5.6.2. Likewise, the bottom edges are simply supported and the concrete density is $2400\text{kg}/\text{m}^3$ (Fig. 5.23). The real structured mould is built in ANSYS and the element represented mould is built in CalculiX (Fig. 5.26). Especially, the model in CalculiX uses symmetry and will be explained in the next chapter (Chapter 6). Only maximum total displacement is presented in Table 5.8.

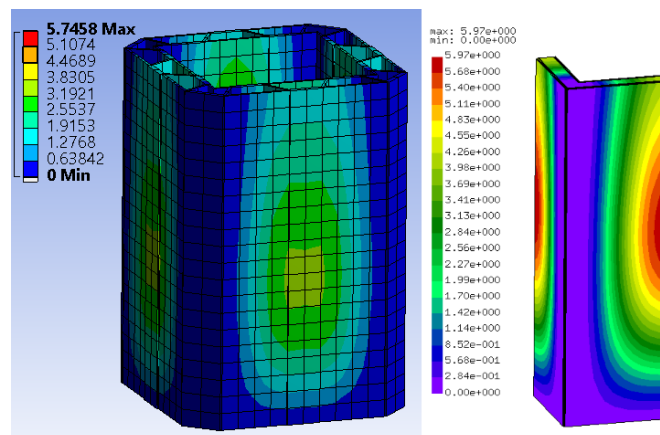


Figure 5.26: Numerical models for structured mould. Left: real structured model in ANSYS. Right: composite element represented model in CalculiX.


Layer of hexagon	Real geometry [mm]	Volumetric element [mm]	Difference [%]
0.5 	5.75	5.97	-3.8%

Table 5.8: Displacement comparison between real structured model built in ANSYS and composite element represented model in CalculiX.

5.7. Summary

The objective of numerical analysis is set to optimise the envelope of the structured mould (Fig. 5.2). A composite element, including two triple-layer shell element and one volumetric element based on hexagonal pattern, is proposed for the modelling, and its numerical inputs can be found in Tables 5.1 and 5.3. Several models are built to validate the established theory: Section 5.6.1 proves the feasibility of the utilization of the triple-layer shell element with modified nominal thickness. Then Section 5.6.2 proves both ANSYS and CalculiX generate similar outputs with respect to a single-layer mould for casting a concrete column. After that, Section 5.6.3 proves the feasibility of the utilization of the custom composite element. Finally, Section 5.6.4 proves that real structured mould built in ANSYS

and composite element represented mould built in CalculiX give similar outputs for casting a concrete column.

6

Design methodology

In the previous chapter, an objective of numerical modelling is described. By taking advantage of 3D printing technology, it is possible to optimise the envelope of the printed moulds following the material or thickness requirement. A custom composite element is proposed, including two shell elements and one volumetric element, with which the material or thickness need is transformed to the material property requirement of a given volumetric element. This chapter proposes an approach for achieving the desired optimised envelope of the moulds by modifying the material property of the volumetric element. The approach is mainly carried out in CalculiX with Python script, and Rhinoceros with grasshopper plug-in takes care of outputs display and model construction of the final shape. The main content of this chapter contains the inputs and algorithm for the iteration process supplied by an example for illustration.

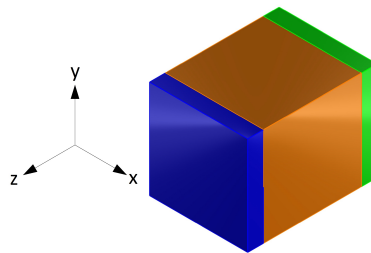


Figure 6.1: One composite element in the local coordinate system. Blue: one shell element as outer layer. Orange: one volumetric element as rib layer. Green: one shell element as inner layer.

6.1. Variables and inputs

Since the objective is to distribute the thickness over the mould, the thickness becomes the main variable in the iteration process. As shown in Table 5.3, once the size of the hexagon and the offset distance between two paired shell elements (or the dimension of the volumetric element in y direction in local coordinate system¹.) have been defined, the only variable becomes the thickness h of the real-size homogenized element. With increasing this thickness, the material properties of the volumetric element can be increased accordingly.

As for the other inputs, an initial thickness needs to be defined to prevent too close distance between two shell elements². Besides, the step, i.e. thickness increase in each iteration, is defined according to the size of the mould.

¹See Section 2.4 for the definition of local coordinate system

²In this project, the minimum distance between two shell elements is considered as 40 mm, which is 5 times the modified nominal thickness of single-layer printing (Table 5.1)

Moreover, two design criteria are defined: strain and maximum total displacement. Only the strain is considered because of the linear relation between the force(or moment) and displacement. The strain results of each element are interpreted with custom definition³, and it needs to be lower than the design value of the yielding strain to fulfil this basic requirement. The definition of the design value of the yielding strain is according to the values of single-layer print in Table 4.6. No criteria is defined regarding double-layer printing, because the weakest point (location which has maximum strain or stress) of the moulds is usually on the inner layer, and its criteria is already taken into account by limiting the size of the hexagon⁴. During this research, no weak point is found at location on the mould other than the inner layer. Criterion of the maximum total displacement is an input, upon which the iteration algorithm will stop. These two design criteria can be interpreted as the formulas below:

$$\varepsilon_{Ed} < \varepsilon_{Rd} \quad (6.1a)$$

$$D_{total,max} < D_{total,criteria} \quad (6.1b)$$

Additionally, an evolutionary ratio is needed for the iteration algorithm. It is introduced separately in the next section. To sum it up, the variable and inputs with units are as follows:

- **Variable**

- Thickness h of the real-size homogenized element [mm]

- **Inputs**

- Offset distance between two shell elements[mm]
- Hexagon side length [mm]
- Initial thickness [mm]
- Iteration step [mm]
- Strain criteria [-]
- Displacement criteria [mm]
- Evolutionary Ratio [-]

6.2. Implementation

The implementation of the thickness distribution contains following steps:

1. Input desired shape and mesh it with Guanaco and Gmsh to generate composite elements.
2. Run Python script, which contains iteration algorithm, to call CalculiX.
3. Using the thickness distribution result from the previous step to construct the mould.

The integrated process of the implementation is shown as a flowchart in Fig. 6.10, including inputs and the iteration algorithm.

6.2.1. Sensitivity analysis

Prior to the iteration algorithm, sensitivity analysis needs to be introduced which is commonly used in topology optimisation [63, 64]. It is used for determining the importance of the elements with respect to different demands, e.g. stiffness, density. Its application with different programming language for topology optimisation can be found in several sources, e.g. [65, 66]. Because the second criteria for the iteration is displacement, the stiffness of the structure is regarded as most relevant. Consequently, the strain energy(Eq. (6.2)) of the shell element is selected as the sensitivity. The strain energy of the volumetric element is not included since the material property of the element is variable. Strain energy

³See Appendix K for the custom defined interpretation of the strain result.

⁴See Appendix I for the definition of the maximum side length of hexagon.

for linearly elastic materials:

$$U = \frac{1}{2}VE\varepsilon^2 \quad (6.2)$$

where:

V is volume.

E is Young's modulus.

ε is strain.

In CalculiX, the strain energy can be automatically generated as output. Once the calculation is finished, the strain energy of the shell elements is collected and sorted in descending order. The element with highest strain energy is regarded as most important, and a threshold is defined as the average value of the highest strain energy and lowest strain energy. After that, by multiplying a predefined evolutionary ratio with the threshold, an adjustable threshold of internal energy can be defined (Fig. 6.2).

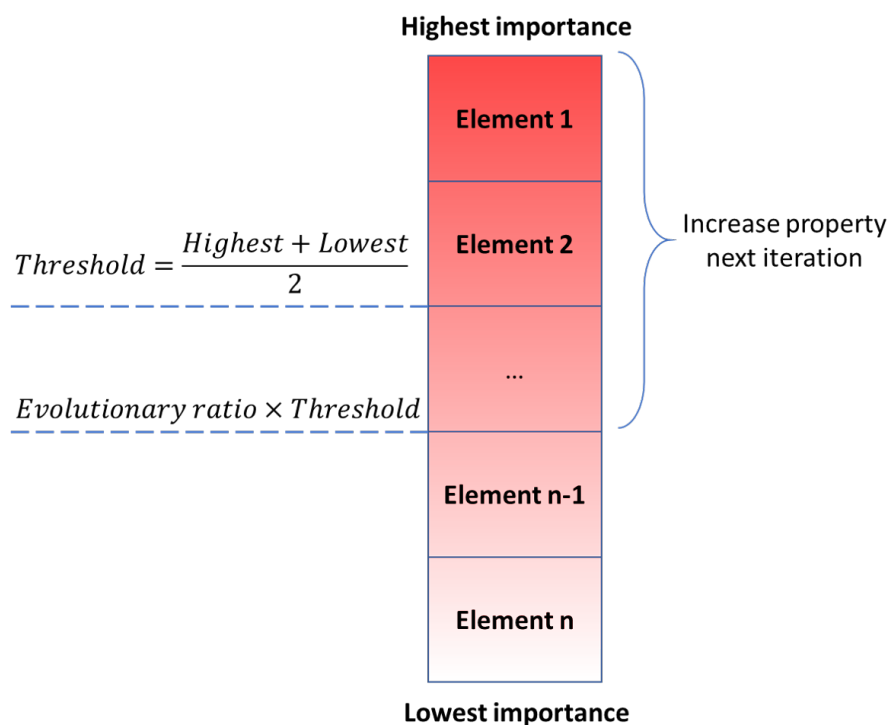


Figure 6.2: Sensitivity analysis for selecting elements to increase property.

6.2.2. Iteration algorithm

The algorithm for distributing the thickness is an iterative process. First, the desired shape is transformed into a mesh of composite elements and relevant general inputs are defined. Then the CalculiX generates outputs, including strain, displacement and internal energy, based on these inputs. After that, if the output results do not fulfil the criteria, the procedure switches to the sensitivity analysis. As shown in Fig. 6.2, if any shell element has internal energy higher than the modified threshold, its corresponding volumetric element will increase its property in the next iteration, i.e. increase the corresponding thickness of the real-size homogenized element⁵. Next, the modified material properties of the volumetric elements will be the new inputs for the calculation of next iteration. Finally, if both criteria are met, the iteration stops, and the outcome is the optimised thickness distribution.

⁵It should be noted, each volumetric element has two corresponding shell elements. If the strain energy of any of them is beyond limit, the property of the volumetric element will increase.

6.3. Example

An example is presented in this section to elaborate the process of the design methodology according to Fig. 6.10. Considering a mould for casting a simple rectangular column which has dimensions of $500\text{mm} \times 500\text{mm} \times 1000\text{mm}$. The mould is simply supported at the bottom, and for the sake of simplification, symmetry is utilized to consider only one quarter of the mould. Consequently, the corresponding edges need to be constrained with the rotational degree of freedom around the vertical edge and translation degree of freedom in the plane of the printed wall and perpendicular to the edge (Fig. 6.3, Left.). The concrete density is 2400kg/m^3 , and the hydrostatic pressure caused by it has a maximum value of 0.024MPa at the bottom of the mould and minimum value of 0MPa at the top (Fig. 6.3, Right.). After the meshing with the composite element, the input mesh for CalculiX has a form as shown in Fig. 6.4.

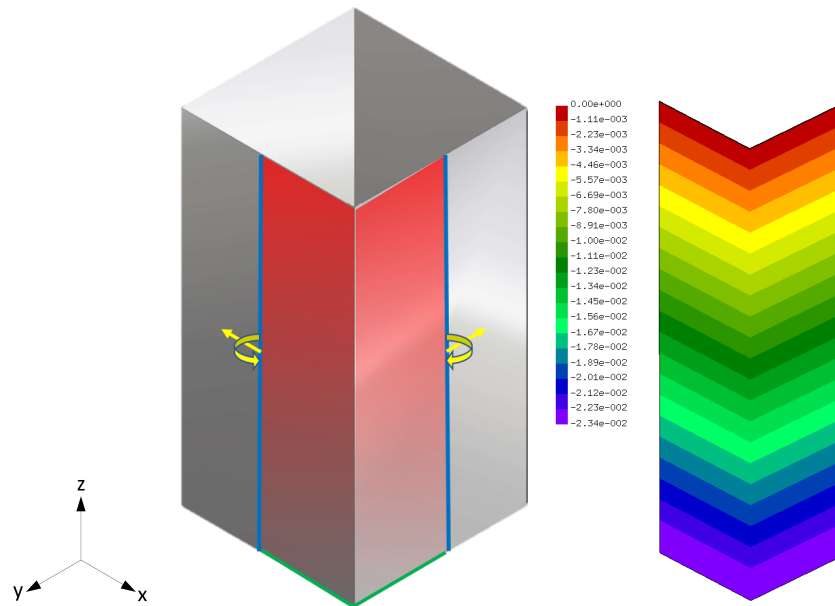


Figure 6.3: Example mould. Left: boundary conditions of one quarter of the mould. Right: hydrostatic pressure.

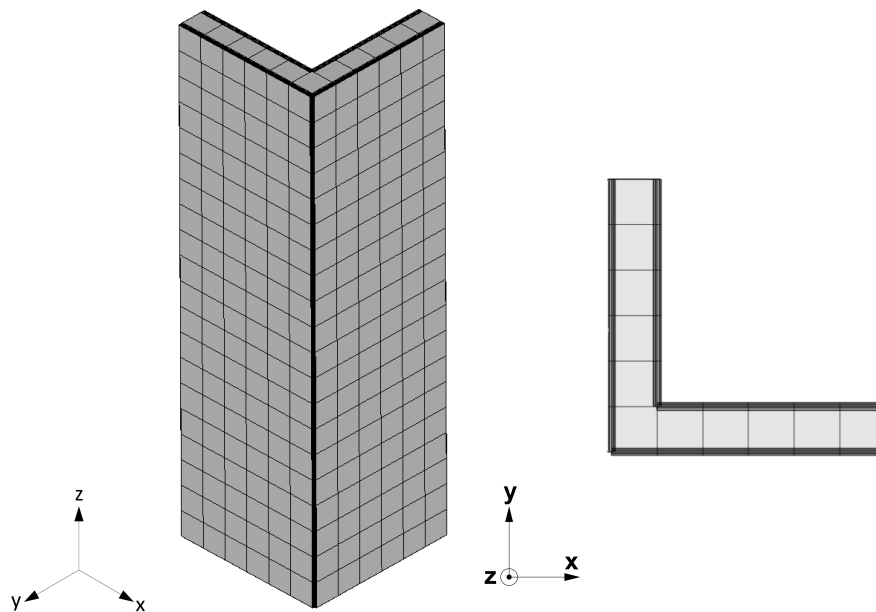


Figure 6.4: Composite element represented mould. Left: meshed mould. Right: planar view shows the composition.

The inputs for the algorithm are as follow:

- **Inputs**
 - Offset distance between two shell elements is 50 [mm]
 - Hexagon side length is 100 [mm]
 - Initial thickness is 85 [mm]
 - Iteration step 10 [mm]
 - Strain criteria is according to Table 4.6
 - Displacement criteria is 5 [mm]
 - Evolutionary Ratio is 4.5

The distribution results are shown in Fig. 6.5 with half of the wall because of symmetry. It can be seen the thickness increases in some elements with the increase of the iteration number while some elements, with blue colour, retains the initial thickness. The iteration stops at 16 round, and generate a thickness distribution pattern as show in the last graph of Fig. 6.5. There are several elements have largest thickness, but it should be noted, the elements at corner and bottom (in the red brackets) have an overestimated thickness due to the singularity. This is a common issue regarding the Finite Element Modelling, and it usually appears at corners with a right angle or at the support. Its influence is relatively obvious with the implemented algorithm in this example because it is related to the property increase of the element, and the higher the property the severer the singularity. Therefore, the final shape should be modified regarding this issue to get the right shape. This issue could be solved with rounded or chamfered edge, but these operations would increase the difficulty of meshing. Furthermore, as shown in Fig. 6.6, with the iteration number increases, both the average strain energy among the elements and its standard variance have a reduction. This means there are more elements contribute to the structure and share the load, which makes the structure more redundant and durable to reduce the impact of accidental local fracture.

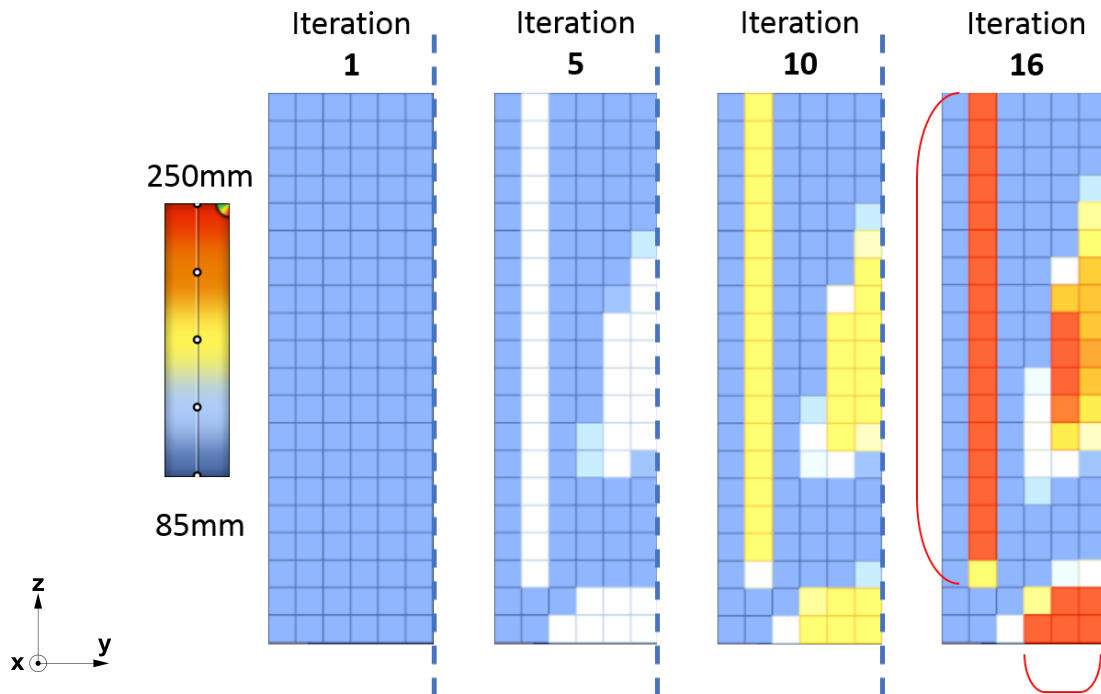


Figure 6.5: Thickness distribution with the iteration.

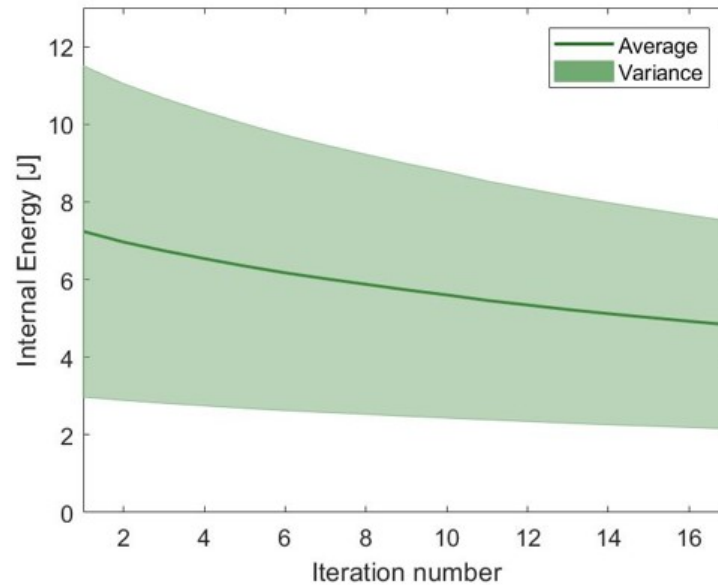


Figure 6.6: Internal energy changes with the iteration.

Once the thickness distribution is known, it can be constructed in Rhinoceros with real hexagons. During the construction, the 45 degree overhang angle limitation regarding the 3D printing technology [67] needs to be taken into account. In case of this research, this limitation is even more strict according to the practical experience of the relatively large size of the printed product. The overhang angle limitation applied is 50 degree, in spite of it is preferred to be 60 degrees for a better printing quality. The hexagons are placed as regular as possible, and the final shape is input to ANSYS for checking. The output displacement does have a more uniform pattern, but the maximum total displacement is 3.22mm instead of the criteria set in the inputs of 5mm . This difference has two potential reasons: First, the shape has been modified due to the overhang angle limitation, and consequently consume more materials than expected and makes the structure stiffer. Second, the utilized homogenization method assumes no bending at joints of the hexagon (Section 5.5.2), but there actually are bending generated at the joint and contributing to the stiffness of the structure.

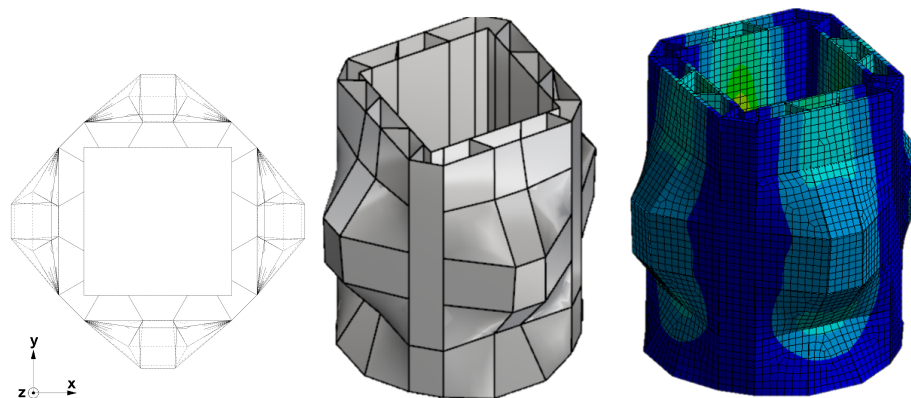


Figure 6.7: Constructed mould for checking. Left: technical planar view. Middle: constructed model in Rhino. Right: displacement distribution pattern of the mould from ANSYS.

What is more, comparing with the theoretical value of the saved material usage (27.36% ⁶), the value from the model is 1.7% . The reasons behind this significant reduction could be: Firstly, the thickness distribution in the constructed model does not follow the output results completely due to

⁶In order to achieve the same criteria of displacement, it requires a uniformly distributed thickness of 139mm , and by comparing it with the result from optimised thickness distribution, 27.36% material has been saved.

the limitation of the overhang angle, which makes the results not the most optimised. Secondly, the meshing size has influence on the quality of the output. However, too fine mesh would increase the computational cost, and the relation between the mesh size and the output quality is not investigated within this project. Thirdly, a feature of the large-scale 3D printing is: it needs to print layer by layer continuously, i.e. the layers of the hexagons at every height needs to be the same. It significantly reduces the benefit from the thickness distribution, since it causes more multilayer printed part in the structure which reduces the stiffness while increasing the material usage⁷ (Fig. 6.8). The final potential reason is also related to the multilayer printing. Since the regular hexagon with a predefined side length is selected as planar pattern, if the thickness of the rib layer needs to be reduced, the length of the double-layer part will increase, and the property drops with the material usage increases (Figs. 6.8 and 6.9).

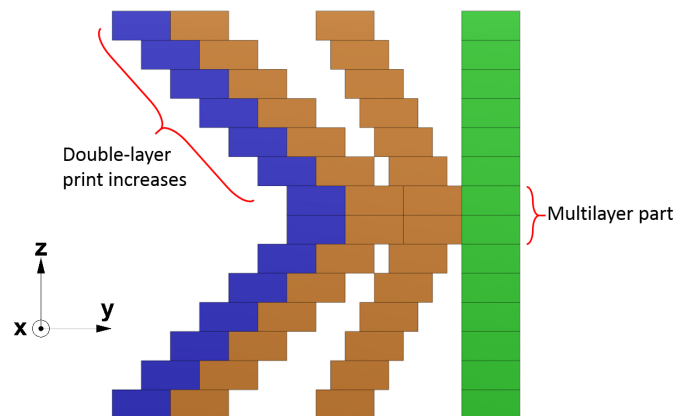


Figure 6.8: Multilayer printing influence on the optimised mould (side view). Blue: cross-section of outer layer printing line. Orange: cross-section of rib layer printing line. Green: cross-section of inner layer printing line.

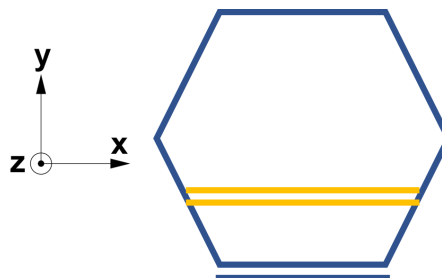


Figure 6.9: Length of double-layer printed part increases with the selected shape in case of smaller thickness of the rib layer (planar view). Blue: regular hexagon pattern. Yellow: longer double-layer printed part.

6.4. Summary

A conceptual design methodology for optimising 3D printed moulds is described in this chapter, including the process and an example. Required inputs for applying the methodology is defined in Section 6.1. The implementation of the algorithm is explained in Section 6.2. And a example is presented with results and several problems in Section 6.3. The integrated process is shown in the flowchart in Fig. 6.10.

⁷See Section 4.3 for the property reduction regarding multilayer printing.

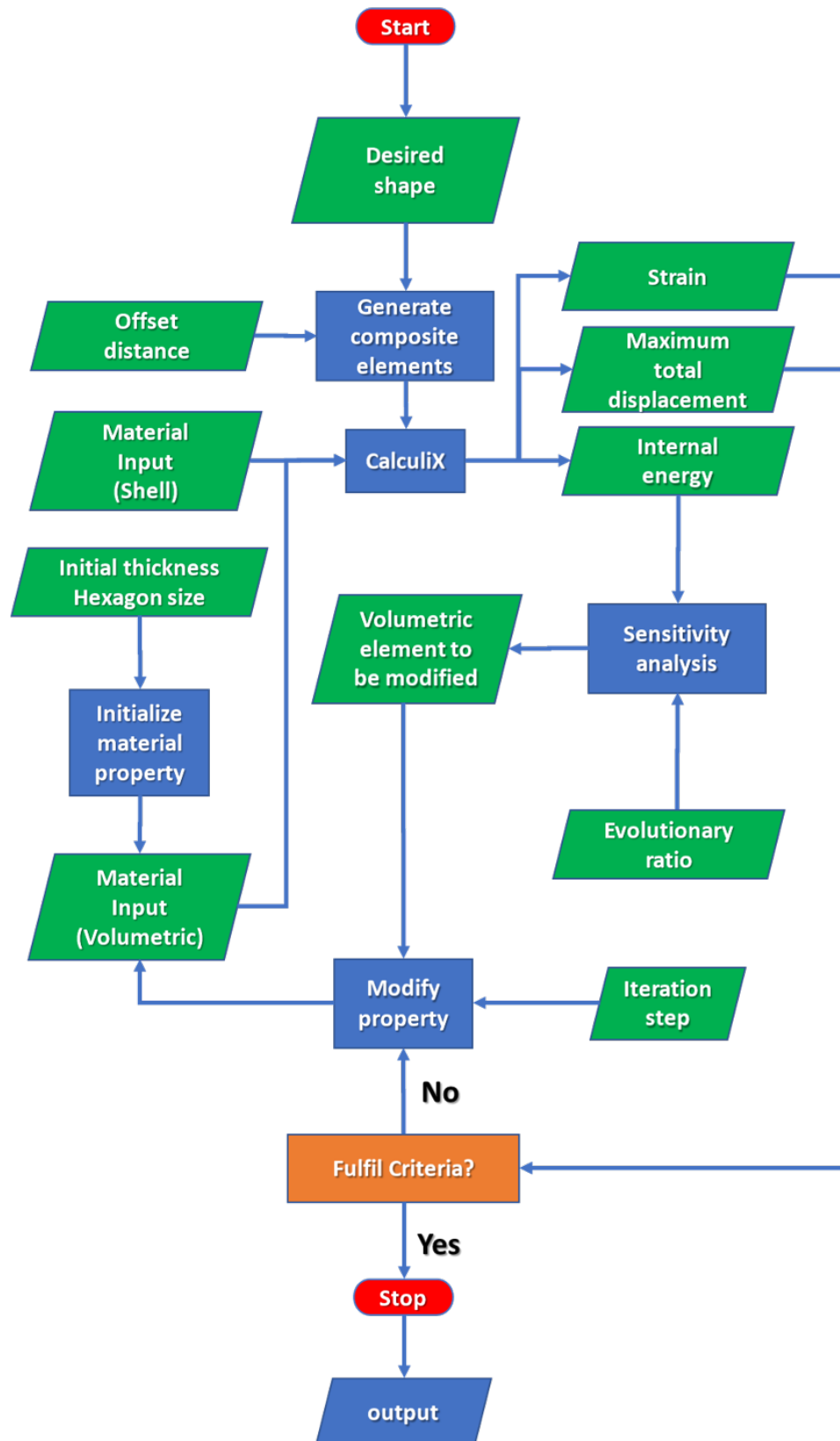


Figure 6.10: Integrated process of the thickness distribution.

7

Case study

In this chapter, a case study is presented, which implements the proposed design methodology. The selected material for design is *Scolefin 53-G-10 natural* with 50% virgin material and 50% recycled material. However, it is too difficult to produce this composition for larger-scale product since it requires print twice, and shredding such a big structured product into small pieces is also challenging. Therefore, virgin *Scolefin 53-G-10 natural* is used for printing the final moulds. Nevertheless, according to the results from the preliminary test (Chapter 3), the stiffness of the compositions based on *Scolefin 53-G-10 natural* have small deviation regarding the recycled material content, and the mechanical behaviour of the mould should be similar regardless the content of recycled material.

7.1. General information

For the sake of not wasting concrete material, the idea of the case study is designing a product which can be used after this project, and a parametric bench is therefore proposed (Fig. 7.1). The bench consists of a seating area with hollow arch underneath and a parametric back. Since the design of the bench is not the main scope of this research, it only shows the potential of the implementation of the proposed methodology, and the structural aspects such as the load-bearing capacity of the bench are neglected. However, in order to make the bench still usable, high strength concrete and plastic fibre reinforcement are used. More detailed dimensions of the bench can be found in Appendix L.

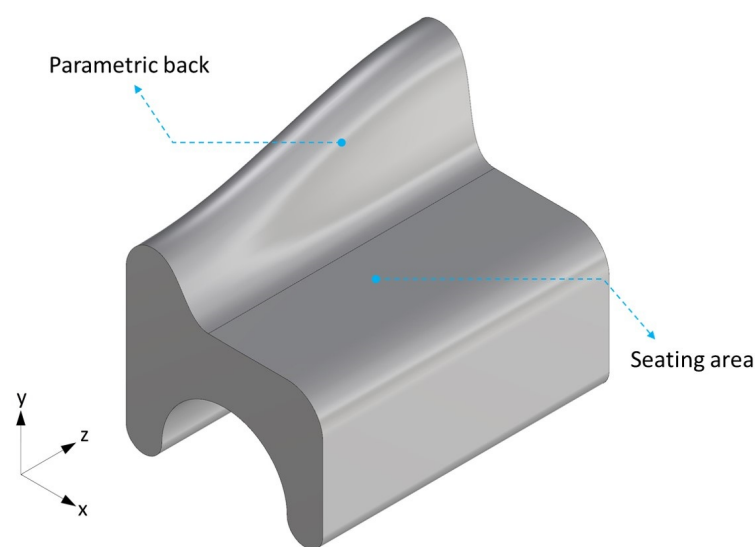


Figure 7.1: Designed bench with seating area and parametric back.

Considering the weight limitation for the transportation and time limitation for the printing¹, the bench is divided into two parts (Fig. 7.2) and the corresponding moulds were printed separately. The casting direction is along the global z axis, and each part has an height of 400mm . The weight of each concrete product is around 150kg assume the density of the concrete is 2400kg/m^3 .

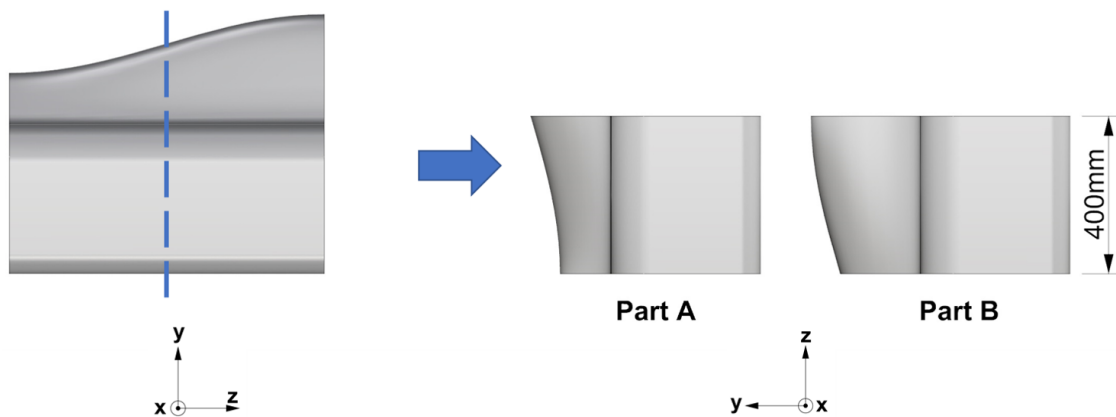


Figure 7.2: Separated two parts of the bench.

7.2. Mould design

Design inputs of the moulds are slightly different according to the specific needs of each part, e.g. maximum total displacement. The strain criteria is according to Table 4.6, and the other inputs are listed in Table 7.1. The detailed design methodology can be found in the previous chapter. Because of the irregular form of the designed parts, only the results of one face, where the maximum displacement appears, are presented (Figs. 7.3 to 7.6).

Input	Part A	Part B
Offset distance [mm]	25	
Hexagon side length [mm]	100	50
Initial thickness [mm]	50	
Iteration step [mm]	5	
Displacement criteria [mm]	2	1.5
Evolutionary Ratio	30	

Table 7.1: Inputs for the thickness distribution methodology for the case study.

During the iteration process for calculating the form of the mould *Part A*, the maximum displacement has been reduced 18%. The theoretical material reduction is 22% and the estimated value is 2.4%. This is caused by the same reason with multilayer printing as explained in Section 6.3. The thickness distribution of *Part A* has a pattern as shown in Fig. 7.3. It can be seen that the pattern follows the distribution of the internal energy in Fig. 7.4. Moreover, with the iteration number increases, the number of the elements with lowest internal energy (purple in Fig. 7.4) becomes less, and more elements have medium internal energy (green in Fig. 7.4). This means more elements are contributing to the structure and consequently increases redundancy. One thing should be noted, the singularity occurs at the support, but it does not affect the result thanks to the adjustment by the setting of evolutionary ratio.

¹The printing time highly depends on the extruding height of the product since it is related to the cooling time, the higher the product the longer the printing time.

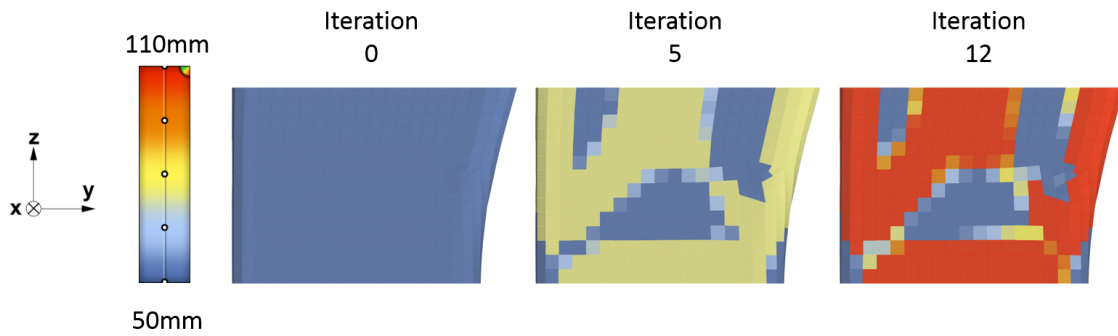


Figure 7.3: Thickness distribution of *Part A* with iteration.

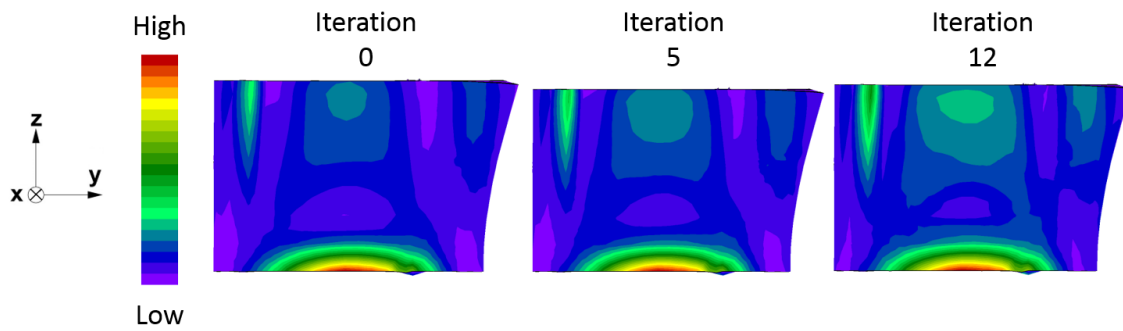


Figure 7.4: Internal energy distribution of *Part A* with iteration.

As for the *Part B*, its maximum displacement has a reduction of 33%. The theoretical and estimated material reduction are 22% and 1% respectively, the reduction of the efficiency of the optimisation is also caused by multilayer printing, and the more complex the shape the more impact on the optimisation results. The thickness distribution with respect to the iteration number is shown in Fig. 7.5 and internal energy distribution is shown in Fig. 7.6. It can be seen that the overall internal energy of *Part B* is lower than *Part A*, i.e. more elements are in green, this is because of the utilization of smaller size of regular hexagon for designing *Part B*. More uniformly distributed strain energy with the increase of the iteration number and singularity issue can also be observed in Fig. 7.6.

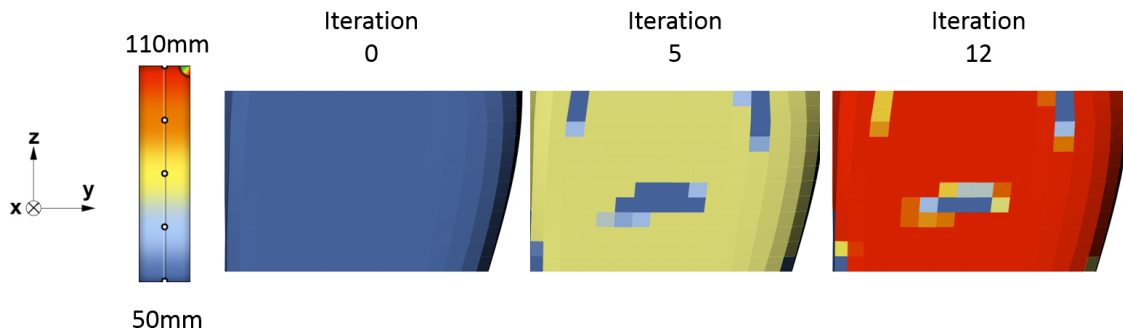


Figure 7.5: Thickness distribution of *Part B* with iteration.

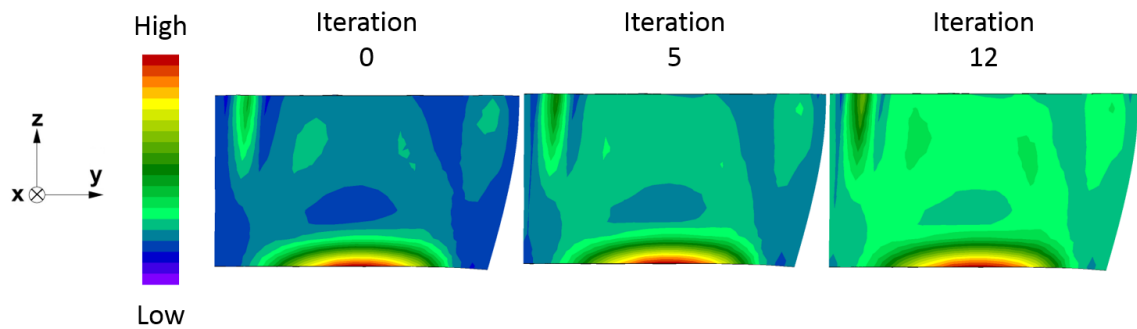


Figure 7.6: Internal energy distribution of *Part B* with iteration.

7.3. Post-processing

Different from the example presented in Section 6.3, the post-processing for the case study includes a further step to transform the structured model into the input shape for the 3D printer. First of all, the original shape needs to be represented by the contour curves along z axis, and the curves need to be offsetted by 4mm , including 1mm overlap for sufficient bonding. Next, the offsetted contour curves are trimmed and reconnected (Fig. 7.7).

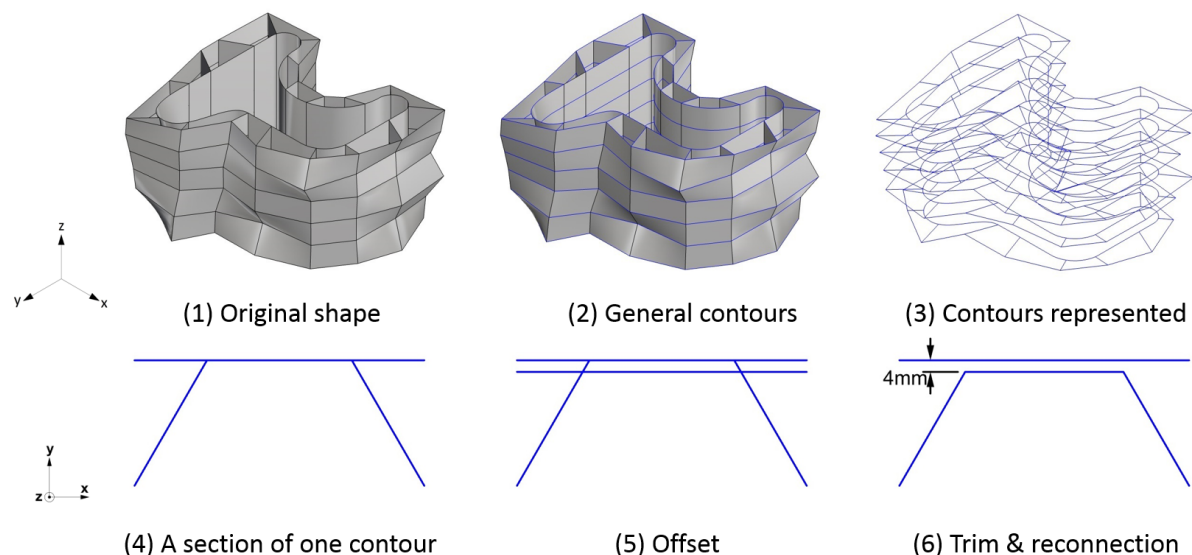


Figure 7.7: Example of contour generation of *Part A*.

Moreover, because of the layer-by-layer printing feature, seams are required to make the planar curve continued, and the start point (also is the end point) of the curve at each height level needs to be the same. In order to ensure the sufficient bonding and printing quality at the seam, the printing path has also been considered, which has aligned connections instead of staggered (Fig. 7.8). After finishing printing the first layer, the nozzle of the printer shift to the next layer (Fig. 7.9). The final shape for printing is shown in Fig. 7.10.

The post-processing is currently manually and contains inaccuracy, e.g. offsetting generates triple-layer printing parts. Besides, the influence of the seam is not taken into account. However, the post-processing is an important step, especially it includes the generation of the printing path, which is one of the crucial factors that influence the mechanical behaviour of the final structure. Therefore, a more accurate, integrated, efficient and controllable post-processing methodology is desired for the further development.

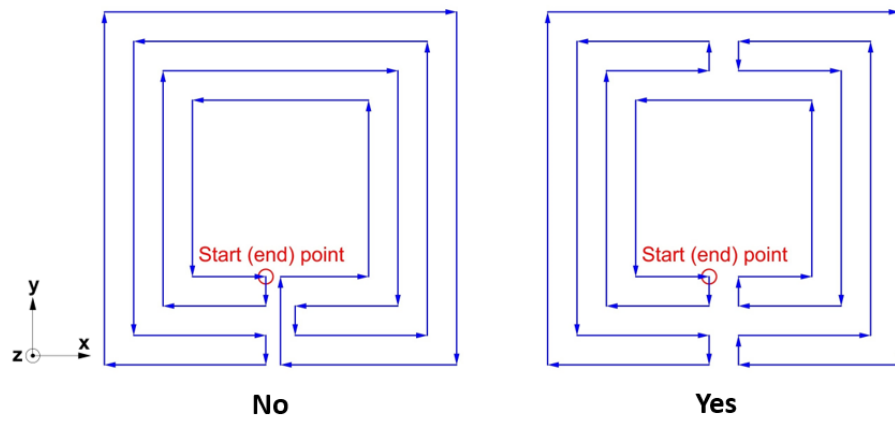


Figure 7.8: Example of printing path at each level. Left: staggered. Right: aligned.

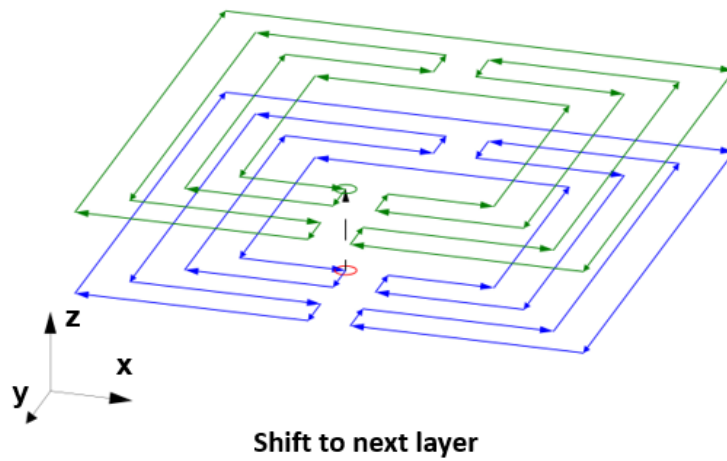


Figure 7.9: Example of shifting to the next layer.

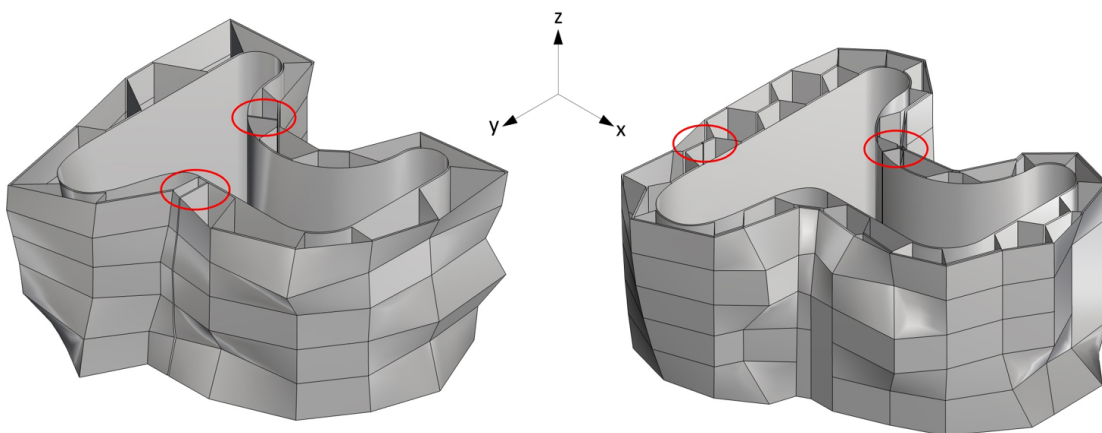


Figure 7.10: Final shape as input for the 3D printer. Red circle: location of the seam.

7.4. Practical implementation

The printing of two moulds was scheduled between 29th January 2018 and 9th February 2018, and was actually finished on 2nd February. *Part A* and *Part B* have printing time of 7 hours and 8.5 hours respectively. After 14 days for sufficient curing, they were delivered to *Macrolab at faculty Civil Engineering and Geosciences, Delft University of Technology*, and conducted the concrete casting. The casting is under the supervision of M. van Leeuwen, and was scheduled on 23rd February 2018. In addition to the moulds for the bench, three moulds for producing the standard concrete cube for concrete strength test with dimension of 150mm × 150mm × 150mm were also prepared (Fig. 7.11).

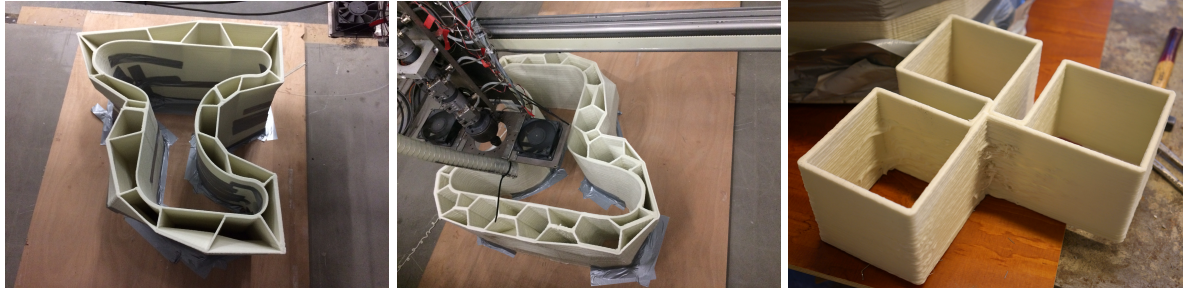


Figure 7.11: Printed moulds for concrete casting. Left: Part A. Mid: Part B. Right: Three standard size cubes.

7.4.1. Preparation

Several measures were carried out for the preparation of the casting. First of all, the staples at the bottom of the printed mould (Fig. 7.12) were removed with electrical saw. The purpose of applying the staple is to prevent the slippage of the product during the printing process, but it would cause the uneven bottom of the moulds for casting. This issue can be improved by reverse the extruding direction to make the side which contains staple upward.



Figure 7.12: Staples at the bottom of the moulds.

Next, the bottom of the outer layer and inner layer were sealed with clay and silicon respectively to prevent water leakage and provide constraint (Fig. 7.13).



Figure 7.13: Bottom sealing. Left: clay at outside. Right: Silicon at inside.

At last, the locations where have cracks were filled with filler. The filler requires 24 hours for sufficient hardening (Fig. 7.14).



Figure 7.14: Filling the cracks. Left: surface of the mould after fixing the cracks. Right: the filler.

The final prepared moulds are shown in Fig. 7.15.

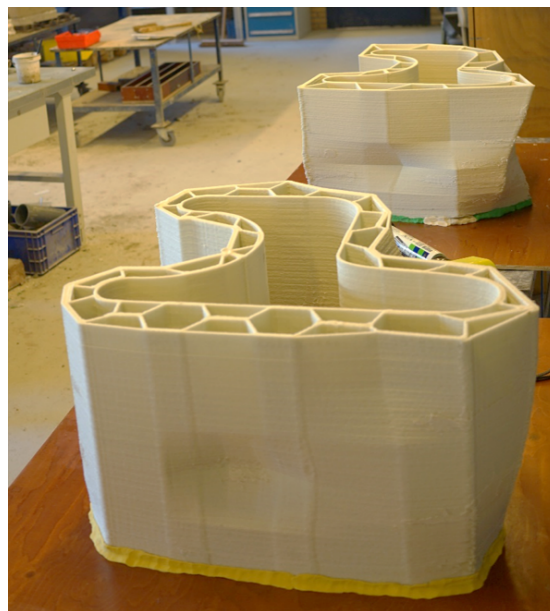


Figure 7.15: Two moulds ready for the casting.

7.4.2. Concrete casting

Thanks to the sufficient preparation, the casting was carried out successfully and efficiently. The concrete has a volume of 160 litres in total, including two main moulds for the parametric bench and three cubes. as mentioned previously, the moulds have severe cracks, and the usage of the vibration needle, therefore, needs to be limited. However, due to the same reason of cracks, the moisture content of the concrete should not be too high in order to prevent leakage. Therefore, semi self-compact concrete was used which embraced and balanced these two considerations. Moreover, because the design of the concrete bench itself is not the main task within this research, its strength is not verified with calculations. To make the final product usable, the concrete mixture for the casting has a relatively high class and should gain the strength around 65MPa after 28 days. In the meantime, plastic fibres were also added to increase the tensile behaviour of the final concrete product. Partial process of the casting is presented in Figs. 7.16 and 7.17, and the details of the concrete mixture can be found in Appendix M.



Figure 7.16: Preparation for the casting. Left: ingredients for the concrete mixture. Right: blender which has a maximum volume of 200 litres.



Figure 7.17: Casting process. Left: cast three cubes. Right: cast the mould.

7.5. Summary and issues

The final concrete products have decent quality, only limited deformations and leakages at the support were observed (Fig. 7.18). The boundary condition was predefined as simply supported in the numerical designing, and this needs to be improved by applying more realistic boundary conditions or by making the support in practical implementation as close as possible to the predefinition. What is more, the demoulding is a very challenging task and requires considerable man labour and time. Therefore, the improvement of demoulding is highly recommended for the further research. The strength test of the concrete cubes were carried out after this project due to the time limitation, thus is not presented in this report.



Figure 7.18: Final concrete product cast by the mould *Part A*.

Within the case study, the most obvious issue is cracking. In order to fix the cracks, extra labour

and cost were spent. One of the potential cause is that the printed geometry contains parts which are double-curved. The double-curved surface weakens the bonding between the printed layers, and consequently caused cracks (Fig. 7.19).



Figure 7.19: Double-curved part on the moulds where has cracks.

The other cause is the shrinkage during the printing process. As mentioned before, *Scolexin 53-G-10 natural* has a severe shrinkage problem, and it also has impact on the structured printed products. The extruding process requires a closed printing path at each height level, and therefore would produce a closed area inside and an open area outside. The heat generated during the printing process could not easily be extracted inside the printing product, while it is easier outside the printing product thanks to the better airflow condition. Although both inside and outside of the printed product have shrinkage, the inner area would shrink more because of the longer duration under high temperature. This uneven shrinkage caused a thermal bending moment that is similar to timber structures (Fig. 7.20), and it makes larger cracks on the outside surface than that on the inside surface as a consequence (Fig. 7.21).

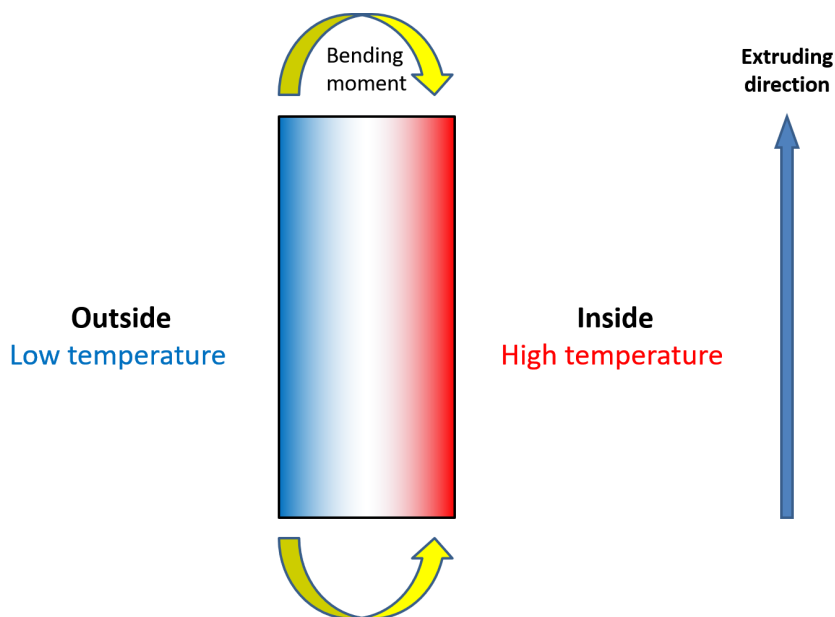


Figure 7.20: Bending moment caused by the uneven shrinkage.



Figure 7.21: Cracks caused by shrinkage. Left: large crack at outer surface. Right: Warping of the bottom of the mould.

To sum it up, the case study is generally successful. The designed moulds are castable and the final concrete products have good quality. However, no measurement was carried out for validating the accuracy of the proposed design methodology with the selected material, thus further application requires more validations. Moreover, the impact of the shrinkage is considerable, more investigation of the material and printing process should be carried out with respect to this issue.

8

Discussion

In this chapter, the overall research project presented in this report is discussed and evaluated, including the tests, implementation, limitations and possible solutions. Regarding the different scope, it can be divided into three parts: Laboratory experiments and mechanical properties, numerical analysis and practical implementation.

8.1. Laboratory experiments and material properties

8.1.1. Overview

A large number of experimental data was collected from the laboratory tests, and according to the deviation of the data and the setting of the test, most of it is reliable and adequate as the input for numerical analysis. The testing frame itself is feasible and relatively precise for deriving basic mechanical properties, except for the shear test. The method seems to be applicable while testing the shear property along the printing direction but becomes messy while testing the transverse direction. The test results for both directions could not provide enough information besides the maximum shear strength. Although shear failure is not dominant within the scope of this project, it is still important for determination of the mechanical behaviour and structural feasibility of a material. Especially the shear behaviour at the interface between the adjacent printed wall in case of multilayer printing, which could have impact with respect to printed geometry. Therefore, this part has relatively large room to be improved.

As for the preparation of the samples, laser cutting is not applicable to the materials which have high content of glass fibre. Even if it could be applied, it is still not suggested to use this method because of the high thermosensitivity of the plastics and potential interference with the test results. Since any physical cutting method is not suitable for the material containing glass fibre, water jet seems to be the only choice. However, it requires flat printed sheet for cutting and is relatively expensive. Improvement of the printing quality would be helpful for cutting with water jet, but it is recommendable to explore the alternative approaches which have less influence on the material property and are economic at the same time.

8.1.2. Recycling

Reuse of the recycled material is promising because of many benefits it brings, such as sustainability and economic. However, its implementation is usually not straightforward due to the foreseeable reduction of mechanical properties after recycling. With respect to the materials investigated in this project, *Scolefin 53-G-10 natural*, *Technomelt 3D 6910* and *60%LDPE+40%PPgf*, the attempt made to reduce the property degradation is mixing recycled material with virgin material. This approach is generally successful. In case of the first material *Scolefin 53-G-10 natural*, although the maximum strength of blends with different virgin/recycled ratio is different, it does not affect the stiffness. In addition, the force-displacement relation of longitudinal tensile property of this material is bilinear. Only the first linear segment is taken into account for design purpose, and the phenomenon is not investigated further. As for *Technomelt 3D 6910*, its strength and stiffness maintains relatively well with all

four predefined mixing ratios. Nevertheless, it is sensitive to creep and consequently requires reduced properties for structural design under long-term load. The third material *60%LDPE+40%PPgf*, is considered not suitable for structural purpose. Both of its strength and stiffness are relatively poor once the recycled material is added in, and it also has relatively significant inhomogeneity. It is justifiable since its 'virgin material' is already post-industrial recycled plastic, and it is the only one coming from the real-life production among the three investigated materials. This should be pointed out because the recycling is usually accompanied with impurities from where the material was used, and it is an important factor which needs to be taken into account as it influences the mechanical behaviour of the material. Therefore, despite *60%LDPE+40%PPgf* is not considered for structural use within this project, it could be still promising in case of using other approaches to reduce the mechanical property degradation and inhomogeneity after recycling. Once the relationship between the real-life recycled source and structural design is established, the benefit would be considerable.

Additionally, a trend is observed regarding the test results. For all three materials, the mechanical property has a tendency to decrease when adding more recycled material to the mixture. However, once the virgin/recycled ratio reaches 25%/75%, the mechanical properties of the composition would rise. This phenomenon is not investigated deeper since it does not lie within the defined research scope, but it could be a point for the further research. However, utilization of the recycled material for structural design should not be considered as using as much recycled material as possible. Reliability, feasibility and applicability are more important.

In terms of the recycling round test for *Technomelt 3D 6910*, the strength retains well even in the 3rd round. However, except for the first round product, it is not suggested to use it for structural design without additives because of the poor printing quality and inhomogeneity.

8.1.3. Material properties

The other mechanical property tests for *Scoflexin 53-G-10 natural* with virgin/recycled ratio of 50%/50% were performed with adequate number of samples. Besides the test results derived from it, the most significant observation is the shrinkage of the material during the printing. The material is based on polypropylene, and a severe shrinkage can be observed on the printed product. This issue has an impact on almost every phase within this project, and none of them is considered as positive. Firstly, it affected the execution of the test. The shrinkage causes warping of the printed product and consequently caused the problem in both cutting and testing stage. Especially in the tensile and shear test, specimen usually broke during the clamping because of the warped surface, and therefore extra effort needed to be made for saving the samples. Secondly, it has relatively large impact on the mechanical properties. Both the unidentical normal and flexural Young's modulus issue and the property reduction of multilayer printing (Section 4.3) is somehow related to the shrinkage problem. And because of the negative impact on the mechanical properties, it significantly reduces the benefit of the optimisation in the modelling stage. Finally, shrinkage affects the quality and usability of the printed product. Cracks can be observed on both test specimens and the printed moulds. Especially for the moulds, although the complex geometry contributes a lot to retain the shape of the mould, the occurrence of the cracks indicates the potential residual stress within it, and the influence of it could be relatively considerable with respect to the safety and usability. Due to the time limitation, the in-depth investigation regarding shrinkage is not carried out. However, attempts are already being made to embrace this issue by adding additives, but its effect still needs to be verified with experiments.

8.2. Numerical analysis

In order to build the numerical model for designing structured moulds, a composite element, including two shell elements and one volumetric element, is proposed (Chapter 5). It is numerically proven to be applicable and relatively accurate, but there is still room for the improvement in several aspects. Firstly, the utilization of the triple-layer shell element based on the modification of the nominal thickness (Section 5.5) because of the large difference between $E_{flexural}$ and E_{normal} . This is a theoretically feasible solution, but it does not reflect the real mechanical behaviour of the printed product. Besides, using larger thickness also affects the implementation and accuracy of the Finite Element Analysis. Therefore, more effort should be put to explore the physical reasons behind this phenomenon, especially the Young's modulus distribution across the cross section. Secondly, thanks to the work of Shi and

Tong[60], it is possible to transform hexagonal pattern into homogenized properties. However, the method itself only considers the pattern as truss and only includes axial force which causes inaccuracy during the transformation. Besides, since it is a method usually applied to composite slabs, that normally do not have a large dimension normal to the slab plane, it could not be fully reliable for the moulds. This could be improved with more theories, e.g.[68, 69]. However, it is more recommended to perform laboratory and experiments on real-structured geometry with hexagonal pattern to investigate the mechanical properties of specific build-up. Moreover, the homogenization of the other patterns is also a promising direction to be explored to expand the applicability of the methodology. What is more, the properties in the transverse direction in terms of double-layer printing is based on the deduction of other results, thus these need to be validated by carrying experiments.

In terms of the algorithm used in the design methodology, it is applicable and adjustable. With different criteria and parameters, it can be utilized for different objectives. There are two main points which would help to improve the efficiency of the algorithm: First, it currently only add materials where needed, but it is possible to make it bi-directional, i.e. also reduce material where it does not need, to produce more optimised outcome. Therefore, literature such as [52] could help to improve this aspect. Second, the convergence speed is currently quite slow in order to achieve the criteria. Using mathematical convergence tools, e.g.[70], could have significant improvement on convergence speed.

As for the outcome of the design methodology, it is relatively limited and conceptual. The final amount of the saved material has a relatively small magnitude. Compared to the preparation needed to be done to implement this methodology, its benefit seems to be negligible. However, most of the negative influence comes from external reasons rather than the methodology itself. Firstly, the 3D printing technology is limited by the 45-degree overhang angle rule, and it is not included in the algorithm but manually modified after the generation of the output. Once it is taken into account during the iteration process, the output is likely to be more reasonable. Secondly, although the selected regular hexagonal pattern is well known for material efficiency, it seems to be less effective in case of the investigated research scope and in some cases it even generates negative impact (Section 6.3). Choosing alternative pattern could be one of the solutions, and with it, the output could be even more optimised with a secondary approach, e.g. with the triangular pattern the flexibility is increased and method such as graphic statics[71] can be utilized to carry out a further structural optimisation. Finally, mechanical properties reduction in case of multilayer printing has a relatively large negative impact, which is the main factor decreasing the efficiency of the optimisation. For the chosen scope, only double-layer printing was investigated (Chapter 4). Its contribution to the material consumption is doubled compared to the single-layer, but its contribution to mechanical property reduction is more than double. This means the occurrence of the double-layer parts would have negative impact on both material consumption and stiffness. If this effect of triple-layer printing is taken into account, the optimised output could even have a negative value. A possible solution could be improving the material composition to reduce the effect of multilayer printing. However, this is difficult to carry out because of the variety of additives and compositions of plastics. Therefore, the relatively reasonable way is to reduce the multi-layer parts of the printed product. It should be emphasized, double-layer parts also contribute to the integrity of the structure by providing sufficient bonding, thus it should not be completely removed but limited.

8.3. Practical implementation

The practical implementation of the design methodology is promising since it takes advantage of the flexibility of 3D printing technology. However, the methodology only constrains the overall quality of the concrete product, i.e. displacement during the casting with the moulds, and local deformation is not taken into account. Therefore, the possibility of combining the proposed methodology and pre-deformation method[35], is another promising direction to achieve a better product quality.

However, there are many work need to be done prior to the utilization of both the methodology and test results, such as thoroughly exploring the material and improvement on the printing technology itself. What is more, the composition of the material, the input printing parameters, even the environmental variables would have a significant influence on the material property, and it is too difficult to control all these variables. Once the parameters have been changed, the applicability of the derived

test results become uncertain, and repetitive material tests need to be performed to verify the mechanical properties. This testing process is time-consuming and only yield basic properties for engineering use instead of the exploration of the physical causes. Therefore, establishing of the related standard is suggested to distinguish different categories with respect to different variables - this would benefit the further development of the technology.

As for the recycling, its resource is a problem needs to be considered. Since the large-scale 3D printing has not become a big industry yet, it is not easy to collect enough materials for the implementation, and the utilization of the real-life resource is accompanied with uncertain influences on the mechanical property. However, this problem is predictable to become less with the development of the technology.

The final aspect regarding the implementation is the printing technology itself. Several limitations, such as printing time, have significant impacts on the applicability of the technology and consequently influence the methodologies based on it. Although it still needs time for development, the situation is getting better.

9

Conclusions

In this chapter, several conclusions are drawn based on the discussion and issues discovered during the research. Same as the discussion chapter, the content is divided into three parts: Laboratory experiments and mechanical properties, numerical analysis and practical implementation.

9.1. Laboratory experiments and material properties

The material tests are presented in Chapters 3 and 4, and it has been discussed in Section 8.1. From the implementation of the testing scheme (Section 8.1.1), investigation of the feasibility of the utilization of recycle plastics (Section 8.1.2) and the material properties derived from the test (Section 8.1.3), it can be concluded that:

- The testing scheme used in the research is applicable and could yield adequate results. However the shear test still needs to be improved.
- Mixing virgin and recycled material can retain the feasibility of the recycled plastics for structural design with respect to large-scale 3D printing technology.
- Recycled plastics without additives or reinforcement are not suitable for structural use from both mechanical and printing quality point of view.
- Besides the significant orthotropic behaviour, the mechanical properties of the printed material are also related to the number of printed layers. Multilayer printing reduces the stiffness.
- Shrinkage of the plastic material has significant impact on the mechanical behaviour, therefore should always be considered during the structural design.

9.2. Numerical analysis

The numerical analysis and the design methodology are presented in Chapters 5 and 6, and based on the discussion of them (Section 8.2), including the discovered issues, utilized iteration algorithm and the outcome of the design methodology, it can be concluded that:

- Modification of the nominal thickness is applicable for numerical analysis if $E_{flexural}$ is larger than three times of E_{normal} .
- The proposed composite element is numerically proven to be applicable and relatively accurate for modelling structured moulds with predefined regular hexagonal pattern.
- The planar pattern (or printing path) has large influence on the mechanical behaviour of the 3D printed mould. This influence is mainly related to the multilayer printing.
- The proposed design methodology is generally applicable. However, its post-processing needs to be developed further.
- The benefit from the optimisation for the 3D printed mould highly depends on the properties and features of the material.

9.3. Practical implementation

The practical implementation aspect has been discussed in Section 8.3. The conclusions are drawn based on the observations and facts during the performance of the material tests and design methodology:

- Large-scale 3D printing technology can be taken advantage of its flexibility. However, the benefit depends on the state-of-art of the technology.
- The source of recycled plastics should be distinguished since it has an impact on the mechanical properties.
- The selected material based on *Scofelin 53-G-10 natural* needs to be mixed with additives to prevent negative impact related to shrinkage issue on both quality and usability of the printed mould.
- Further development of both test scheme and design methodology need to be based on extra numerical and experimental validation.

10

Recommendations

Recommendations presented in this chapter are based on the content of investigated and relevant problems found within this project. Same as the previous chapter, it is separated into three parts: Laboratory experiments and mechanical properties, numerical analysis and practical implementation.

10.1. Laboratory experiments and material properties

The testing scheme for deriving the basic properties is mature. However, as mentioned in Chapter 8, the testing method for the shear property is insufficient. Although shear is not dominant in the research projects done so far, it would have considerable impact in case of complex printed geometry. Especially the shear at the interface of multilayer printing, has a direct influence on the mechanical properties of the printed structure. Besides, mechanical property reduction of the double-layer printing and shrinkage of the material have significant negative impacts on the investigated content, thus are also recommended as investigation directions. Moreover, distribution of Young's modulus across the cross-section of the printed member is currently not clear. Both investigation of physical causes of it and possible improvement are recommended.

As for the recycling of plastics, mixing virgin and recycled materials is a feasible solution for retaining the mechanical properties after recycling. Even though, there are plenty of other approaches in order to retain the properties of the recycled plastics, which could be more suitable and efficient for 3D printing purpose. Moreover, the phenomenon of increased strength with 75% recycled material and 25% virgin material mixture would also be an interesting aspect to investigate.

To conclude the recommendation above, it can be listed as follows:

- Improvement of the method for testing the shear properties.
- Investigation of the mechanical properties, especially shear behaviour, at the interface of adjacent layers in case of multilayer printing.
- Investigation of the physical causes of the large difference between $E_{flexural}$ and E_{normal} and corresponding Young's modulus distribution across the cross-section of the printed member.
- Exploration of the solutions for reducing of the shrinkage of the material after printing.
- Investigation of other approaches to reduce the property degradation of plastic after recycling, especially for 3D printing purpose.
- Investigation of the reason for the strength increase when the material consists of 75% recycled material and 25% virgin material.

10.2. Numerical analysis

There is a large room for improvement with respect to numerical analysis. First of all, the input material properties for modelling the rib layer is based on the theory of homogenization of hexagonal shape for composite slab [69], and the corresponding limitation of the theory becomes the limitation of this project, e.g. only the axial force within the printed member is considered. It is recommended to improve this part by applying more suitable homogenization approaches or using numerical simulation and experiments to establish a specific theory. Then for the design methodology, it is recommended to improve the efficiency and speed of the algorithm such as application of mathematical convergence tools. In terms of the selected planar pattern, regular hexagon, its mechanical performance reduction related to the multilayer printing is significant. Therefore, triangular shape would be an alternative solution because of more flexibility. However, the integrity of the structure needs to be taken care of in case of the utilization of triangular pattern, i.e. sufficient strength at connections between printed members. This part is relatively complex because it is related to the material properties, determination of the printing path and homogenization transformation, thus it should be treated as a crucial part of the further research project. Moreover, the transformation from the optimised thickness distribution to the real structure is currently manual and labour costly, solutions need to be explored to make the methodology applicable. What is more, the methodology proposed in this research project is conceptual and only as one direction for taking advantage of 3D printing technology, thus exploration of the other possibilities is always desirable.

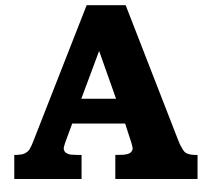
To conclude the recommendation above, it can be listed as follows:

- Rib pattern improvement with respect to both homogenization approach and pattern selection.
- Improvement of the efficiency and accuracy of the iteration algorithm.
- Development of suitable methodology for transforming the thickness distribution to real structure.
- Improvement of meshing method for generating composite element.
- Exploration of the other solutions for optimising the 3D printed moulds.

10.3. Practical implementation

Optimisation is usually not an easy task since it is accompanied by high computational cost and lacking practicality. The improvement of the foundation, e.g. material, on which the optimisation is based should always be developed first. Moreover, the possible combination between the thickness distribution methodology proposed in this project and pre-deformation method [35] would be a promising direction to get more benefit. Moreover, demoulding is a challenging part in case of 3D printed mould, especially for complex geometry. Because the mould is printed in one go, it is relatively difficult to remove, practical solution is therefore recommended. Recommendations, including the points above, with respect to practical implementation are listed below:

- Validation of the applicability and practicality of the proposed methodology without optimisation step.
- Combination of the thickness distribution and pre-deformation methodologies.
- Investigation of the possible improvement of the 3D printing technology, especially the printing speed.
- Establishment of the possible relation between consumer waste recycled plastics and 3D printing technology.
- Solution for demoulding of 3D printed mould.



Material Information of *Scolefin*
53-G-10 natural



■ Scolefin® 53 G 10-0

Polypropylene
Prime Compound

Description:

PPH, 30% glass filled, chemically coupled, heat stabilized, natural

General

MFI (230°/2,16kg)	ISO 1133	15	g/10min
Density	ISO 1183	1.12	g/cm ³

Thermal

HDT/A (1,82MPa)	ISO 75A	145	°C
-----------------	---------	-----	----

Mechanical

Charpy notched impact strength (23 °C)	ISO 179/1eA	8	kJ/m ²
Charpy unnotched impact strength (23 °C)	ISO 179/1eU	40	kJ/m ²
Tensile stress at yield	ISO 527	90	MPa
Tensile modulus	ISO 527	6800	MPa

Various

Ash content (700 °C)	ISO 3451	30	%
----------------------	----------	----	---

Datasheet

The data and information contained herein are typical average values, based on our current level of knowledge and experience, and do not constitute sales specifications. No liability, warranty or guarantee of product performance is created by this document. It is the buyer's responsibility to inspect and test our products in order to determine the suitability for the buyer's application.

Ravago Group Headquarters

Moerenstraat 85A
B - 2370 Arendonk

Tel: +32 (0)14 67 25 11
Fax: +32 (0)14 67 20 12

www.ravago.com
manufacturing@ravago.com

Issue Date:
Jul 2014

B

Calculation of the characteristic
value for material properties

The test results were processed in accordance with NEN-EN 1990 [39]. First of all, the standard deviation of the object samples is calculated according to Eq. (B.1):

$$s = \sqrt{\frac{1}{N-1} \sum_{i=1}^N (x_i - \bar{x})^2} \quad (\text{B.1})$$

where:

N is ample length.

\bar{x} is mean value of x .

Then the coefficient of variance can be calculated according to Eq. (B.2):

$$CV = \frac{s}{\bar{x}} \quad (\text{B.2})$$

Next, the characteristic value of a material property X_k can be derived from Eq. (B.3):

$$X_k = \bar{x}\{1 - k_n CV\} \quad (\text{B.3})$$

where:

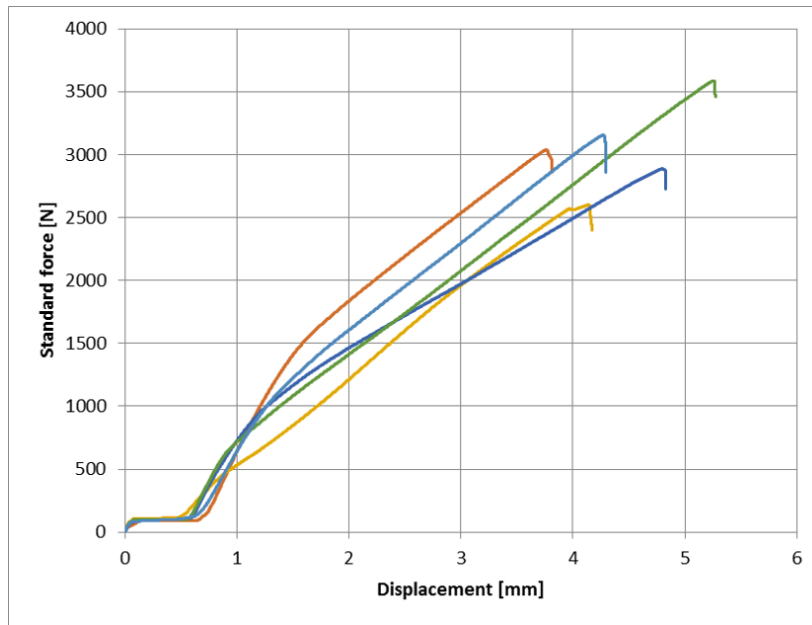
k_n is according to the definition in table E-1 in NEN-EN 1990 [39] and has value as in Table B.1 .

N	1	2	3	4	5	6	8	10	20	30	∞
k_n	2.31	2.01	1.89	1.83	1.80	1.77	1.74	1.72	1.68	1.67	1.64

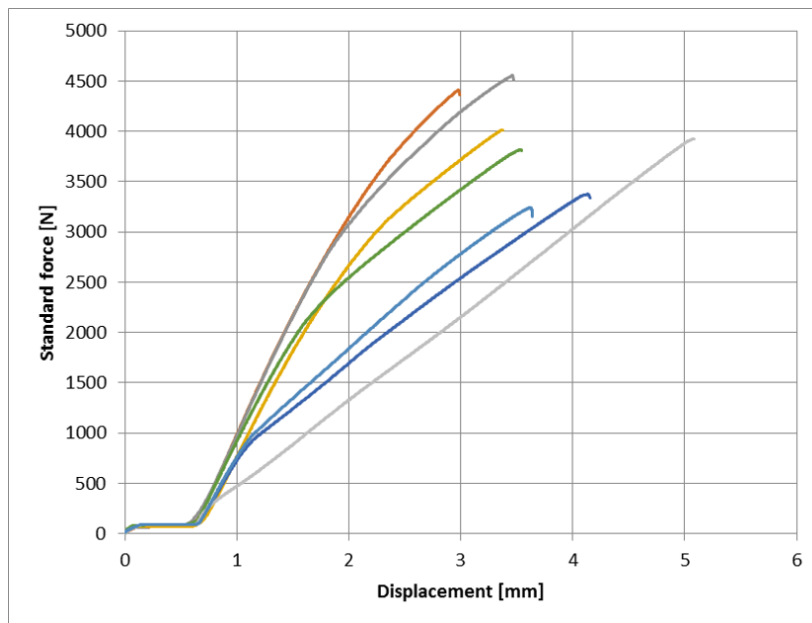
Table B.1: Value of k_n based on the different sample size.

C

Raw data of preliminary tensile test

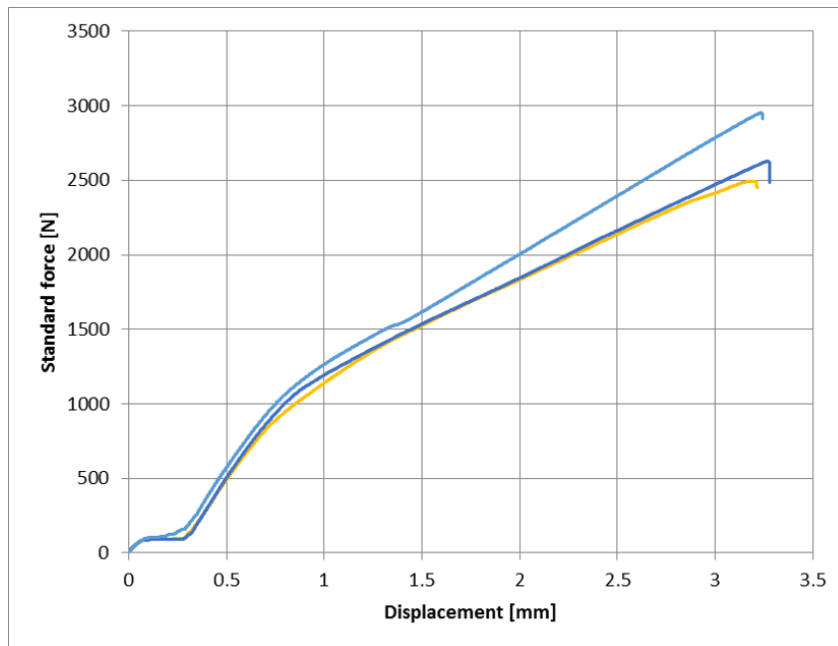
C.1. Composition test results: *Scolefin 53-G-10 natural*

(a) Test speed 0.5 mm/min.

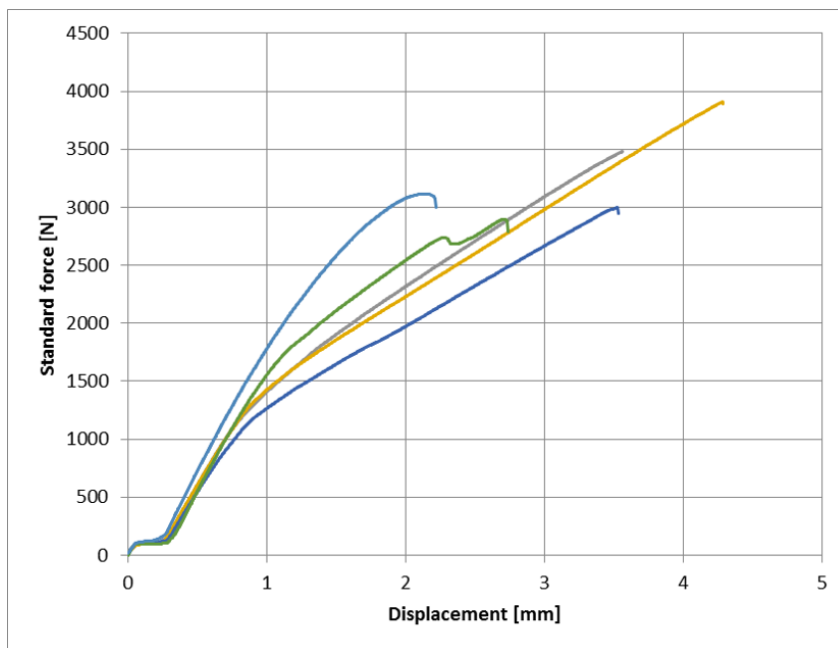


(b) Test speed 10 mm/min.

Figure C.1: Force-displacement curve for virgin/recycled material composition 100%/0%.

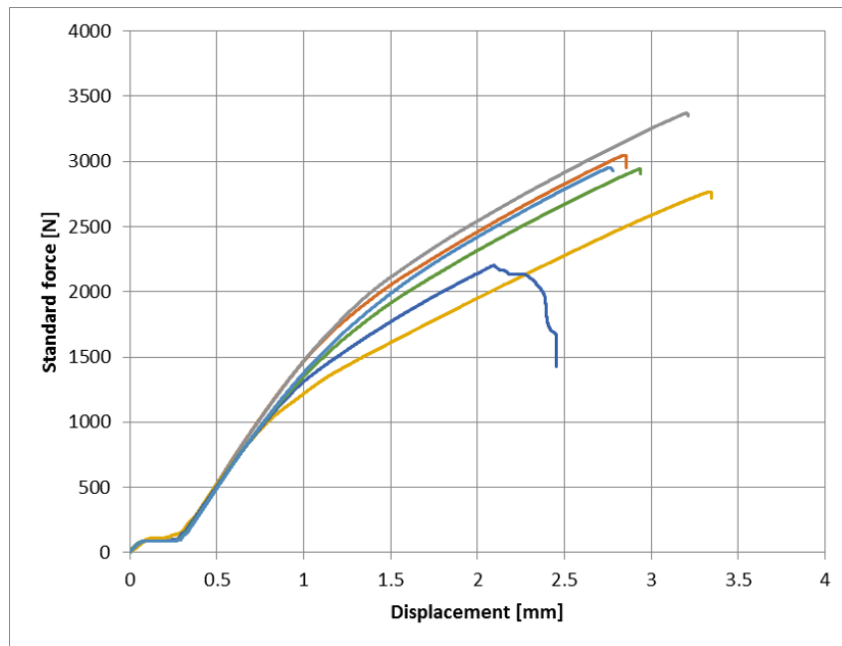


(a) Test speed 0.5 mm/min.

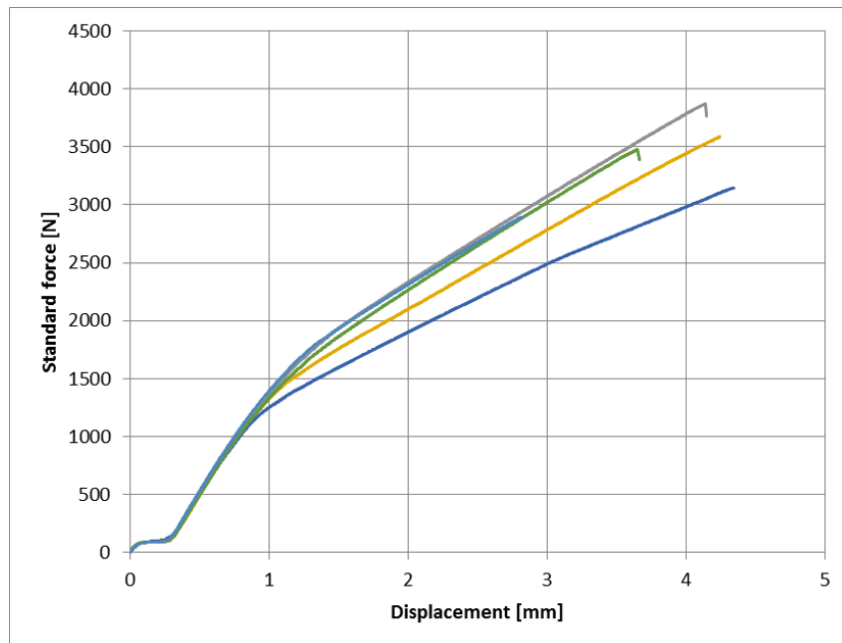


(b) Test speed 10 mm/min.

Figure C.2: Force-displacement curve for virgin/recycled material composition 75%/25%.

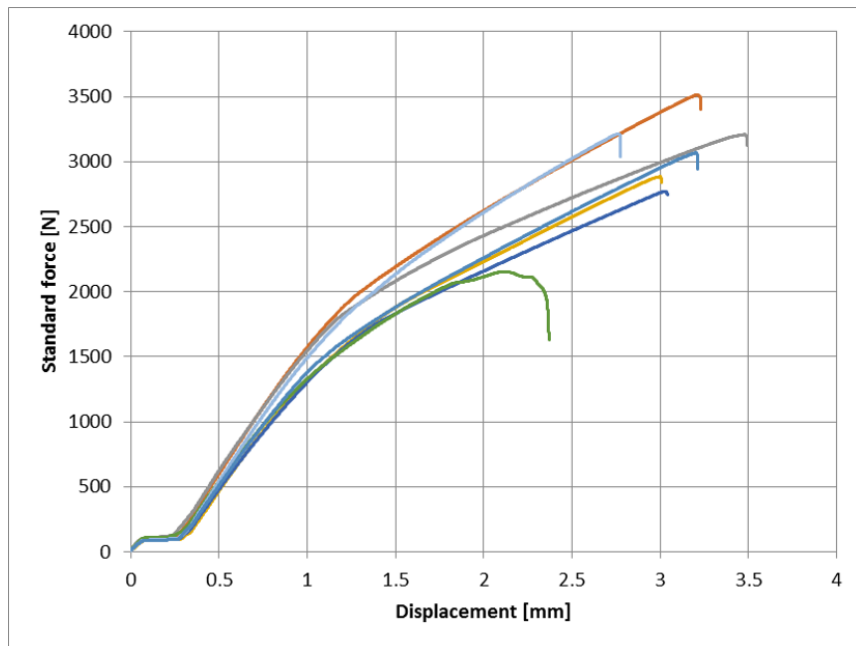


(a) Test speed 0.5 mm/min.

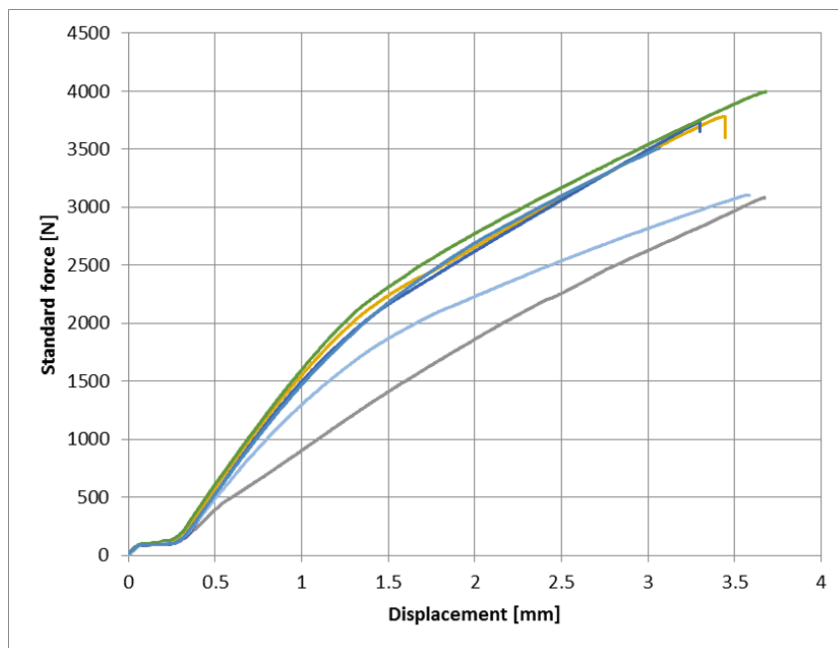


(b) Test speed 10 mm/min.

Figure C.3: Force-displacement curve for virgin/recycled material composition 50%/50%.



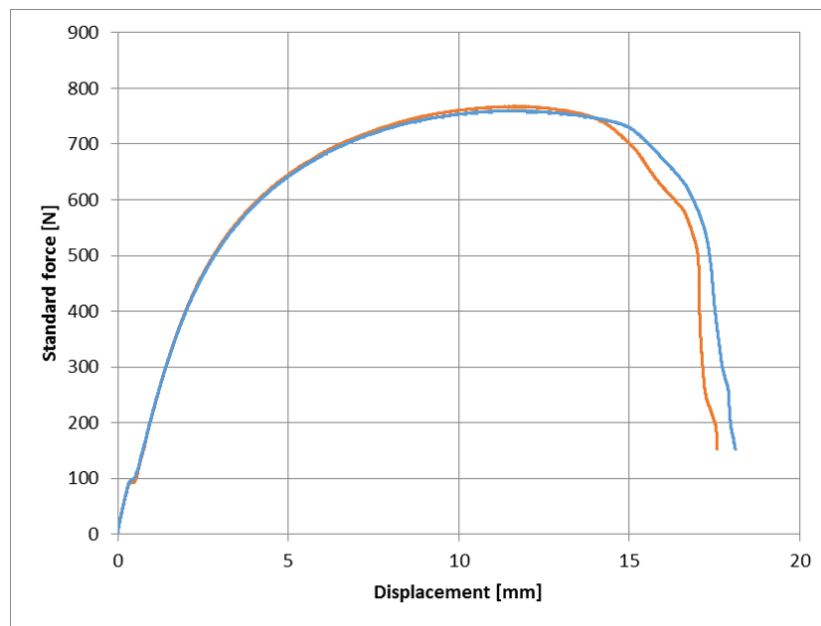
(a) Test speed 0.5 mm/min.



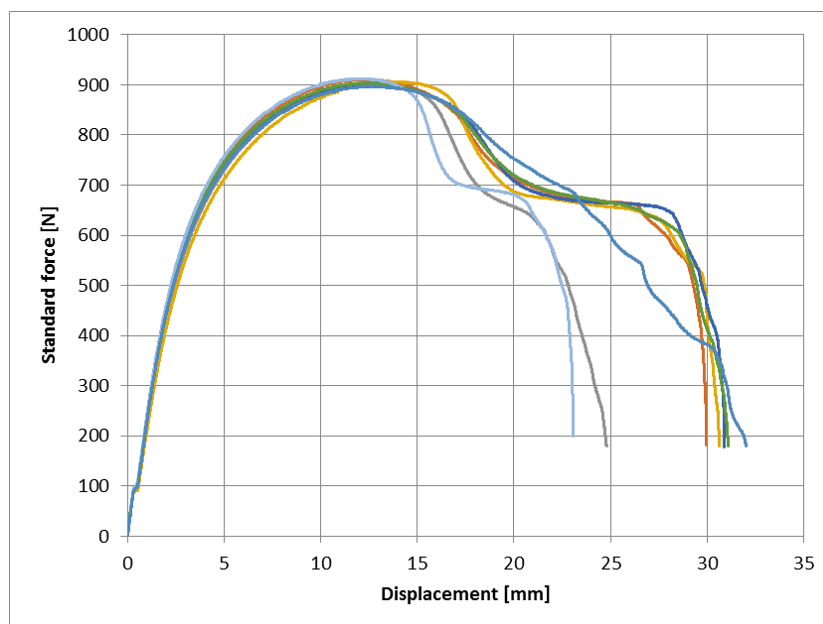
(b) Test speed 10 mm/min.

Figure C.4: Force-displacement curve for virgin/recycled material composition 25%/75%.

C.2. Composition test results: *Technomelt 3D 6910*

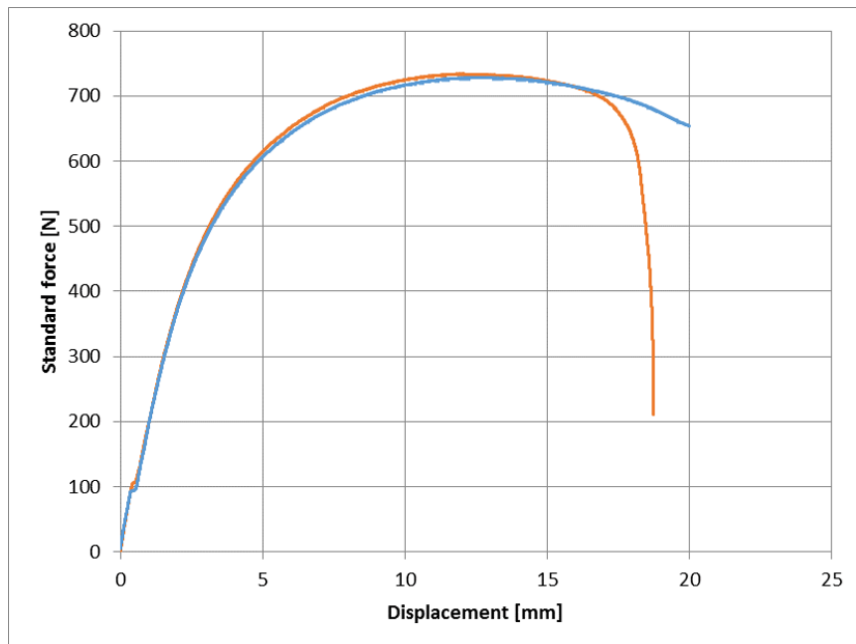


(a) Test speed 0.5 mm/min.

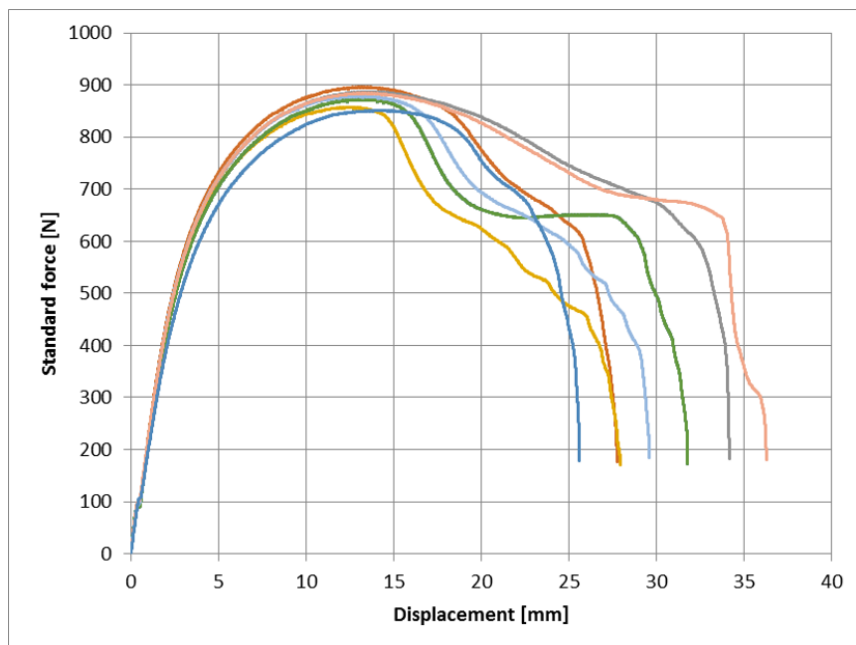


(b) Test speed 10 mm/min.

Figure C.5: Force-displacement curve for virgin/recycled material composition 100%/0%.

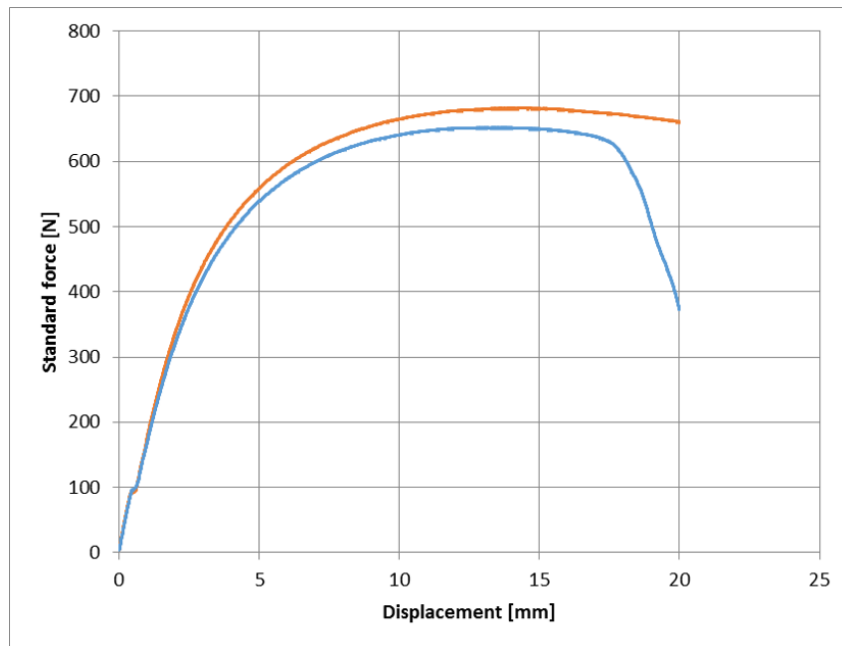


(a) Test speed 0.5 mm/min.

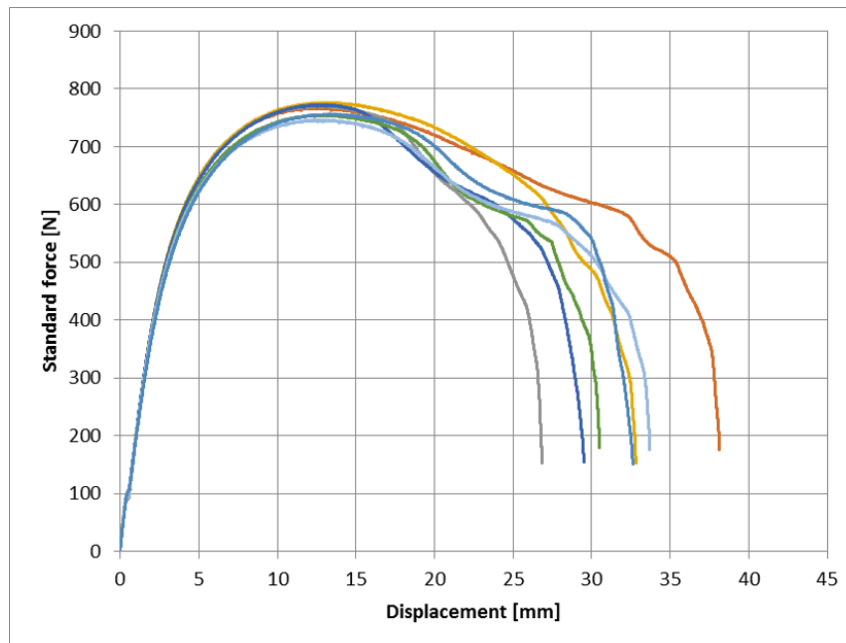


(b) Test speed 10 mm/min.

Figure C.6: Force-displacement curve for virgin/recycled material composition 75%/25%.

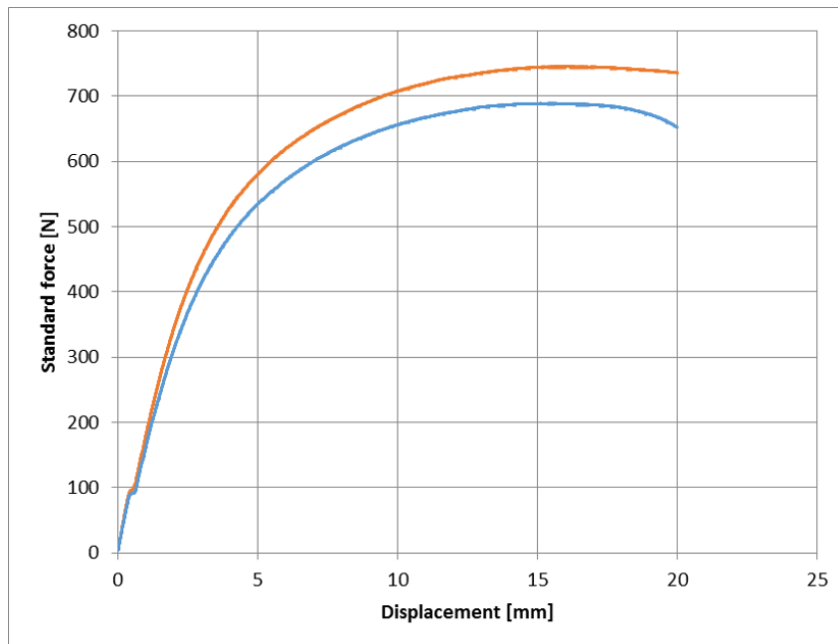


(a) Test speed 0.5 mm/min.

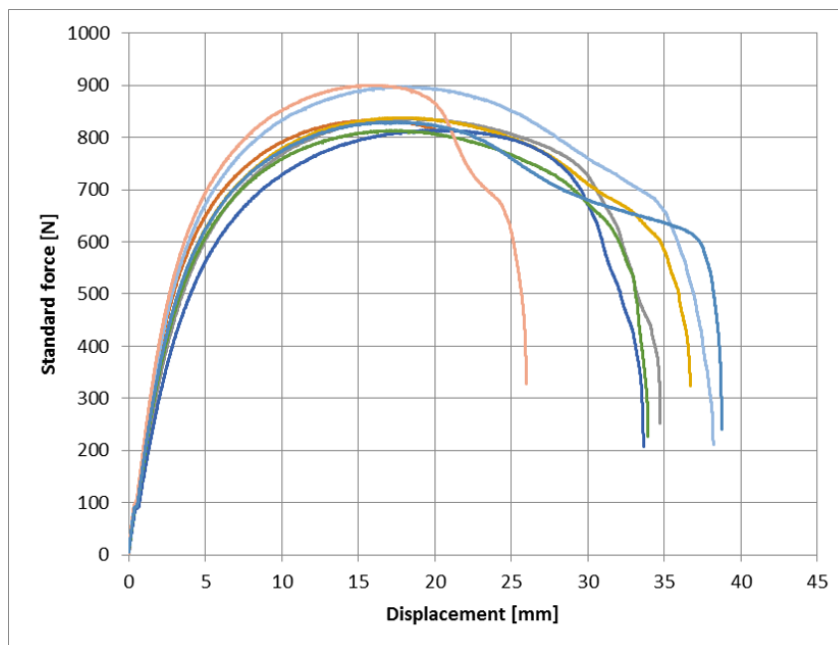


(b) Test speed 10 mm/min.

Figure C.7: Force-displacement curve for virgin/recycled material composition 50%/50%.

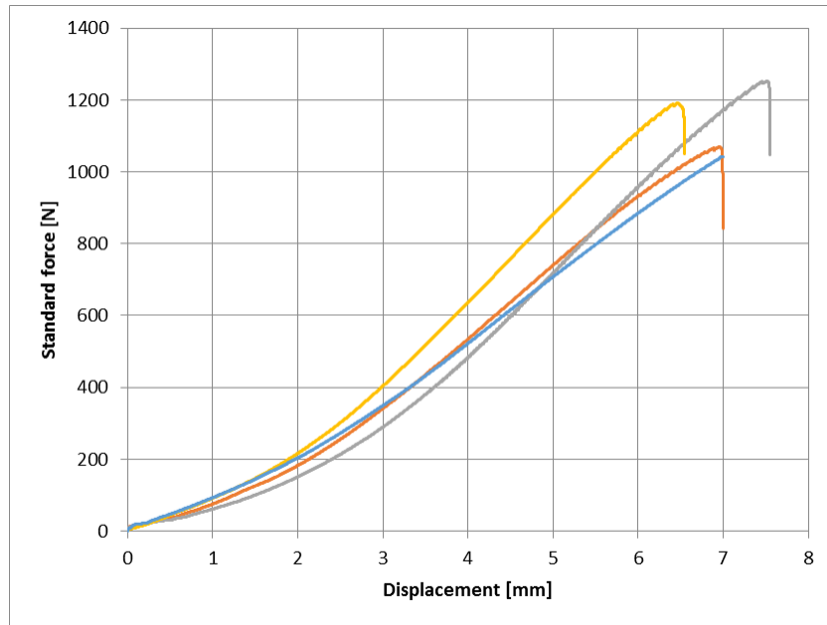


(a) Test speed 0.5 mm/min.

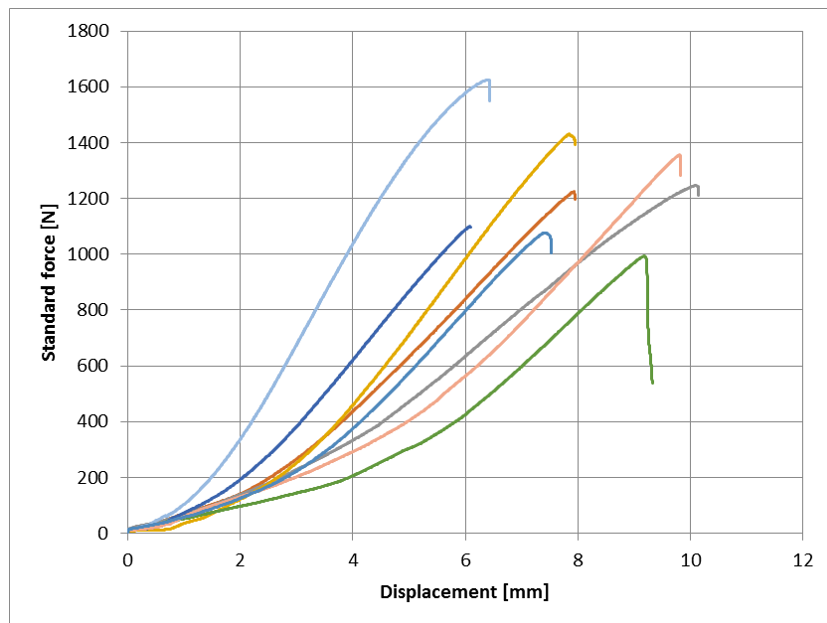


(b) Test speed 10 mm/min.

Figure C.8: Force-displacement curve for virgin/recycled material composition 25%/75%.

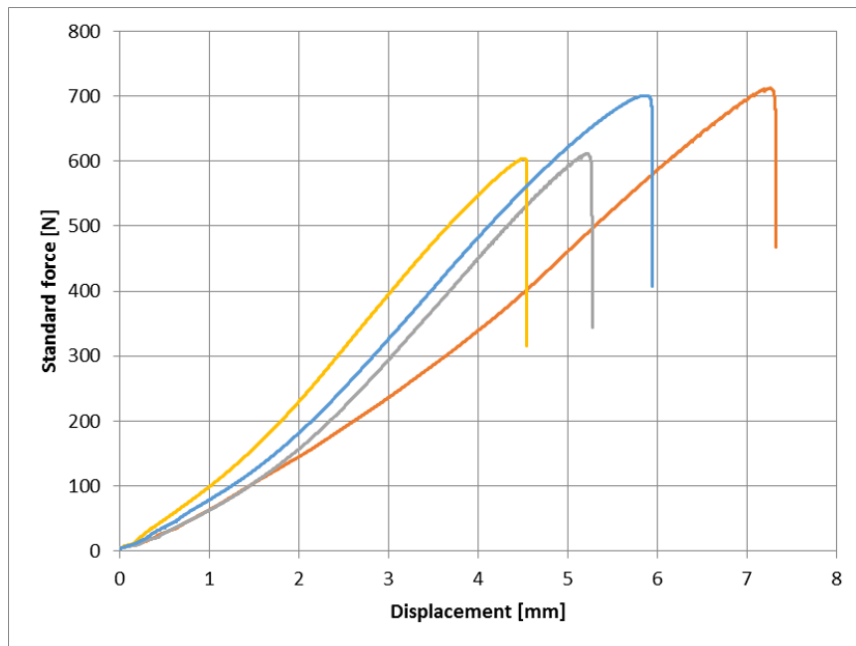
C.3. Composition test results: 60%LDPE 3+40%PPgf recycled

(a) Test speed 0.5 mm/min.

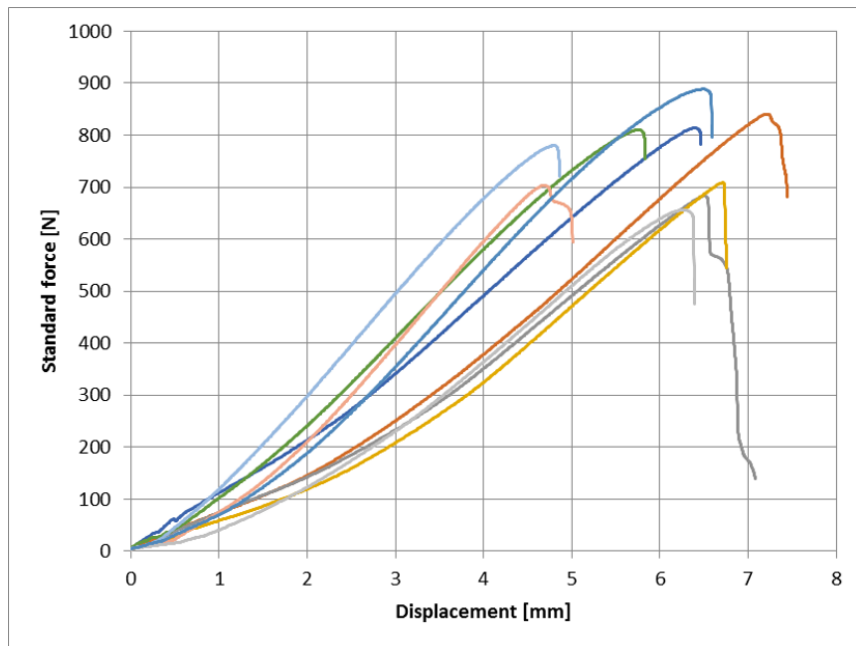


(b) Test speed 10 mm/min.

Figure C.9: Force-displacement curve for virgin/recycled material composition 100%/0%.

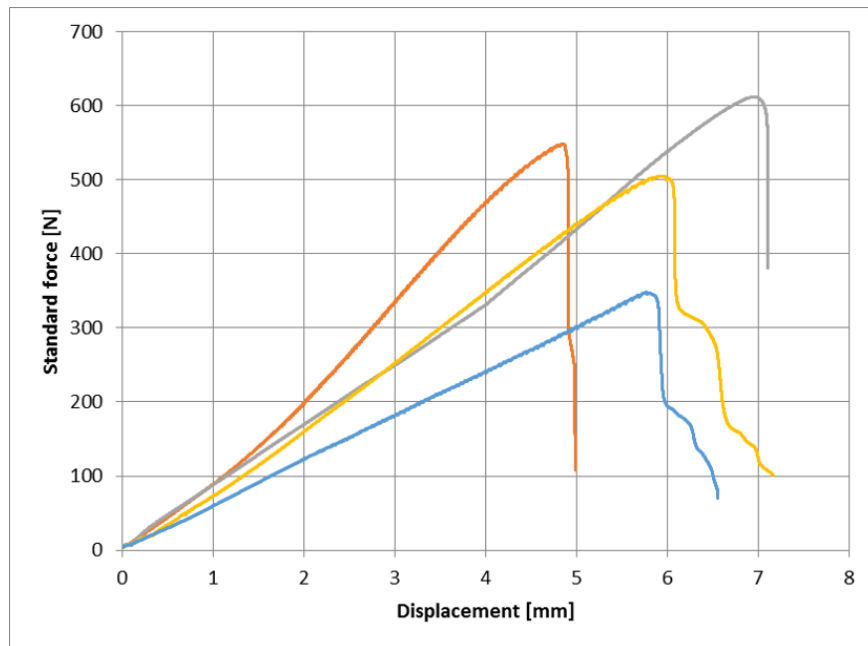


(a) Test speed 0.5 mm/min.

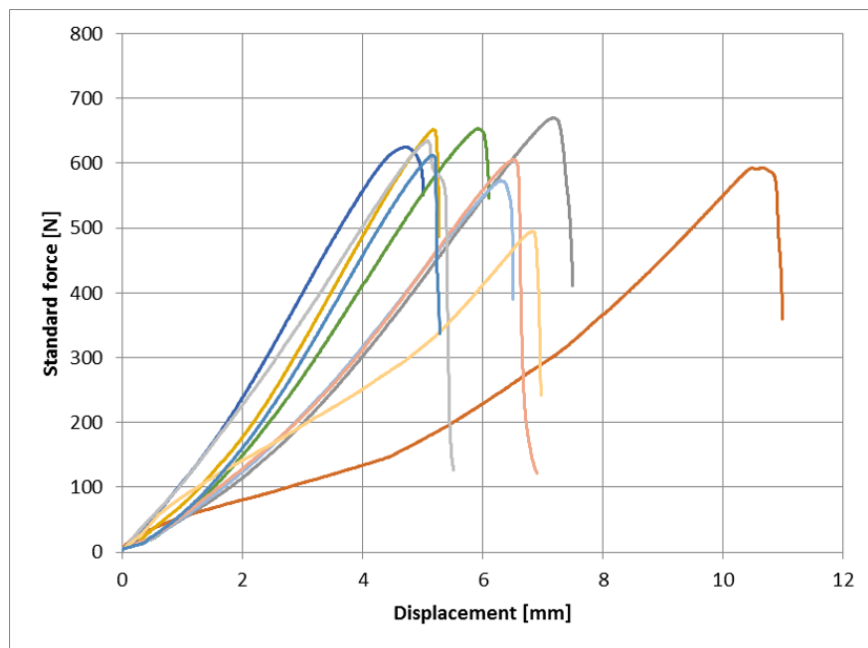


(b) Test speed 10 mm/min.

Figure C.10: Force-displacement curve for virgin/recycled material composition 75%/25%.

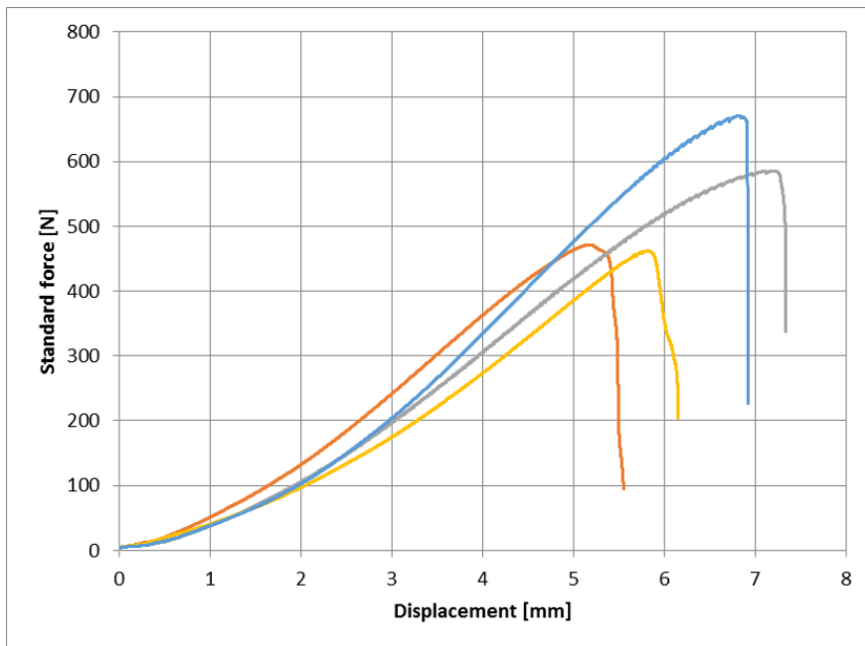


(a) Test speed 0.5 mm/min.

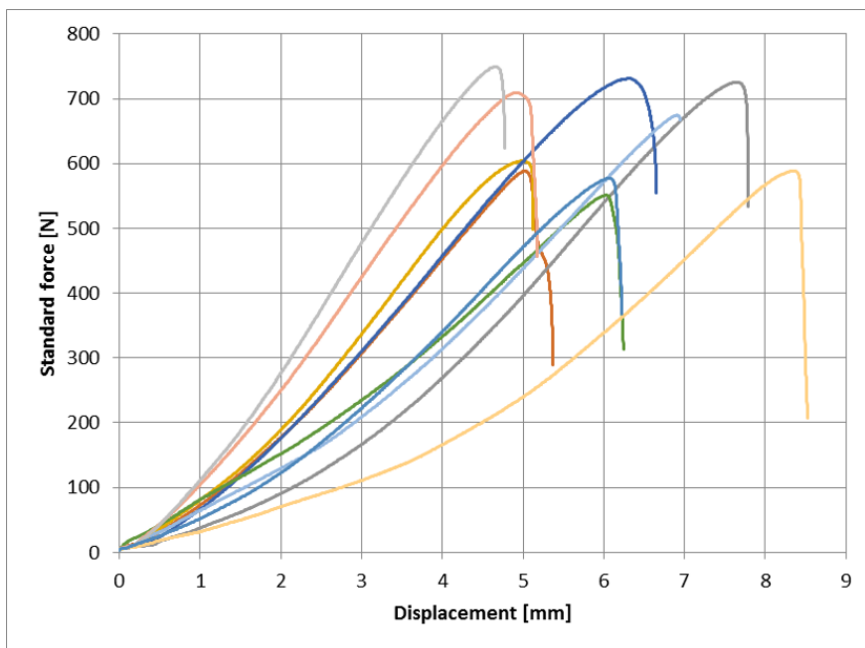


(b) Test speed 10 mm/min.

Figure C.11: Force-displacement curve for virgin/recycled material composition 50%/50%.



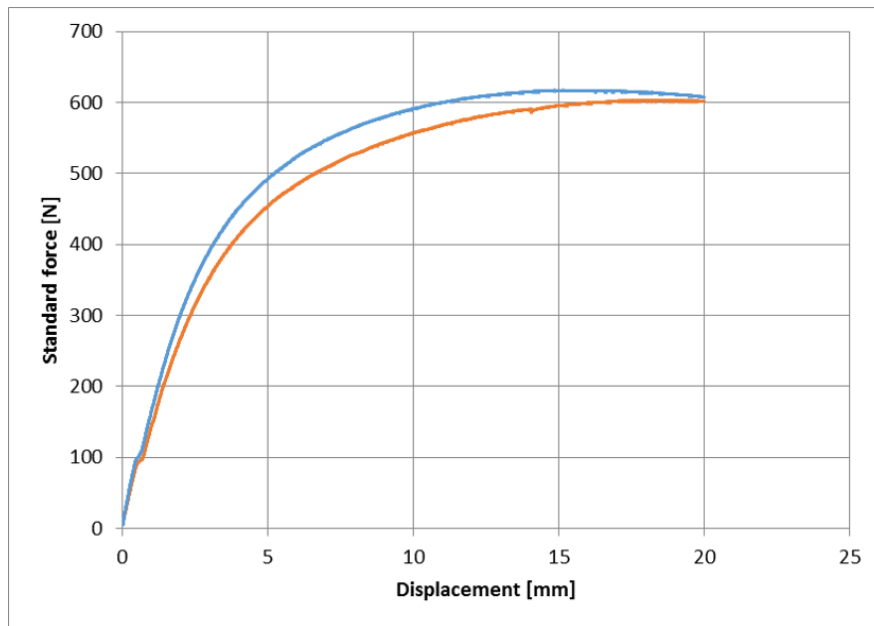
(a) Test speed 0.5 mm/min.



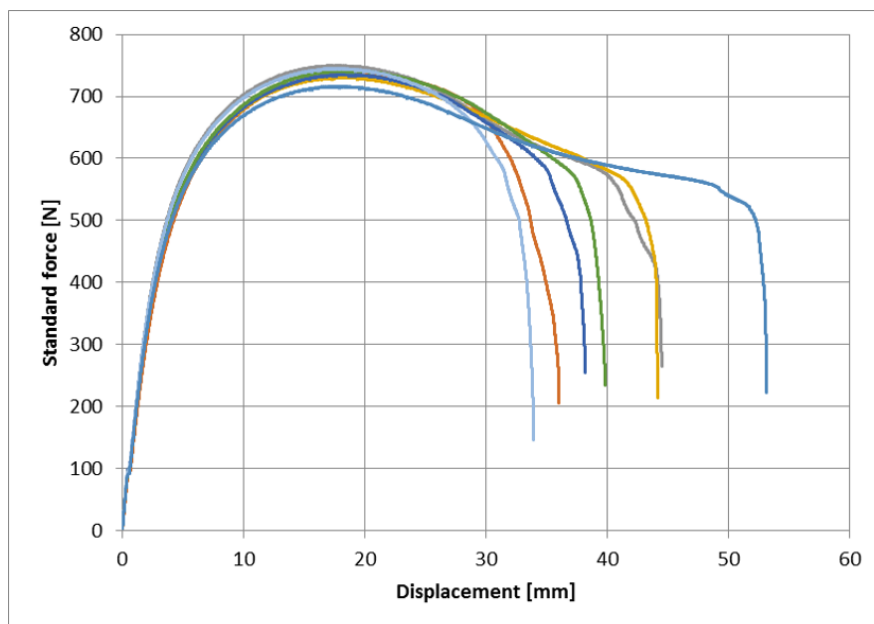
(b) Test speed 10 mm/min.

Figure C.12: Force-displacement curve for virgin/recycled material composition 25%/75%.

C.4. Recycling round test results: *Technomelt 3D 6910*

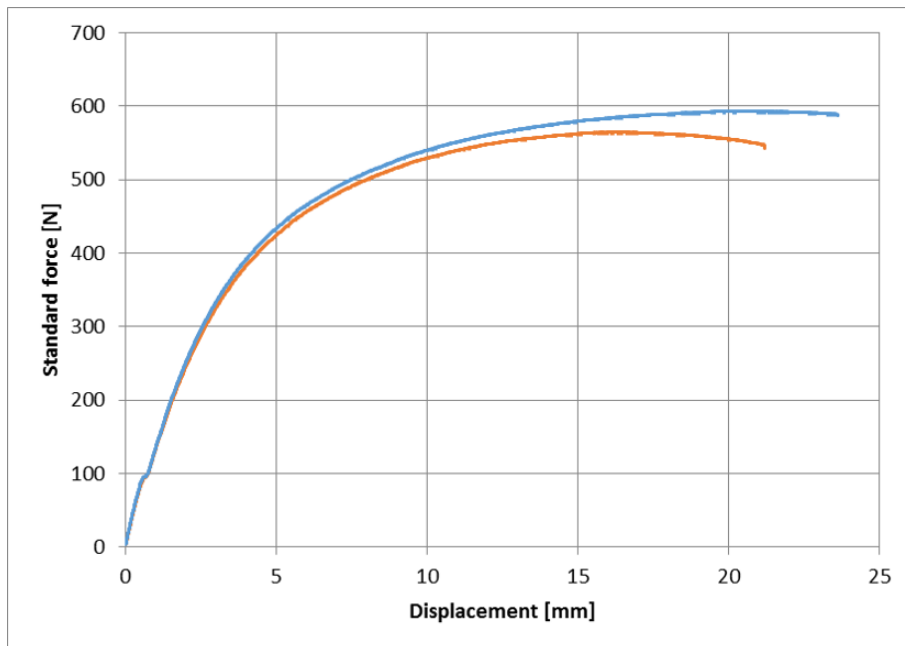


(a) Test speed 0.5 mm/min.

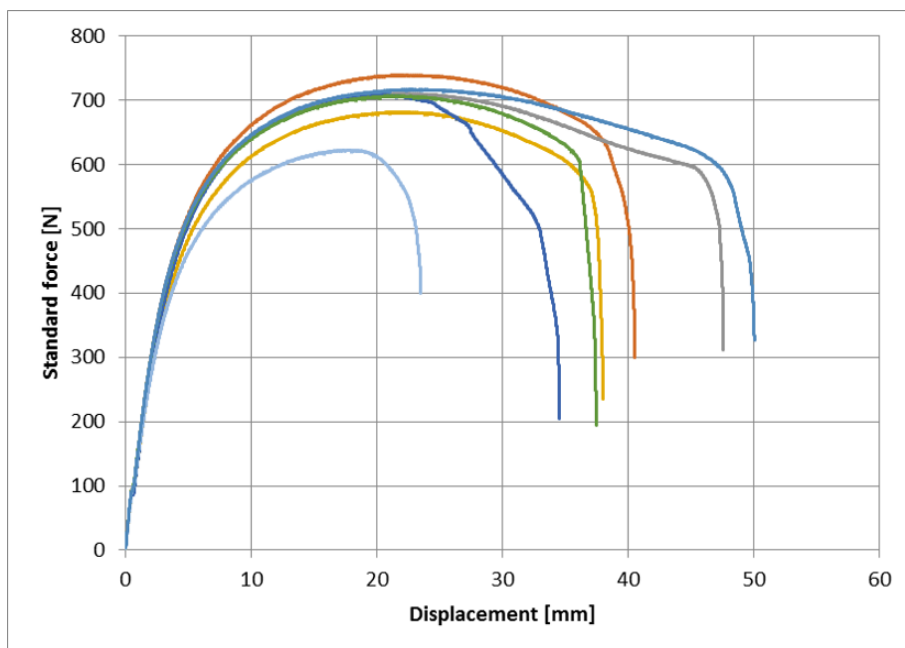


(b) Test speed 10 mm/min.

Figure C.13: Force-displacement curve for 1st round recycle material.

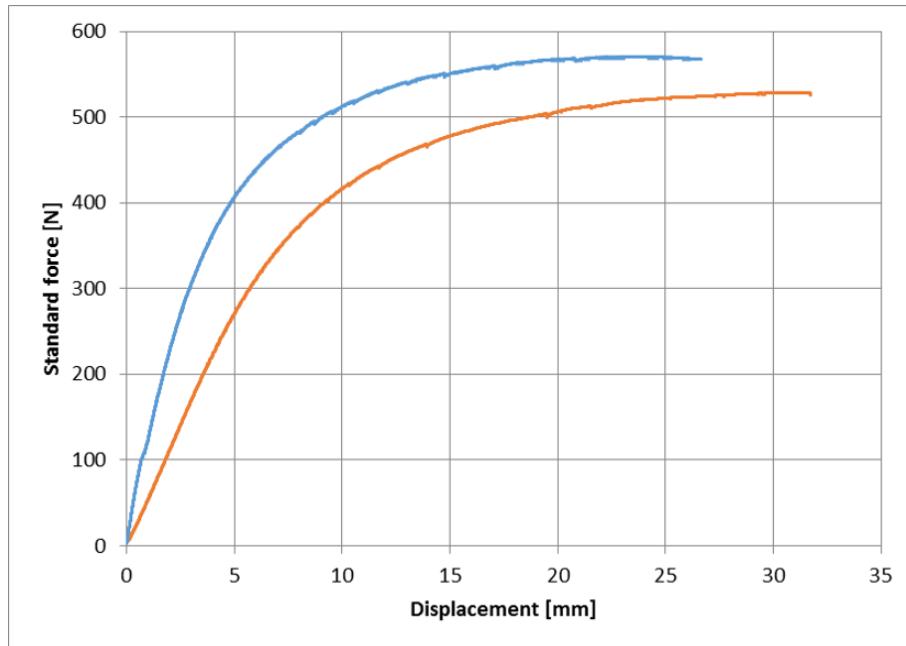


(a) Test speed 0.5 mm/min.

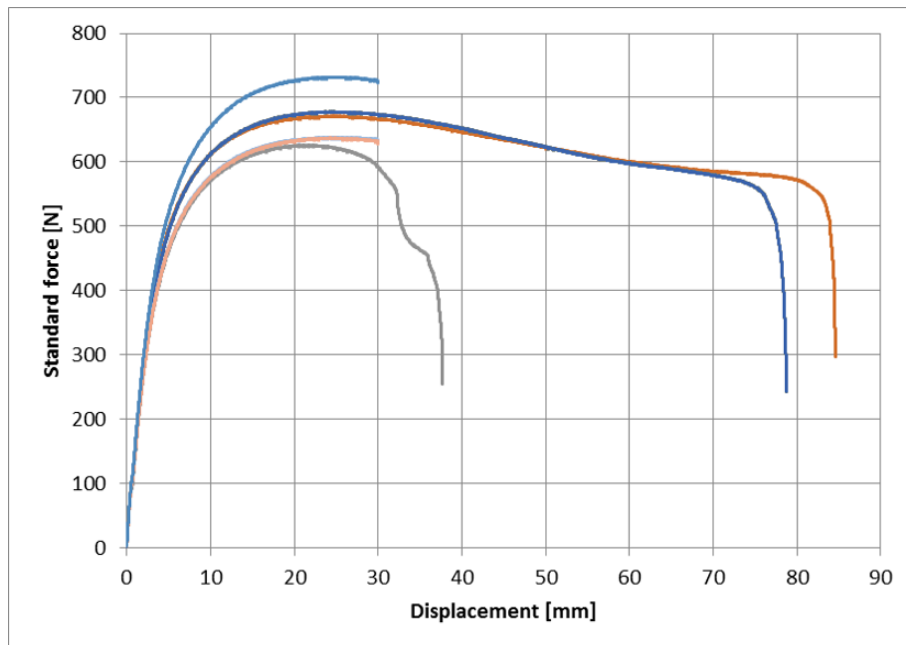


(b) Test speed 10 mm/min.

Figure C.14: Force-displacement curve for 2nd round recycle material.



(a) Test speed 0.5 mm/min.



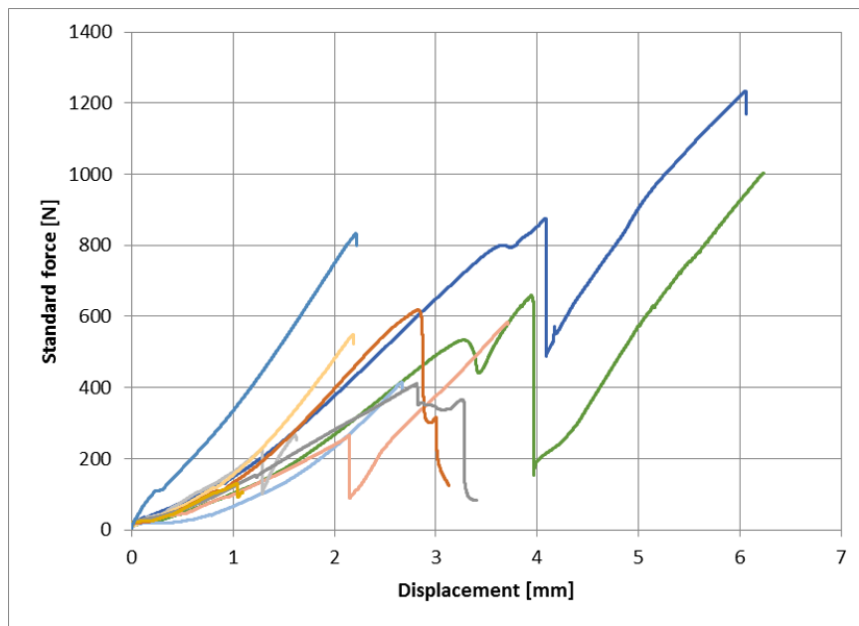
(b) Test speed 10 mm/min.

Figure C.15: Force-displacement curve for 3rd round recycle material.

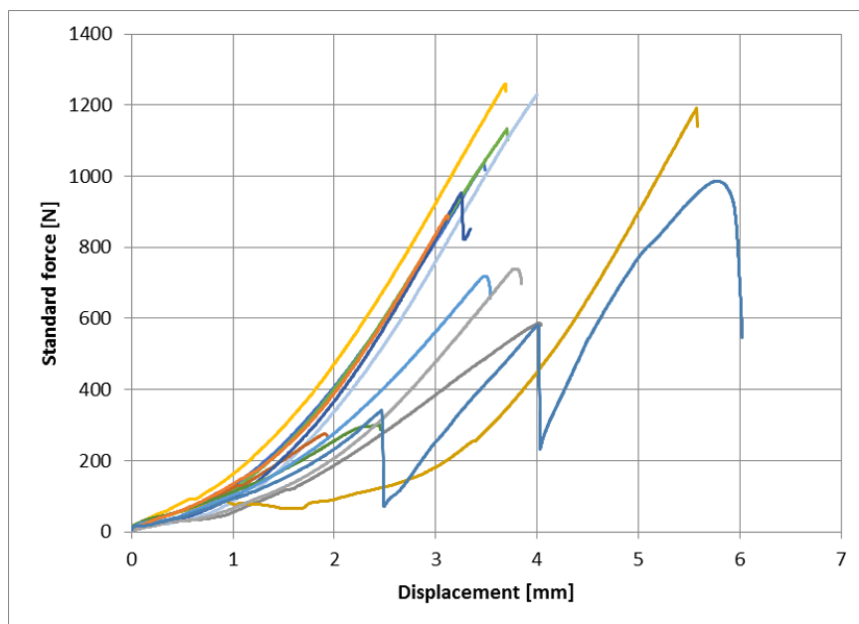
D

Raw data of other property test for
the selected material

D.1. Tensile test results

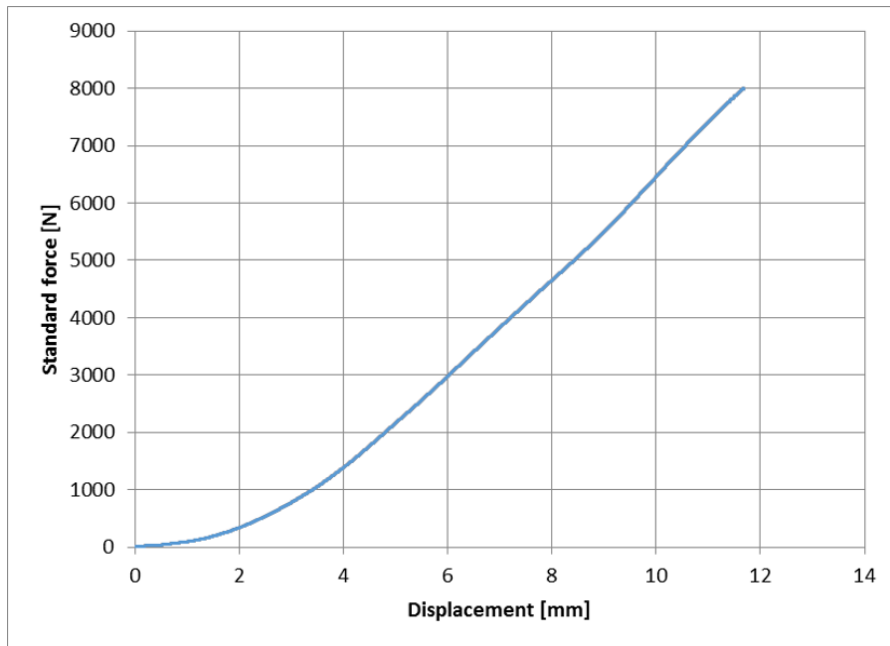


(a) Test speed 0.5 mm/min.

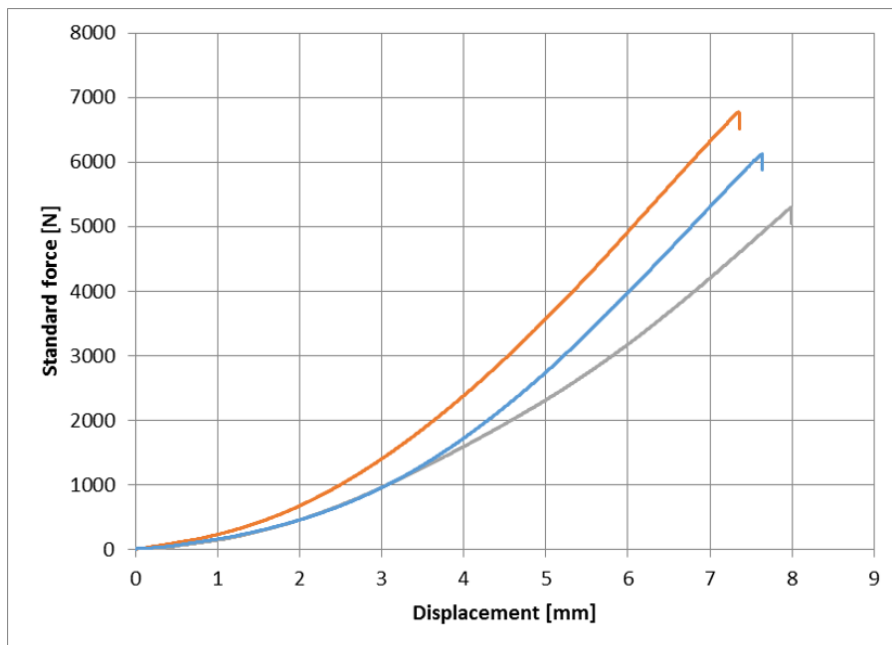


(b) Test speed 10 mm/min.

Figure D.1: Single layer transverse tensile test results.



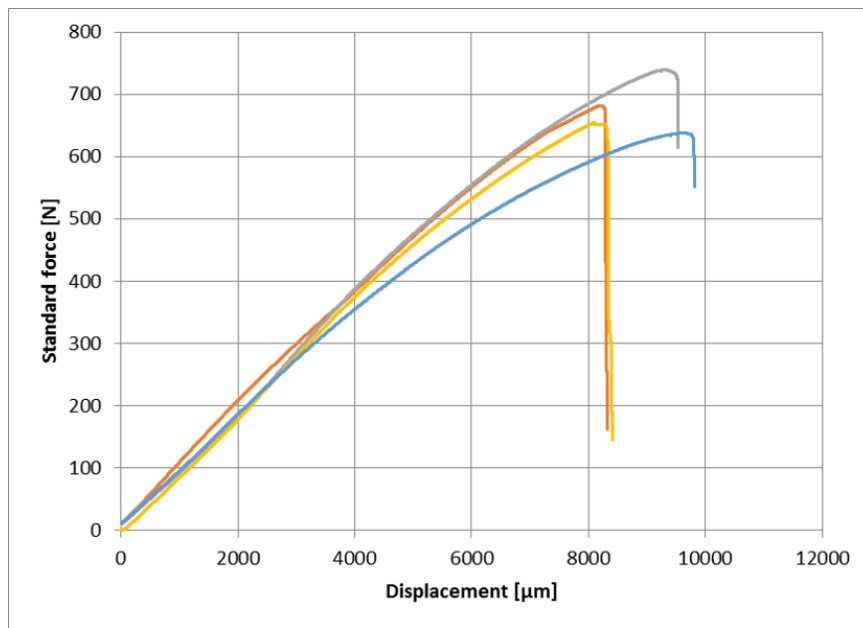
(a) Test speed 0.5 mm/min.



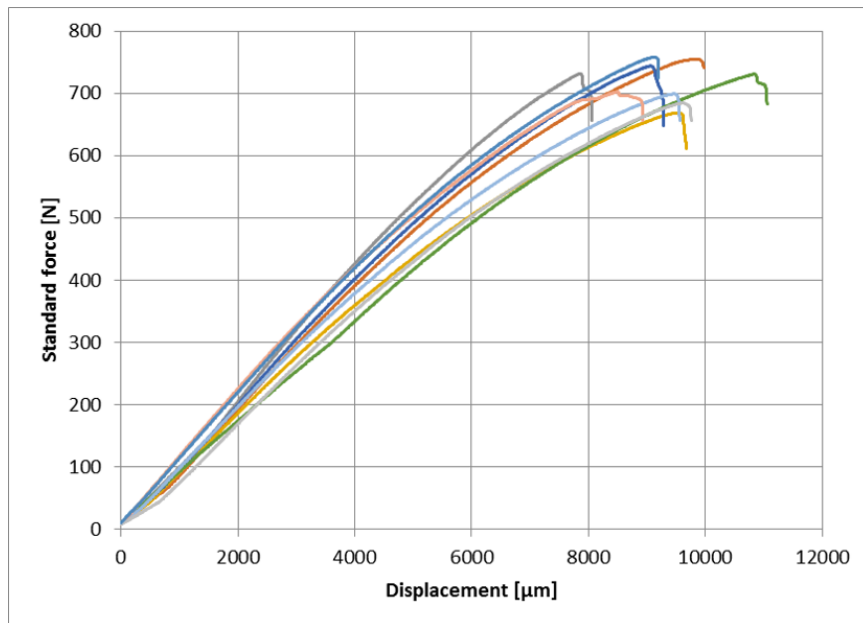
(b) Test speed 10 mm/min.

Figure D.2: Double layer longitudinal tensile test results.

D.2. Bending test results

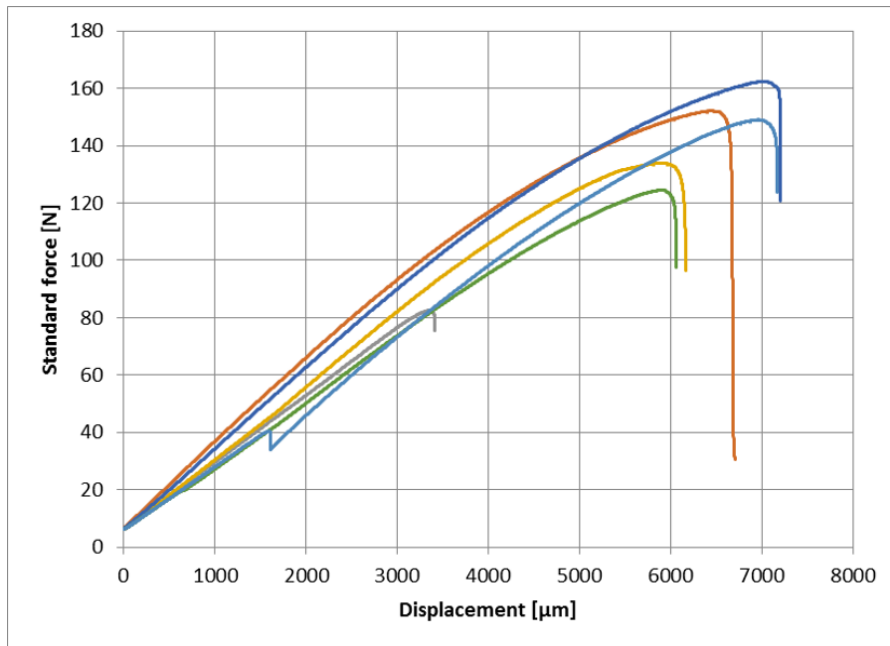


(a) Test speed 0.5 mm/min.

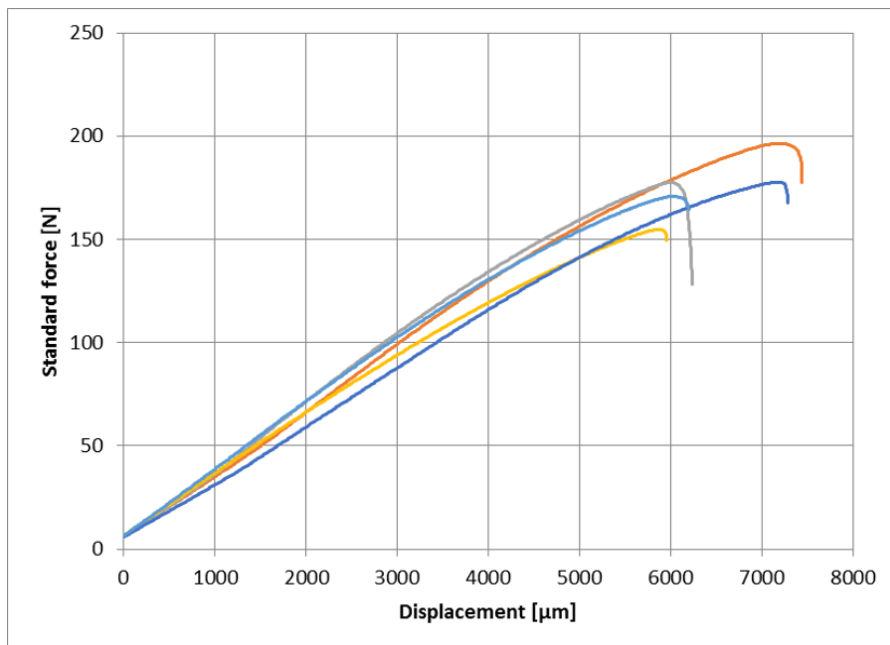


(b) Test speed 10 mm/min.

Figure D.3: Single layer longitudinal bending test results.

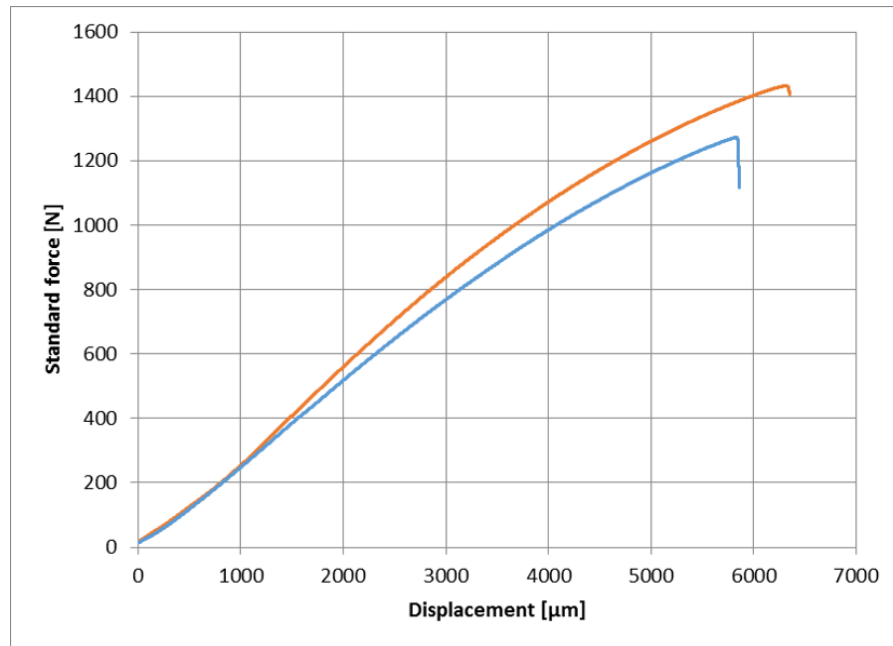


(a) Test speed 0.5 mm/min.

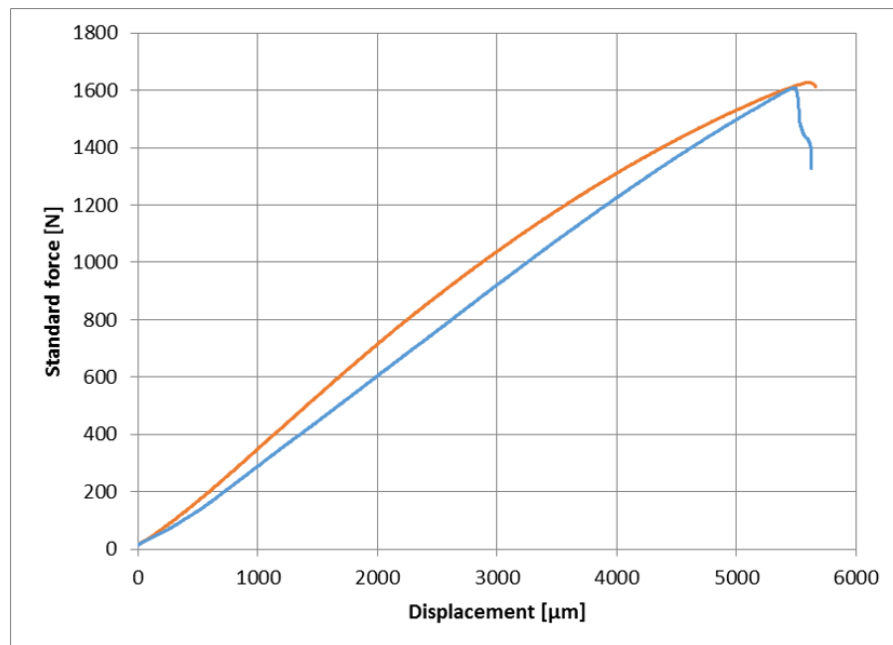


(b) Test speed 10 mm/min.

Figure D.4: Single layer transverse bending test results.



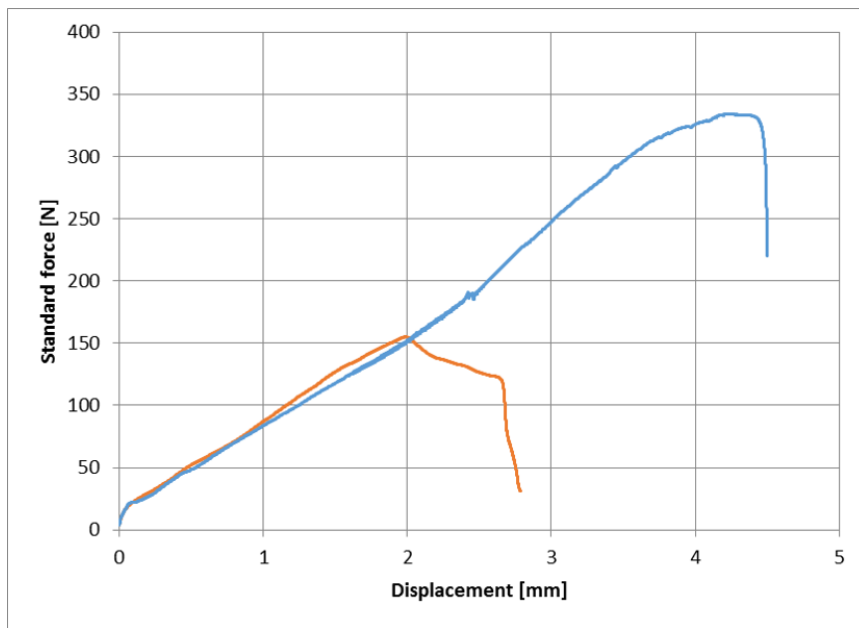
(a) Test speed 0.5 mm/min.



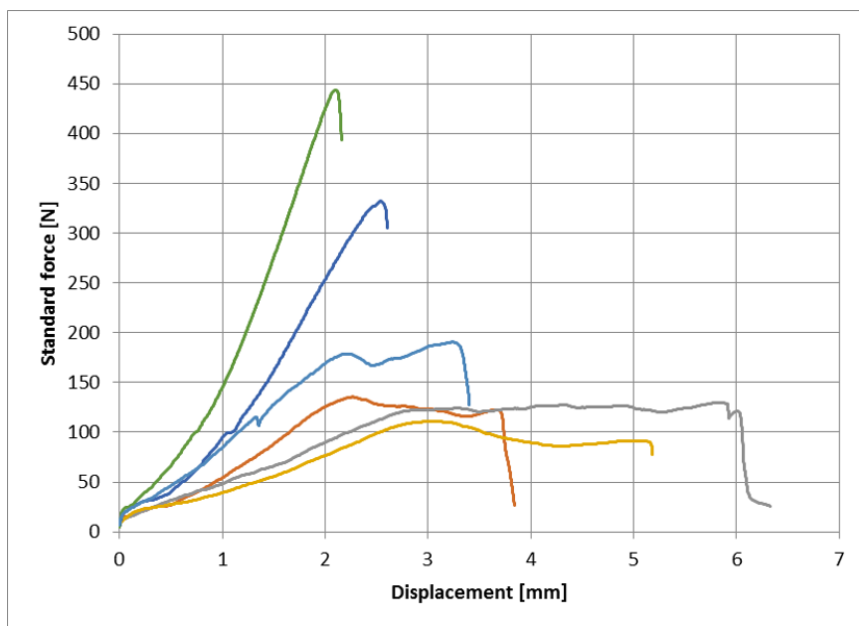
(b) Test speed 10 mm/min.

Figure D.5: Double layer longitudinal bending test results.

D.3. Shear test results

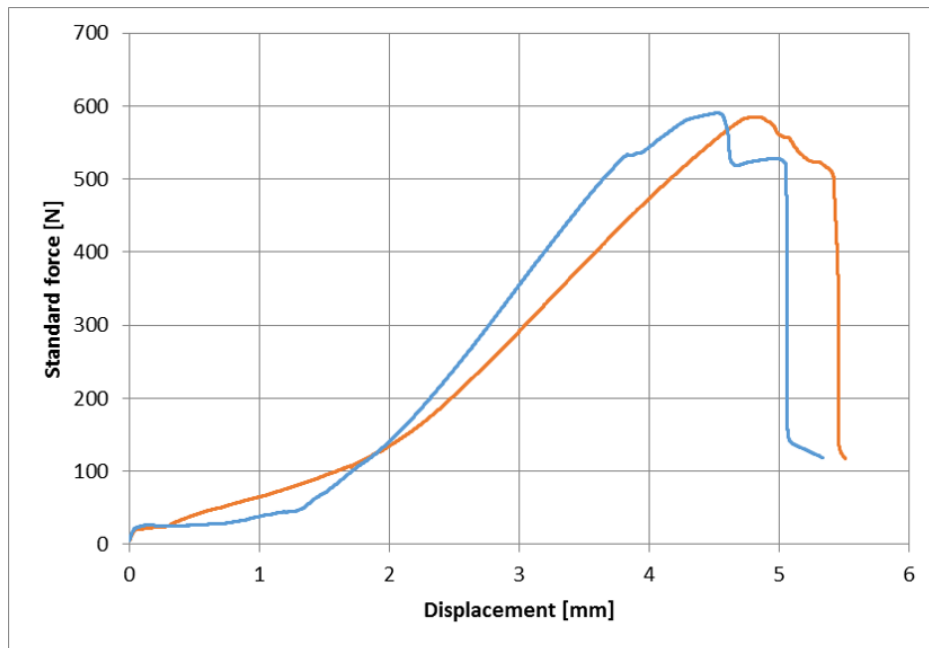


(a) Test speed 0.5 mm/min.

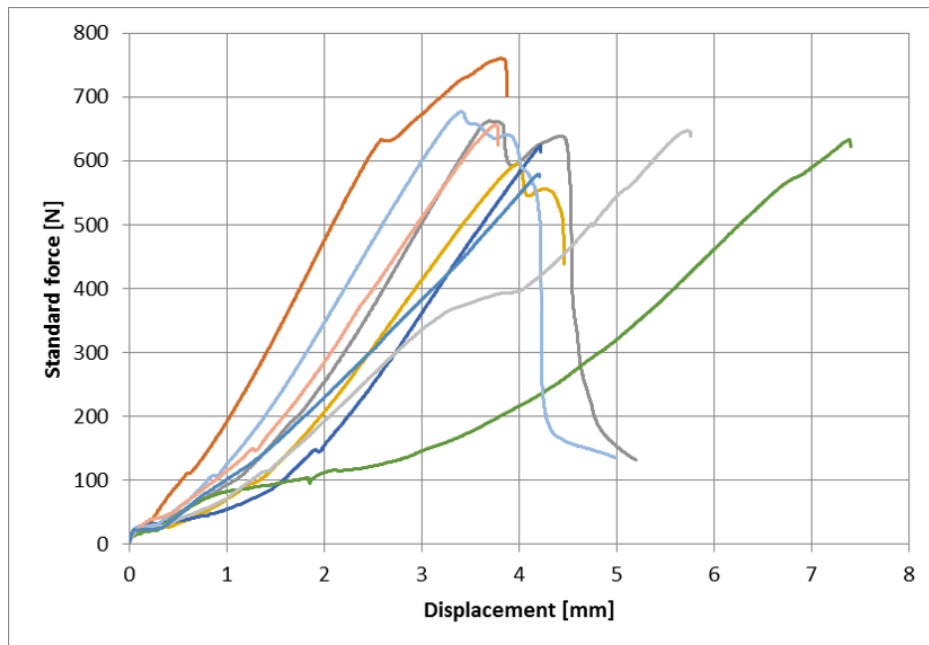


(b) Test speed 10 mm/min.

Figure D.6: Single layer longitudinal shear test results.

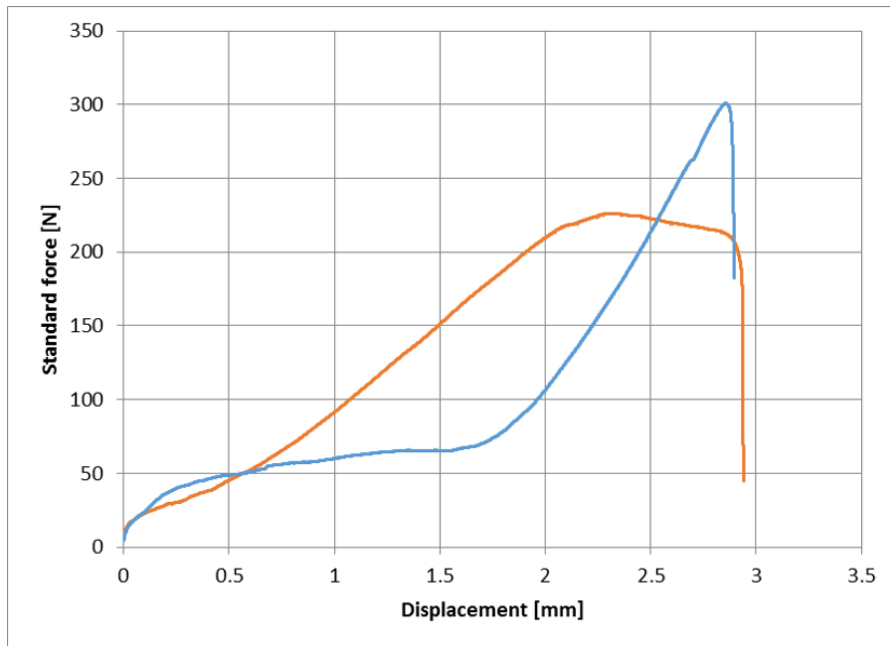


(a) Test speed 0.5 mm/min.

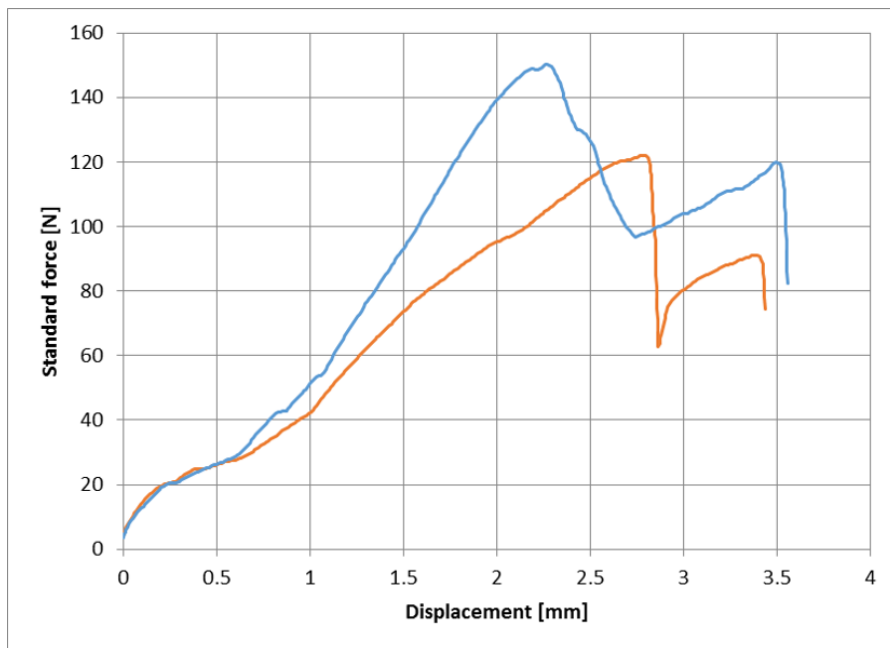


(b) Test speed 10 mm/min.

Figure D.7: Single layer transverse shear test results.

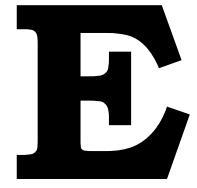


(a) Test speed 0.5 mm/min.



(b) Test speed 10 mm/min.

Figure D.8: Double layer longitudinal shear test results.



Effective length for tensile test

Due to the limitation of the laboratory conditions, there was no gage used for measuring the strain of the samples. Therefore, the results derived from the tensile test need to use effective length for calculating the desired mechanical properties. First of all, the tensile specimen has form and dimensions as in Fig. E.1:

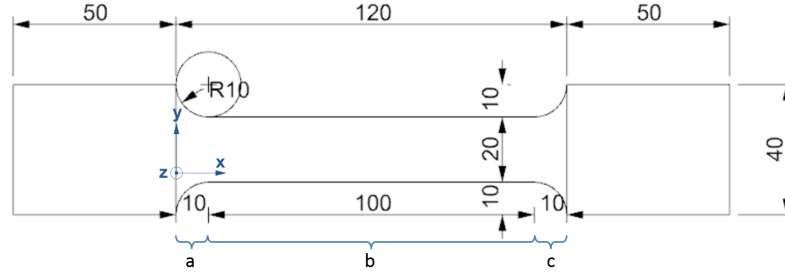


Figure E.1: Specimen for tensile test.

The narrowing part can be divided into three sections: a , b and c . With the coordinate system defined in Fig. E.1, the cross-sectional area of each section can be calculated:

$$A(x) = \begin{cases} a : t(40 - 2\sqrt{100 - (x - 10)^2}) & 0 \leq x \leq 10 \\ b : 20t & 10 < x < 110 \\ c : t(40 - 2\sqrt{100 - (x - 110)^2}) & 110 \leq x \leq 120 \end{cases} \quad (\text{E.1})$$

where:

t is the nominal thickness.

Then the normal force/displacement relationship can be derived according to the linear theory, and it has a form as follow

$$\delta = \int_0^L \frac{Ndx}{EA(x)} \quad (\text{E.2})$$

where:

N is the normal force.

δ is the normal displacement.

E is the Young's modulus.

L is the length.

Next, by combining Eqs. (E.1) and (E.2), the displacement with equivalent length can be derived as follow:

$$\delta_{eq} = \frac{N \left(\frac{\pi(8\sqrt{3} - 9)}{18t} \right) + \frac{5}{t}}{E} \quad (\text{E.3})$$

Finally, by comparing with the uniform cross-section with 120mm long and $20t$ as area, the effective length can be derived:

$$\delta_{120} = \frac{N}{Et} \int_0^{120} \frac{dx}{120} = \frac{6N}{Et} \quad (\text{E.4})$$

$$L_{eff} = 120 \frac{\delta_{eq}}{\delta_{120}} = \frac{80\pi\sqrt{3}}{9} - 10\pi + 100 \quad (\text{E.5})$$

The effective length can be approximated to 116.95mm.

F

Hydrostatic pressure during concrete casting

The load within this research is mainly the hydrostatic pressure from the fresh concrete during the casting. According to Puente, Santilli and Lopez [72], the lateral pressure can be given in:

$$P = \lambda_c \gamma H \quad (\text{F.1})$$

where:

λ_c is the relationship between vertical and horizontal pressure.

γ is the concrete density.

H is the casting height.

The value of λ_c depends on the fluidity of the concrete during the casting and varies from zero to one. Within this project, it assumes the full fluidity of the concrete and λ_c , therefore, equals to one.

Moreover, the hydrostatic pressure from the fresh concrete is also related to the rate of placement R and setting time t_E [73]. However, they are ignored within this project and the pressure is assumed as fully hydrostatic and time independent.

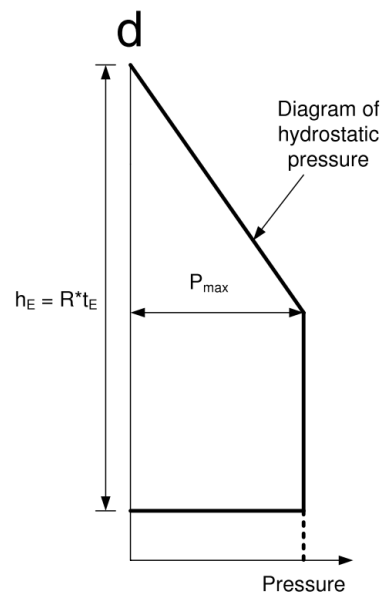


Figure F.1: Experimental diagrams of pressure envelope [72].

G

Mathematical limitation of using
triple-layer shell element

In order to utilize triple-layer shell element, several parameters need to be defined: the thickness t_1 and t_2 , and the corresponding Young's modulus E_1 and E_2 . For the sake of simplicity, only one direction is presented. In Fig. G.1, these parameters are presented in local coordinate system¹.

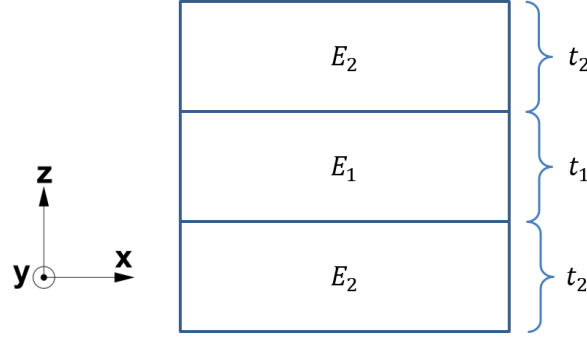


Figure G.1: Experimental diagrams of pressure envelope [72].

Assuming the nominal thickness is t , the relationship between normal Young's modulus, flexural Young's and the rest parameters can be express as follow:

$$E_{normal}t = E_1t_1 + 2 \cdot E_2t_2 \quad (G.1a)$$

$$E_{flexural}t^3 = E_1t_1^2 + E_2(t^3 - t_1^3) \quad (G.1b)$$

$$t = t_1 + 2t_2 \quad (G.1c)$$

By solving the Eq. (G.1), it yields E_1 and E_2 :

$$E_1 = \frac{(-E_{flexural} + 3E_{normal})t^2 - 3E_{normal}t \cdot (t - t_1) + E_{normal}(t - t_1)^2}{(2t - 2t_2)(t - 2t_2)} \quad (G.2a)$$

$$E_2 = \frac{-4E_{normal}t_2^2 + 4E_{normal}t_2 + t^2(E_{flexural} - E_{normal})}{4t_2(t - t_2)} \quad (G.2b)$$

Both E_1 and E_2 should be positive, and the denominators of both equations in Eq. (G.2) are positive, thus their numerators should be positive as well. Then E_1, E_2 can be represented by the function of their numerators E'_1, E'_2 . Following steps will only elaborate the results of E_1 , and the corresponding procedure of E_2 yields same results.

$$E'_1 = E_{normal}t_1^2 + E_{normal}t \cdot t_1 + (E_{normal} - E_{flexural})t^2 \quad (G.3)$$

Assuming t is constant, then Eq. (G.3) can be rewritten into vertex form:

$$E'_1 = E_{normal}\left(t_1 + \frac{t}{2}\right)^2 + t^2\left(\frac{3}{4}E_{normal} - E_{flexural}\right) \quad (G.4)$$

Considering both t_1 and E_1 need to be positive, and $0 \leq t_1 \leq t$, $E_{flexural}$ and E_{normal} have boundaries as follow:

$$\begin{cases} 3E_{normal} > E_{flexural} > E_{normal} & , t \sqrt{\frac{E_{flexural}}{E_{normal}}} - \frac{3}{4} - \frac{t}{2} \leq t_1 \leq t \\ E_{flexural} < E_{normal} & , 0 \leq t_1 \leq t \sqrt{\frac{E_{flexural}}{E_{normal}}} \end{cases} \quad (G.5)$$

Therefore, $E_{flexural} : E_{normal}$ cannot exceed 3 : 1 if triple-layer shell element is utilized.

¹See Section Section 2.4 for the definition of local coordinate system.

H

Derivation of the material inputs for
the shell element

Since the material can be regarded as polymer composites reinforced by glass fibre, its properties can be estimated by the method named Halpin-Tsai semi-empirical equation [74]. This method was also used by Baran for estimating the properties of 3D printed components with *Technomelt 3D 6910* [35]. In the following introduction, the properties related to the polymer matrix, i.e. polypropylene in this research, have a subscript of m , and that related to the glass fibre have a subscript of f . The coordinate system defines the x (or 1) axis coincides the direction of the glass fibre, which is also the printing direction, and y (or 2) axis is perpendicular to the printing direction.

First of all, the Poisson ratio ν_{12} of the composite can be defined according to Eq. (H.1), and by substituting the values and ν_{12} is equal to 0.39.

$$\nu_{12} = \nu_f \nu_f + \nu_m \nu_m \quad (\text{H.1a})$$

$$\nu_f = \frac{M_f \rho_m}{M_f \rho_m + M_m \rho_f} \quad (\text{H.1b})$$

$$\nu_m = 1 - \nu_f \quad (\text{H.1c})$$

where:

ν is the Poisson ratio. 0.22 for the glass fibre and 0.42 for the matrix.

ν is the volume fraction.

M is the mass. Glass fibre content is 30% in this research.

ρ is the density. $2.5g/cm^3$ for glass fibre and $1.12g/cm^3$ for the matrix.

It is explained in Section 5.5 that the printed wall can be treated as transverse isotropic material. Therefore, $\nu_{12} = \nu_{13} = 0.39$ and $\nu_{23} = 0.42$. Next, the shear modulus can be estimated according to Eq. (H.2):

$$E_2 = E_3 \quad (\text{H.2a})$$

$$G_{23} = \frac{E_2}{2(1 + \nu_{23})} \quad (\text{H.2b})$$

$$G_{12} = G_{13} = \frac{1 + \eta_G \nu_f}{1 - \eta_G \nu_f} G_{23} \quad (\text{H.2c})$$

$$\eta_G = \frac{G_f - G_{23}}{G_f + G_{23}} \quad (\text{H.2d})$$

where:

E is the Young's modulus derived for the material tests.

G is the Shear modulus.

Finally, the 9 constants, i.e. Young's modulus, shear modulus and Poisson ratios in three directions, of the material properties input for triple-layer shell element can be derived according to the Young's modulus of each layer, and the values are listed in Table 5.1. It should be noted, these estimated values need to be verified for the actual structural application.



Definition of the maximum side length of hexagon

In order to use the regular hexagon as the planar pattern for the moulds, the size of it needs to be defined and is limited by the local yielding criteria. Assuming a 50mm wide strip, and the total concrete height is 1000mm, then the distributed load is around 1.2N/mm.

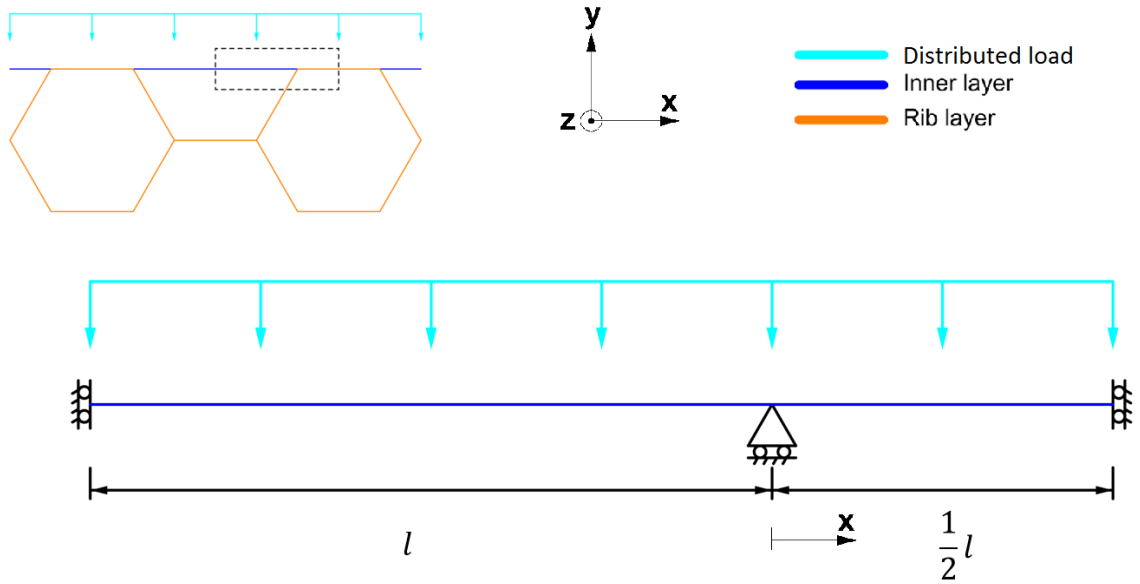


Figure I.1: The mechanical model for calculating the maximum side length l of the regular hexagon.

Assuming the origin point is as shown in Fig. I.1, the section with $x > 0$ is double-layer, and the section with $x < 0$ is single-layer. By applying Euler–Bernoulli beam theory, several boundary conditions (Eq. (I.2)) can be established for the differential equation Eq. (I.1):

$$EI \frac{d^4 v}{dx^4} = q \quad (\text{I.1})$$

$$\begin{cases} \theta(-l) = 0 \\ v(0) = 0 \\ \theta(\frac{1}{2}l) = 0 \\ \theta(0)_{left} = \theta(0)_{right} \end{cases} \quad (\text{I.2})$$

where:

θ is rotation.

v is deflection.

E is flexural Young's modulus.

q is distributed load.

The criterion are the bending moments at $x = -l$ and $x = \frac{1}{2}l$. They should not exceed the flexural yielding criteria defined in Table 4.6 for double-layer and single-layer printing. Then by solving the differential equation (Eq. (I.1)) with the boundary conditions (Eq. (I.2)), the maximum value l of single-layer section and double-layer section can be defined as follow:

$$\begin{cases} l_{max,single} = -\frac{\sqrt{3}\sqrt{q(k_{single} - k_{double})}M_{max,single}(k_{single} - 2k_{double})}{q(k_{single} - k_{double})} \\ l_{max,double} = -\frac{2\sqrt{6}\sqrt{q(k_{single} - 10k_{double})}M_{max,double}(k_{single} - 2k_{double})}{q(k_{single} - 10k_{double})} \end{cases} \quad (I.3)$$

where:

k is equal to EI . $2953 \times 10^4 mm^4$ for single-layer and $10457 \times 10^4 mm^4$ for double-layer.

M_{max} is the corresponding bending moment at flexural yielding strain. $3126 N \cdot mm$ for single-layer and $8014.85 N \cdot mm$ for double-layer.

Finally, $l_{max,single}$ and $l_{max,double}$ have values of $136.76 mm$ and $168.32 mm$ respectively. The maximum side length of regular hexagon used in this research is $100 mm$ which fulfils the requirements.

J

Conversion from the homogenized properties to the element properties

Homogenized properties of the regular hexagon need to be converted into the properties of the volumetric element. As shown in Fig. J.1, which is same as Fig. 5.20, the homogenized element has free dimensions while the volumetric element has predefined dimensions.

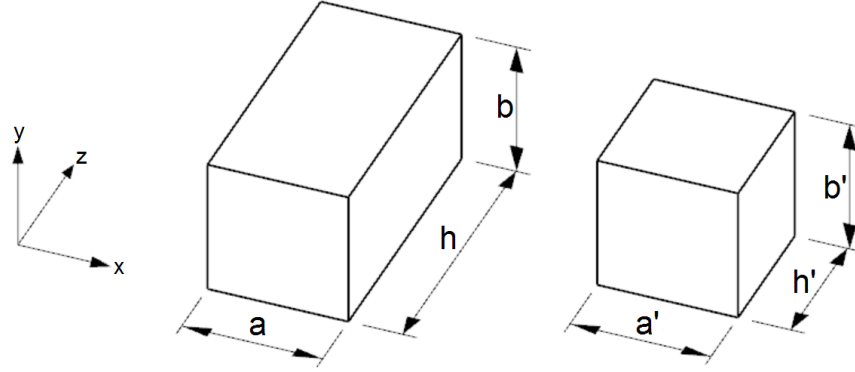


Figure J.1: Conversion from homogenized properties to the element properties in local coordinate system. Left: real size homogenized element. Right: mesh-size volumetric element.

Among the dimensions shown in Fig. J.1, $a = a'$ and $b = b'$, and h' is predefined, this leaves h the only variable. The conversion of the properties aims to retain the relationship between the external force and its response to the structure, i.e. for Young's modulus F/ε is same for both homogenized element and volumetric element. The force and strain has relation as in Eq. (J.1):

$$F = E\varepsilon A \quad (\text{J.1})$$

where:

F is external force.

E is Young's modulus.

ε is strain.

A is area.

Assuming the external forces and the strains for both homogenized element and volumetric element are identical, it yields:

$$E_{homo}A_{homo} = E_{mesh}A_{mesh} \Rightarrow E_{mesh} = E_{homo} \frac{A_{homo}}{A_{mesh}} \quad (\text{J.2})$$

Next, the Young's modulus for three directions can be derived:

$$\begin{cases} E_{x,mesh} &= E_{x,homo}\eta \\ E_{y,mesh} &= E_{y,homo}\eta \\ E_{z,mesh} &= E_{z,homo} \end{cases} \quad (\text{J.3})$$

where:

η is $\frac{h}{h'}$.

Likewise, the shear modulus also has relationship as follow:

$$G_{mesh} = G_{homo} \frac{A_{homo}}{A_{mesh}} \quad (J.4)$$

where:

G is shear modulus.

However, different from Young's modulus, shear modulus is related to two directions of the element which means the following equation needs to be fulfilled:

$$G_{ij,mesh} = G_{ji,mesh} \quad (J.5)$$

where:

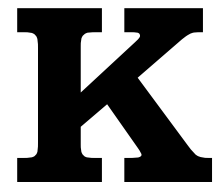
i, j are directions x, y, z in local coordinate system.

Because there is only one variable h' , which results in unequal $G_{ij,mesh}$ and $G_{ji,mesh}$ in some directions. Therefore, their values are averaged:

$$G'_{ij,mesh} = G'_{ji,mesh} = \frac{G_{ij,mesh} + G_{ji,mesh}}{2} \quad (J.6)$$

Finally, the shear modulus for the volumetric elements can be converted as follow:

$$\begin{cases} G_{xy,mesh} &= G_{xy,homo}\eta \\ G_{xz,mesh} &= 0.5 \times G_{xz,homo}(\eta + 1) \\ G_{yz,mesh} &= 0.5 \times G_{yz,homo}(\eta + 1) \end{cases} \quad (J.7)$$



Custom defined interpretation of the strain results

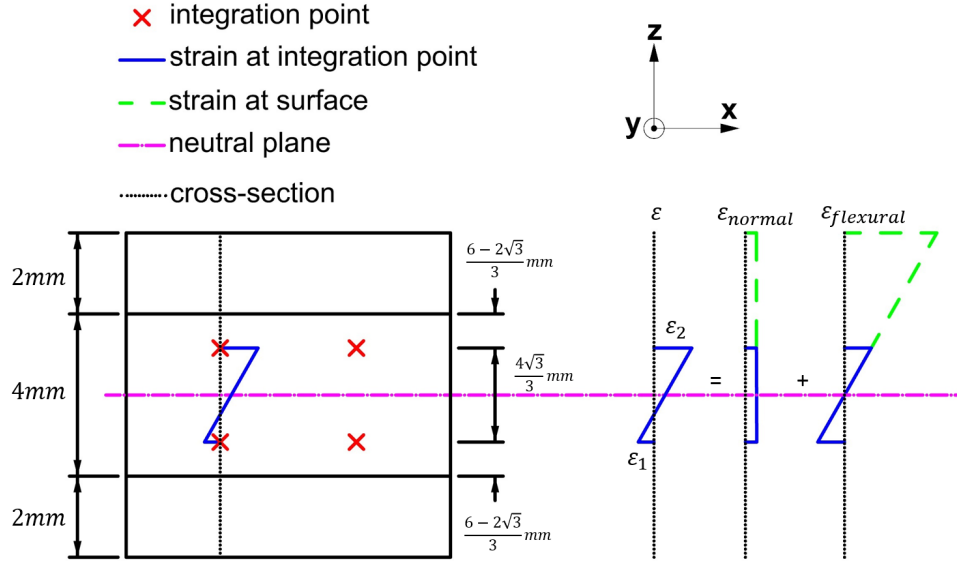


Figure K.1: Definition of the strain interpretation.

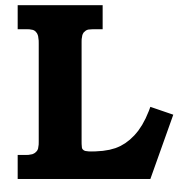
The custom interpretation of the strain results is based on the thin-shell theory, and the strain varies linearly along the cross-section of the shell element. It aims to generate strain results for comparison with the yielding criterion. As shown in Fig. K.1, the reference points for generating the strain are the integration points of the middle layer of the triple-layer shell element. Two integration points can determine one strain distribution, and it (ε) can be considered as consisting of normal strain and flexural strain. However, for the flexural strain, its yielding can be influenced by the normal strain. Therefore, the flexural strain is considered as the maximum value of ε_1 and ε_2 :

$$\begin{cases} \varepsilon'_{normal} &= |0.5(\varepsilon_1 + \varepsilon_2)| \\ \varepsilon'_{flexural} &= \max(|\varepsilon_1|, |\varepsilon_2|) \end{cases} \quad (\text{K.1})$$

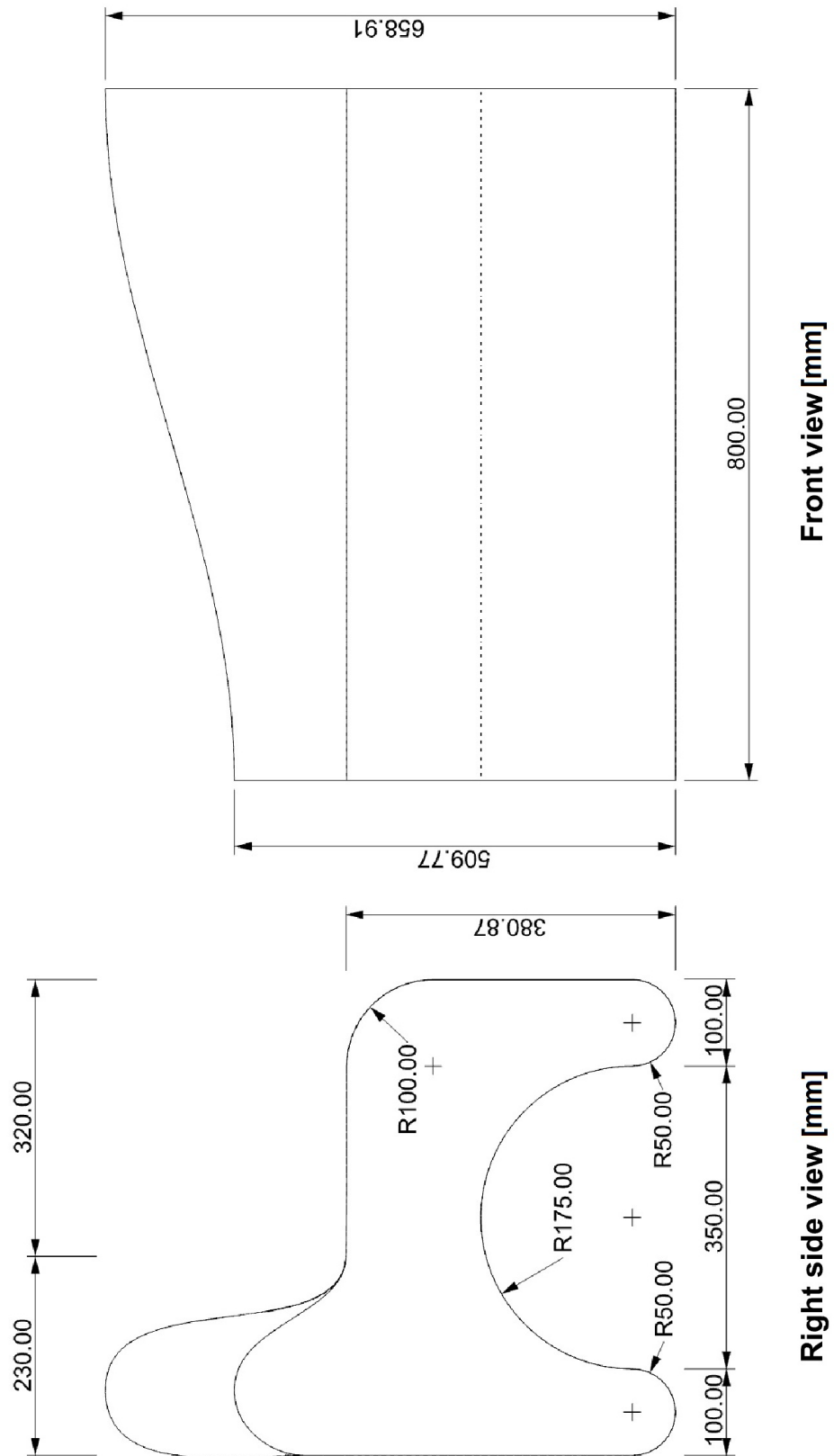
Next, the strains need to be linearly extrapolated to the surface. The total thickness of the shell element is 8mm as defined in Table 5.1, and the locations of the integration points are as shown in Fig. K.1, then the final strain can be derived:

$$\begin{cases} \varepsilon_{normal} &= \varepsilon'_{normal} \\ \varepsilon_{flexural} &= \varepsilon'_{flexural} \times 12/(9 + \sqrt{3}) \end{cases} \quad (\text{K.2})$$

There are 8 integration points in the middle-layer, considering two directions, it generate 8 flexural strains and 8 normal strains. They are compared with the strain criterion to check if the element is in the allowable strain state.



Details of the parametric bench for the case study



M

Details of the self-compact concrete
C65

Cement		Droge massa	Te doseren massa	Te doseren volume	Volume fijn			Totale fractieV/V
CEM III/B 42.5 N LH HS ENCI IJMUIDEN		260kg	260kg	88L	88,1L			8,81%
CEM I 52.5 R ENCI MAASTRICHT		220kg	220kg	70L	69,8L			6,98%
TotaalCement		480kg	480kg	158L	158,0L			15,80%
Zand		Droge massa	Te doseren massa	Te doseren volume	Volume fijn	Vocht	Absorptie	Totale fractieV/V
Rivierzand 0/4 mm		772kg	776kg	295L	15,5L	0,50% M/M	0,50% M/M	29,46%
TotaalZand		772kg	776kg	295L	15,5L			29,46%
Grind		Droge massa	Te doseren massa	Te doseren volume	Volume fijn	Vocht	Absorptie	Totale fractieV/V
Riviergrind 2/8 mm		882kg	882kg	346L	38,2L	0,00% M/M	0,00% M/M	34,58%
TotaalGrind		882kg	882kg	346L	38,2L			34,58%
Hulpstof		Droge massa	Te doseren massa	Te doseren volume	Volume fijn	T.o.v. bindmiddel	T.o.v. cement	Totale fractieV/V
Cugla-LR-7090 Superplastificeerder con. 20		1,680kg	1,680kg	1,600L	0,0L	0,35% M/M	0,35% M/M	0,16%
Cugla HR Superplastificeerder con. 20%		2,400kg	2,400kg	2,286L	0,0L	0,50% M/M	0,50% M/M	0,23%
TotaalHulpstof		4,080kg	4,080kg	3,886L	0,0L			0,39%
Water en slib		Massa bij droge materialen	Te doseren massa	Te doseren volume	Volume fijn			Totale fractieV/V
Leidingwater		183kg	183kg	183L	0,0L			18,28%
TotaalWater en slib		183kg	183kg	183L	0,0L			18,28%
Lucht				15L	0,0L			1,50%
Totaal (7 Grondstoffen):			2324kg	1000L	211,6L			100%

List of Figures

1.1	3D printed Urban Cabin by DUS architects [3] (photo by Ossip van Duivenbode). . . .	1
1.2	Application of 3D printing.	2
1.3	Stainless steel node made by additive manufacturing [9].	2
1.4	Application of concrete 3D printing in Phoenix International Media project [10].	3
1.5	Large-scale 3D printed products by Aectual [13]. Left: facade. Middle: floor. Right: mould for casting concrete staircase.	3
1.6	Beach cleanup activity conducted by Greenpeace on Freedom Island, Philippines [17]. .	4
1.7	Thermoplastics and thermosets [20].	4
1.8	Mechanical recycling steps of plastics [21, 22].	5
1.9	Several physical phenomenons occur with the increase of the recycling cycle [23]. . . .	5
1.10	Preparation of the material for recycling at Aectual. Left: small segments. Middle: shredded pellets for printing. Right: printing process(example) [28].	6
1.11	Form finding used by Antoni Gaudí during the design of Sagrada Família [29].	6
1.12	Tree structures [30].	7
1.13	Three categories of structural optimisation.(a)sizing optimisation (b)shape optimisation (c)topology optimisation [32].	7
1.14	Three types of application with the large scale 3D printing [13].	8
1.15	Previous projects. Left: printed beam for testing [33]. Middle: printed columns with steel core after test [34]. Right: parametric wall designed with utilization of pre-deformation method [35].	8
2.1	Environmental conditions for tests	10
2.2	Coordinate system utilized in the research. Left: global coordinate system. Right: local coordinate system	11
2.3	Preparation for the samples. Left: Printed geometry for preliminary test. Right: Water cutting machine at Schrijfver B.V.	12
2.4	Toe effect in stress-strain curve. [40]	12
2.5	Integration of software products utilized in the research	13
3.1	Application of the preliminary test	16
3.2	Force-displacement curve of Scolefin 53-G-10 natural. Green: linear parts. Blue: non-linear transition.	16
3.3	Maximum force and corresponding displacement regarding different composition of Scolefin 53-G-10 natural. Left: speed 0.5 mm/min. Right: speed 10 mm/min (Percentage is the content of virgin material)	17
3.4	Delamination with virgin/recycled ratio of 75%/25%. Left: delamination of the sample. Right: delamination of the printed sheet	17
3.5	Force-displacement curve of Technomelt 3D 6910.	18
3.6	Plastic deformation with narrowing while testing Technomelt 3D 6910.	19
3.7	Maximum force and corresponding displacement for different compositions of Technomelt 3D 6910. Left: speed 0.5 mm/min. Right: speed 10 mm/min (Percentage is the content of virgin material)	19
3.8	Force-displacement curve of 60%LDPE+40%PPgf recycled.	20
3.9	Maximum force and corresponding displacement regarding different composition of 60%LDPE 3+40%PPgf recycled. Left: speed 0.5 mm/min. Right: speed 10 mm/min (Percentage is the content of virgin material)	20

3.10	Maximum force and corresponding displacement with respect to recycling rounds of Technomelt 3D 6910. Left: speed 0.5 mm/min. Right: speed 10 mm/min	21
3.11	Bad quality of sheet of Technomelt 3D 6910 with multi-round printing	21
3.12	Elongation of different basic material with respect to recycled material content.	22
3.13	Elongation of Technomelt 3D 6910 with respect to recycling rounds.	23
3.14	Failure in 45 degree during the tensile test of 60%LDPE 3+40%PPgf recycled.	24
3.15	Decent printing quality with Technomelt 3D 6910.	24
4.1	Application of the property tests. (a)Standard tensile test. (b)Three points bending test. (c)Modified shear test.	25
4.2	Geometry for producing double-layer samples.	26
4.3	The influence of first printed layers. Up: the first printed layers in the printed product. Down: the failure at clamps.	26
4.4	Tensile test results of single-layer samples	29
4.5	Tensile test results of double-layer samples	29
4.6	Bending test results of single-layer samples	30
4.7	Bending test results of double-layer samples	30
4.8	Failure in shear tests.	31
4.9	Determination of the design value for the tensile property in the longitudinal direction of a single-layer wall.	32
4.10	Nonuniform curing throughout the cross section [35].	33
4.11	Voids caused by shrinkage in a segment of printed line, with local coordinate system. Up: Undeformed state. Down: After bent.	34
4.12	Nonuniform density caused by shrinkage, with local coordinate system. Solid line: profile after shrinkage. Dash line: profile before shrinkage. Circle: glass-fibre.	34
4.13	Stiffness reduction with multi-layer printing. Left: two adjacent layers with overlap (dash line: E distribution of single layer. solid line: E distribution after second layer printed). Right: three adjacent layers with overlap (blue line: asymmetric E distribution along the cross-section).	35
5.1	Side view of structured mould.	37
5.2	Side view of optimised mould.	38
5.3	Process of envelope generation with shell element (presented with symmetry).	39
5.4	Overlapping shell elements at a knot [41].	39
5.5	Process of envelope generation with volumetric element (presented with symmetry).	40
5.6	Element at corner (Planar view).	40
5.7	Sandwich elements represent a section of formwork for a rectangular column. Blue: shell elements for the inner and outer layer. Red: volumetric element for rib layer.	41
5.8	Distribution of the Young's modulus across the cross-section of printed wall. Solid: Young's modulus distribution. Dash: profile of cross-section.	41
5.9	Second order quadratic shell element(S8R) utilized in CalculiX [41].	42
5.10	Expansion of the S8R shell element. [41]	42
5.11	Integration points distribution of C3D20R brick element [35].	42
5.12	Inverse stiffness matrix of transverse isotropic material	43
5.13	Multilayer shell for modelling Young's modulus distribution across the cross-section. Blue: distribution curve of Young's modulus.	44
5.14	Triple-layer shell element[35].	45
5.15	Adjustment of Young's modulus distribution by modification of the thickness. Blue: origi- nal Young's modulus distribution along the thickness. Green: modified Young's modulus distribution along the thickness.	46
5.16	Planar geometry of rib layer with regular hexagon	47
5.17	Area coverage of regular triangle and regular hexagon with the same perimeter. If the regular triangle covers an area of A , then the regular hexagon can cover $1.52A$	47
5.18	Printing angle and bonding length of triangle and hexagon.	47
5.19	Unit cell used for homogenization of honeycomb [59, 60].	48

5.20	Conversion from homogenized properties to the element properties in local coordinate system. Left: real size homogenized element. Right: mesh-size volumetric element. . .	49
5.21	Numerical model for tensile test [mm]. Blue: clamped. Red: displacement in positive x direction.	50
5.22	Numerical model for tensile test [mm]. Blue: steel head, displacement in negative z direction. Red: steel support, fixed.	50
5.23	Side view of the single-layer mould for casting rectangular column.	52
5.24	Displacement pattern. Left: ANSYS. Right: CaluliX.	52
5.25	Dimensions [mm] and boundary conditions for composite element represented model.	53
5.26	Numerical models for structured mould. Left: real structured model in ANSYS. Right: composite element represented model in CaluliX.	54
6.1	One composite element in the local coordinate system. Blue: one shell element as outer layer. Orange: one volumetric element as rib layer. Green: one shell element as inner layer.	57
6.2	Sensitivity analysis for selecting elements to increase property.	59
6.3	Example mould. Left: boundary conditions of one quarter of the mould. Right: hydrostatic pressure.	60
6.4	Composite element represented mould. Left: meshed mould. Right: planar view shows the composition.	60
6.5	Thickness distribution with the iteration.	61
6.6	Internal energy changes with the iteration.	62
6.7	Constructed mould for checking. Left: technical planar view. Middle: constructed model in Rhino. Right: displacement distribution pattern of the mould from ANSYS.	62
6.8	Multilayer printing influence on the optimised mould (side view). Blue: cross-section of outer layer printing line. Orange: cross-section of rib layer printing line. Green: cross-section of inner layer printing line.	63
6.9	Length of double-layer printed part increases with the selected shape in case of smaller thickness of the rib layer (planar view). Blue: regular hexagon pattern. Yellow: longer double-layer printed part.	63
6.10	Integrated process of the thickness distribution.	64
7.1	Designed bench with seating area and parametric back.	65
7.2	Separated two parts of the bench.	66
7.3	Thickness distribution of <i>Part A</i> with iteration.	67
7.4	Internal energy distribution of <i>Part A</i> with iteration.	67
7.5	Thickness distribution of <i>Part B</i> with iteration.	67
7.6	Internal energy distribution of <i>Part B</i> with iteration.	68
7.7	Example of contour generation of <i>Part A</i>	68
7.8	Example of printing path at each level. Left: staggered. Right: aligned.	69
7.9	Example of shifting to the next layer.	69
7.10	Final shape as input for the 3D printer. Red circle: location of the seam.	69
7.11	Printed moulds for concrete casting. Left: Part A. Mid: Part B. Right: Three standard size cubes.	70
7.12	Staples at the bottom of the moulds.	70
7.13	Bottom sealing. Left: clay at outside. Right: Silicon at inside.	70
7.14	Filling the cracks. Left: surface of the mould after fixing the cracks. Right: the filler. . .	71
7.15	Two moulds ready for the casting.	71
7.16	Preparation for the casting. Left: ingredients for the concrete mixture. Right: blender which has a maximum volume of 200 litres.	72
7.17	Casting process. Left: cast three cubes. Right: cast the mould.	72
7.18	Final concrete product cast by the mould <i>Part A</i>	72
7.19	Double-curved part on the moulds where has cracks.	73
7.20	Bending moment caused by the uneven shrinkage.	73
7.21	Cracks caused by shrinkage. Left: large crack at outer surface. Right: Warping of the bottom of the mould.	74

C.1	Force-displacement curve for virgin/recycled material composition 100%/0%.	88
C.2	Force-displacement curve for virgin/recycled material composition 75%/25%.	89
C.3	Force-displacement curve for virgin/recycled material composition 50%/50%.	90
C.4	Force-displacement curve for virgin/recycled material composition 25%/75%.	91
C.5	Force-displacement curve for virgin/recycled material composition 100%/0%.	92
C.6	Force-displacement curve for virgin/recycled material composition 75%/25%.	93
C.7	Force-displacement curve for virgin/recycled material composition 50%/50%.	94
C.8	Force-displacement curve for virgin/recycled material composition 25%/75%.	95
C.9	Force-displacement curve for virgin/recycled material composition 100%/0%.	96
C.10	Force-displacement curve for virgin/recycled material composition 75%/25%.	97
C.11	Force-displacement curve for virgin/recycled material composition 50%/50%.	98
C.12	Force-displacement curve for virgin/recycled material composition 25%/75%.	99
C.13	Force-displacement curve for 1 st round recycle material.	100
C.14	Force-displacement curve for 2 nd round recycle material.	101
C.15	Force-displacement curve for 3 rd round recycle material.	102
D.1	Single layer transverse tensile test results.	104
D.2	Double layer longitudinal tensile test results.	105
D.3	Single layer longitudinal bending test results.	106
D.4	Single layer transverse bending test results.	107
D.5	Double layer longitudinal bending test results.	108
D.6	Single layer longitudinal shear test results.	109
D.7	Single layer transverse shear test results.	110
D.8	Double layer longitudinal shear test results.	111
E.1	Specimen for tensile test.	114
F.1	Experimental diagrams of pressure envelope [72].	116
G.1	Experimental diagrams of pressure envelope [72].	118
I.1	The mechanical model for calculating the maximum side length l of the regular hexagon.	122
J.1	Conversion from homogenized properties to the element properties in local coordinate system. Left: real size homogenized element. Right: mesh-size volumetric element.	126
K.1	Definition of the strain interpretation.	130

List of Tables

2.1	Materials for testing with different compositions and recycling rounds	11
3.1	Settings for preliminary tensile test	15
3.2	Unit of properties for comparison	16
3.3	Stiffness comparison with respect to different composition of Scolefin 53-G-10 natural.	18
3.4	Stiffness comparison with respect to different composition of Technomelt 3D 6910.	18
3.5	Stiffness comparison with respect to different composition of 60%LDPE+40%PPgf.	21
3.6	Stiffness comparison with respect to recycling round of Technomelt 3D 6910.	22
4.1	Settings for tensile test.	27
4.2	Settings for bending test.	27
4.3	Settings for shear test.	28
4.4	Cross-sectional properties per running millimetre	28
4.5	Shear strength.	31
4.6	Summery of the design values.	32
5.1	Numerical inputs for shell element.	46
5.2	Homogenized properties for regular hexagonal shape with side length of 100 mm.	49
5.3	Converted element properties for regular hexagonal shape with side length of 100 mm.	49
5.4	Comparison between experimental and model results with respect to tensile property.	51
5.5	Comparison between experimental and model results with respect to flexural property.	51
5.6	Result comparison between ANSYS and CalculiX.	53
5.7	Comparison between real structured model and composite element represented model.	54
5.8	Displacement comparison between real structured model built in ANSYS and composite element represented model in CalculiX.	54
7.1	Inputs for the thickness distribution methodology for the case study.	66
B.1	Value of k_n based on the different sample size.	86

Bibliography

- [1] BMBF-Internetredaktion, *Zukunftsprojekt Industrie 4.0 - BMBF*, (2016).
- [2] Xinhua, *'Made in China 2025' plan unveiled*, (2015).
- [3] DUS Architects, *URBAN CABIN*, (2015).
- [4] J. Excell and S. Nathan, *The rise of additive manufacturing*, *The engineer* **24** (2010).
- [5] J. Bird, *Exploring the 3d printing opportunity*, *The Financial Times*. Retrieved , 08 (2012).
- [6] 3D HUBS, *Transparent Plastic: See-through parts and prototypes*, (2012).
- [7] ULtimate 3D, *Reaching New Heights: 3D Printing In Aerospace and Why It's Catching On*, (2015).
- [8] P. Wu, J. Wang, and X. Wang, *A critical review of the use of 3-D printing in the construction industry*, *Autom. Constr.* **68**, 21 (2016).
- [9] S. Galjaard, S. Hofman, N. Perry, and S. Ren, *Optimizing Structural Building Elements in Metal by using Additive Manufacturing*, *Int. Assoc. Shell Spat. Struct.* (2015).
- [10] WIN SUN, *3D PRINTING ARCHITECTURE'S FUTURE*, (2012).
- [11] Heather Head, *A History of 3D Printing in Construction & What You Need to Know*, (2017).
- [12] H. Kodama, *Automatic method for fabricating a three-dimensional plastic model with photo-hardening polymer*, *Review of scientific instruments* **52**, 1770 (1981).
- [13] Aectual, *Aectual – Sustainable · Innovative · Yours*, (2017).
- [14] R. C. Thompson, S. H. Swan, C. J. Moore, and F. S. Vom Saal, *Our plastic age*, (2009).
- [15] J. R. Jambeck, R. Geyer, C. Wilcox, T. R. Siegler, M. Perryman, A. Andrady, R. Narayan, and K. L. Law, *Plastic waste inputs from land into the ocean*, *Science* **347**, 768 (2015).
- [16] J. Hopewell, R. Dvorak, and E. Kosior, *Plastics recycling: challenges and opportunities*, *Philos. Trans. R. Soc. B Biol. Sci.* **364**, 2115 (2009), [arXiv:rstb.2008.0311](https://arxiv.org/abs/rstb.2008.0311) [: 10.1098] .
- [17] Tisha Brown, *Welcome to Ground Zero of the Ocean Plastic Pollution Crisis*, (2017).
- [18] J. Snudden, C. Ward, and K. Potter, *Reusing automotive composites production waste*, *Reinforced Plastics* **58**, 20 (2014).
- [19] A. Merrington, *Appl. Plast. Eng. Handb.*, second edi ed. (Elsevier Inc., 2017) pp. 167–189.
- [20] Akshay Chavan, *The Plastic Wars: Difference Between Thermoplastics and Thermosets*, (2016).
- [21] S. Al-Salem, P. Lettieri, and J. Baeyens, *Recycling and recovery routes of plastic solid waste (psw): A review*, *Waste management* **29**, 2625 (2009).
- [22] M. P. Aznar, M. A. Caballero, J. A. Sancho, and E. Francés, *Plastic waste elimination by co-gasification with coal and biomass in fluidized bed with air in pilot plant*, *Fuel Processing Technology* **87**, 409 (2006).
- [23] S. Yin, R. Tuladhar, F. Shi, R. A. Shanks, M. Combe, and T. Collister, *Mechanical reprocessing of polyolefin waste: A review*, *Polym. Eng. Sci.* **55**, 2899 (2015), [arXiv:0406218](https://arxiv.org/abs/0406218) [cond-mat] .
- [24] K. Giannadakis, M. Szpieg, and J. Varna, *Mechanical Performance of a Recycled Carbon Fibre/PP Composite*, *Exp. Mech.* **51**, 767 (2011).

- [25] R. Strapasson, S. C. Amico, M. F. Pereira, and T. H. Sydenstricker, *Tensile and impact behavior of polypropylene/low density polyethylene blends*, *Polym. Test.* **24**, 468 (2005).
- [26] I. Anderson, *Mechanical properties of specimens 3d printed with virgin and recycled polylactic acid*, *3D Printing and Additive Manufacturing* **4**, 110 (2017).
- [27] F. Veer, F. Setaki, A. Riemslog, and P. Sakkas, *The strength and ductility of glass fibre reinforced 3d-printed polypropylene*, (2016).
- [28] DUS Architects, *3DPRINTCANALHOUSE by DUS Architects*, <http://3dprintcanalhouse.com/> (2014).
- [29] IAAC, *MAA SEMINAR: FORM FINDING WITH CHRISTINE OTTO KANSTINGER*, (2012).
- [30] F. Otto, B. Rasch, D. W. Bayern, K. V. Stuck, and A. anlässlich der Preisverleihung des Deutschen Werkbundes Bayern an Frei Otto und Bodo Rasch, *Frei Otto, Bodo Rasch: Finding form: towards on architecture of the minimal; the Werkbund shows Frei Otto, Frei Otto shows Bodo Rasch; exhibition in the Villa Stuck, Munich, on the occasion of the award of the 1992 Deutscher Werkbund Bayern Prize to Frei Otto und Bodo Rasch* (Ed. Menges, 2006).
- [31] K. M. MacBain and W. Spillers, *Structural Optimization* (2009).
- [32] M. P. Bendsøe and O. Sigmund, *Engineering*, Vol. 2nd Editio (2003) p. 370.
- [33] A. van der Veen, *The Structural Feasibility of 3D-printing houses using printable polymers*, Master's thesis, Delft University of Technology, Delft (2014).
- [34] S. Peulen, *Vergroten knik gedrag van een stalen staaf door inzet van 3d geprint materiaal*, (2015).
- [35] P. K. Baran, *Methodology and Tools for Test- ing, Numerical Analysis and De- sign of the 3D Printed Moulds*, (2016).
- [36] A. V. D. Veen, *The Structural Feasibility of 3D-printing houses using printable polymers*, (2014).
- [37] R. Francis, *Recycling of polymers : methods, characterization and applications* (2016).
- [38] P. F. Infante, L. D. Schuman, and J. Huff, *Fibrous glass insulation and cancer: response and rebuttal*, *American journal of industrial medicine* **30**, 113 (1996).
- [39] NEN-EN 1990 + a1 + a1 / C2 + NB, *Eurocode: Basis of structural design*, Standard (Nederlands Normalisatie-instituut, Delft, 2008).
- [40] G. Swallowe, *Tensile and compressive testing*, in *Mechanical Properties and Testing of Polymers* (Springer, 1999) pp. 242–247.
- [41] G. Dhondt, *CalculiX CrunchiX USER ' S MANUAL version 2.13*, (2017).
- [42] TIOBE, *TIOBE Index for January 2018*, (2017).
- [43] NEN-EN-ISO 527-4, *Plastics - Determination of tensile properties - Part 4: Test conditions for isotropic and orthotropic fibre-reinforced plastic composites*, Standard (International Organization for Standardization, Geneva, CH, 1997).
- [44] G. Thomas, *Recycling of Polypropylene (PP)*, (2012).
- [45] NEN-EN-ISO 527-1, *Plastics - Determination of tensile properties - Part 1: General principles*, Standard (International Organization for Standardization, Geneva, CH, 2012).
- [46] NEN-EN-ISO 178, *Plastics - Determination of flexural properties*, Standard (International Organization for Standardization, Geneva, CH, 2010).
- [47] Y. Bao and T. Wierzbicki, *On fracture locus in the equivalent strain and stress triaxiality space*, *International Journal of Mechanical Sciences* **46**, 81 (2004).

- [48] V. Shah, *Handbook of Plastics Testing and Failure Analysis*, 3rd ed. (John Wiley & Sons, Hoboken, 2007).
- [49] D. G. Ullman, *The mechanical design process* (McGraw-Hill Science/Engineering/Math, 2015).
- [50] ANSYS, *Engineering Simulation and Design Software | ANSYS*, Website (2017).
- [51] M. G. Larson and F. Bengzon, *The finite element method: Theory, implementation, and applications*, Vol. 10 (Springer Science & Business Media, 2013).
- [52] Aremu A, Ashcroft I, Hague R, Wildman R, and Tuck C, *Suitability of SIMP and BESO Topology Optimization Algorithms for Additive Manufacture*, Solid Free. Fabr. Proc. , 679 (2010).
- [53] Dassault Systèmes, *Abaqus 6.10. Benchmarks Manual* (2010).
- [54] Dassault Systèmes, *Abaqus 6.11. Theory Manual* (2011).
- [55] S. P. Timoshenko and S. Woinowsky-Krieger, *Theory of plates and shells* (McGraw-hill, 1959).
- [56] J. S. Bergstrom, *Mechanics of Solid Polymers*, 1st ed. (William Andrew, San Diego-London-Waltham, 2015).
- [57] A. F. Bower, *Applied Mechanics of Solids*, 1st ed. (CRC Press, Boca Raton, 2010).
- [58] H. P. Gavin, *Mathematical properties of stiffness matrices*, Duke University **9** (2013).
- [59] H. E. Soliman, *Mechanical Properties of Cellular Core Structures*, (2016).
- [60] G. Shi and P. Tong, *The derivation of equivalent constitutive equations of honeycomb structures by a two scale method*, *Comput. Mech.* **15**, 395 (1995).
- [61] Ineos Olefins & Polymers USA, *Typical Engineering Properties of Polypropylene*, Tech. Rep. (2010).
- [62] E. Reissner, *The effect of transverse shear deformation on the bending of elastic plates*, *J. appl. Mech.* , A69 (1945).
- [63] A. A. Novotny, R. A. Feijóo, E. Taroco, and C. Padra, *Topological sensitivity analysis*, *Comput. Methods Appl. Mech. Eng.* **192**, 803 (2003).
- [64] A. A. Novotny and R. A. Feij, *Topological Sensitivity Analysis for Three-dimensional Linear Elasticity Problem $x \in n (W) (W e)$* , **1** (2005).
- [65] Z. H. Zuo and Y. M. Xie, *A simple and compact Python code for complex 3D topology optimization*, *Adv. Eng. Softw.* **85**, 1 (2015).
- [66] O. Sigmund, *A 99 line topology optimization code written in matlab*, *Struct. Multidiscip. Optim.* **21**, 120 (2001).
- [67] A. T. Gaynor and J. K. Guest, *Topology optimization considering overhang constraints: Eliminating sacrificial support material in additive manufacturing through design*, *Struct. Multidiscip. Optim.* **54**, 1157 (2016).
- [68] I. Masters and K. Evans, *Models for the elastic deformation of honeycombs*, *Composite structures* **35**, 403 (1996).
- [69] G. Shi and P. Tong, *Equivalent transverse shear stiffness of honeycomb cores*, *International Journal of Solids and Structures* **32**, 1383 (1995).
- [70] K. Svanberg, *MMA and GCMMA – two methods for nonlinear optimization*, **1**, 1 (2007).
- [71] L. L. Beghini, J. Carrion, A. Beghini, A. Mazurek, and W. F. Baker, *Structural optimization using graphic statics*, *Struct. Multidiscip. Optim.* **49**, 351 (2014).
- [72] I. Puente, A. Santilli, and A. Lopez, *Lateral pressure over formwork on large dimension concrete blocks*, *Eng. Struct.* **32**, 195 (2010).

-
- [73] E. DIN, 18218, Frishbetondruck auf lotrechte Schalungen. Deutsches institut für normung (2008).
- [74] S.-Y. Fu, B. Lauke, and Y.-W. Mai, *Science and Engineering of Short Fibre Reinforced Polymer Composites* (Woodhead Publishing, [s.l.], 2009).